LAWRENCE
LIVERMORE
NATIONAL
LABORATORY

UCRL-TR-217303

Deep Borehole Instrumentation Along San Francisco Bay Bridges: 1996 - 2003 and Strong Ground Motion Systhesis Along the San Francisco/Oakland Bay Bridge

L. Hutchings, W. Foxall, P. Kasameyer, S. Larsen, C. Hayek, C. Tyler-Turpin, J. Aquilino, L. Long

November 23, 2005

Disclaimer

This document was prepared as an account of work sponsored by an agency of the United States Government. Neither the United States Government nor the University of California nor any of their employees, makes any warranty, express or implied, or assumes any legal liability or responsibility for the accuracy, completeness, or usefulness of any information, apparatus, product, or process disclosed, or represents that its use would not infringe privately owned rights. Reference herein to any specific commercial product, process, or service by trade name, trademark, manufacturer, or otherwise, does not necessarily constitute or imply its endorsement, recommendation, or favoring by the United States Government or the University of California. The views and opinions of authors expressed herein do not necessarily state or reflect those of the United States Government or the University of California, and shall not be used for advertising or product endorsement purposes.

This work was performed under the auspices of the U.S. Department of Energy by University of California, Lawrence Livermore National Laboratory under Contract W-7405-Eng-48.

Deep Borehole Instrumentation along San Francisco Bay Bridges: 1996 - 2003
and
Strong Ground Motion Synthesis along the San Francisco/Oakland Bay Bridge

Final Report

July 15, 2005

Caltrans contract no. 59A0238

Lawrence Hutchings, Bill Foxall, Paul Kasameyer, Shawn Larsen,
Cindy Hayek, Christy Tyler-Turpin, Jennifer Aquilino, and Laura Long

Lawrence Livermore National Laboratory
Energy and Environmental Sciences
Hazards Mitigation Center
P.O. Box 808, Livermore, CA 94551

DISCLAIMER

This document was prepared as an account of work sponsored by an agency of the United States Government. Neither the United States Government nor the University of California nor any of their employees makes any warranty, express or implied, or assumes any legal liability or responsibility for the accuracy, completeness, or usefulness of any information, apparatus, product, or process disclosed, or represents that its use would not infringe privately owned rights. Reference herein to any specific commercial product, process, or service by trade name, trademark, manufacturer, or otherwise, does not necessarily constitute or imply its endorsement, recommendation, or favoring by the United States Government or the University of California. The views and opinions of authors expressed herein do not_ necessa4l$_y$ state or reflect those of the United States Government or the University of California, and shall not be used for advertising or product endorsement purposes.

Work performed under the auspices of the U. S. Department of Energy by the University of California Lawrence Livermore National Laboratory under Contract W-7405-Eng-48.

This report has been reproduced
directly from the best available copy.

Available to DOE and DOE contractors from the
Office of Scientific and Technical Information
P.O Box 62, Oak Ridge, TN 37831
Prices available from (423) 576-8401
http://apollo.osti.gov/bridge/

Available to the public from the
National Technical Information Service
U.S. Department of Commerce
5285 Port Royal Rd.,
Springfield, VA 22161
http://www.ntis gov/

OR

Lawrence Livermore National Laboratory
Technical Information Department's Digital Library
http://www.llnl.gov/tid/Library.html

Abstract

As a result of collaboration between the Berkeley Seismographic Station, Lawrence Livermore National Laboratory, and Caltrans, instrument packages have been placed in bedrock in six boreholes and two surface sites along the San Francisco/Oakland Bay Bridge. Since 1996 over 200 local earthquakes have been recorded. Prior to this study few seismic recording instruments existed in bed-rock in San Francisco Bay. We utilized the data to perform analysis of ground motion variability, wave passage, site response, and up-and down-hole wave propagation along the Bay Bridge. We also synthesized strong ground motion at nine locations along the Bay Bridge. Key to these studies is LLNL's effort to exploit the information available in weak ground motions (generally from earthquakes < M=4.0) to enhance predictions of seismic hazards.

We found that Yerba Island has no apparent site response at the surface relative to a borehole site. The horizontal to vertical spectral ratio method best revealed no site response, while the complex signal spectral ratio method had the lowest variance for spectral ratios and best predicted surface recordings when the borehole recording was used as input. Both methods identified resonances at about the same frequencies. Regional attenuation results in a significant loss of high frequencies in both surface and borehole recordings. Records are band limited at near 3 Hz. Therefore a traditional rock outcrop site response, flat to high frequency in displacement, is not available.

We applied a methodology to predict and synthesize strong ground motion along the San Francisco/Oakland Bay Bridge from a M=7.25 earthquake along the Hayward fault, about12 km distant. We synthesized for three-components and broad-band (0.0-25.0 Hz) ground motion accelerations, velocities, and displacements. We examined two different possible rupture scenarios, a “mean” and “one standard deviation” model. We combined the high frequency calculations (Hz > 0.7) based on empirical Green’s functions with finite difference calculations for frequencies less than 0.7 Hz. We found that in the near-source region, far-field shear-wave generation and near-field tectonic ground displacements can result in very large long period ground displacements and velocity pulses. Far-field arrivals have the strongest energy in periods of about 2 to 5 s, and near-field arrivals have the strongest energy in periods of about 5 to 10 s. Much of these near-source ground motions would not be observed by conventional strong motion recording systems, which typically are high-pass band limited at 2-5 s periods, and therefore have not been included as standard practice structural input ground motions. For some fault rupture scenarios, the large tectonic displacement pulse would initially drive the bridge with motions parallel to tectonic fault displacement, and before the bridge would start to rebound, the far-field S-wave would arrive and drive the bridge in the opposite direction. This type of multiple long-period modal response can occur in other long period structures such as base-isolated systems and tall buildings.

Acknowledgments

We would like to thank Pat Hipley for his continued support and encouragement. This work was performed under Caltrans contract no. 59A0238. It was also performed under the auspices of the U.S. Department of Energy by University of California, Lawrence Livermore National Laboratory under Contract W-7405-Eng-48. This work was partially funded by the Campus/Laboratory Collaboration Project. We benefited from cooperation from Lawrence Berkeley National Laboratory and the Berkeley Seismological Laboratory; especially Tom McEvilly and Rich Clymer.

We would also like to acknowledge the inspiration, enthusiasm and vision of the late Dr. Tom McEvilly in helping to bring about the instrumentation in S.F. Bay.

Related Publications

Several students and research collaborators participated in studies as part of this project that resulted in the following publications:

Baise, Laurie, Lawrence Hutchings, and Steven Glaser (2001) Analysis of Site Response at Yerba Buena Island, San Francisco Bay, California from Weak Motion Recordings. Special Issue on Site Response, *Bollettino di Geofisica, V* 42 219-243. Trieste, Italy.

Hutchings, L., P. Kasameyer, W. Foxall, T. McEvilly, R. Clymer, and R. Uhrhammer (2002) Deep Borehole Instrumentation Along San Francisco Bay Bridges - 2001-2002. Lawrence Livermore National Laboratory, UCRL 132137-03.

Hutchings, L., P. Kasameyer, C. Turpin, L. Long, W. Foxall, J. Hollfelder, T. McEvilly, R. Clymer, and R. Uhrhammer (2001) Deep Borehole Instrumentation Along San Francisco Bay Bridges - 2000. Lawrence Livermore National Laboratory, UCRL 132137-02.

Hutchings, L., P. Kasameyer, C. Turpin, W. Foxall, J. Hollfelder, T. McEvilly, R. Clymer, and R. Uhrhammer (2000) Deep Borehole Instrumentation Along San Francisco Bay Bridges - 1999. Lawrence Livermore National Laboratory, UCRL 132137-01.

Mualchin, Lalliana, Pat Hipley, Lawrence Hutchings, Jennifer Hollfelder, Steve Jarpe, and Kazuoh Seo (1998) Wave Propagation along the San Francisco, California Bay Bridge. proceedings, Second International Symposium on the Effects of Surface Geology on Seismic Motion, Yokohama, Japan, December 1-3, pp 22-31.

Hutchings, Lawrence, Paul Kasameyer, William Foxall, Jennifer Hollfelder, Christine Turpin and Steven Jarpe (1999) Deep Bore Hole Instrumentation along the San Francisco Bay Bridges 1996- 1998. Lawrence Livermore National Laboratory UCRL-ID-132137, pp 28.

Hayek, Cynthia, Lawrence Hutchings, Steven Jarpe, Charles Hoelzer, Patricia Jovane, and Jennifer Hollfelder (1997) A Bedrock Borehole Study of the Site Response in the Eastern San Francisco Bay Area, Ca. *Seis Res Let,* **68** (1).

Hutchings, L., T. McEvilly, J. Cullen, W. Foxall, R. Clymer, W. Bakun, J. Bowman, and M. Palmer (1995) Deep Bore Hole Instrumentation along San Francisco Bay Bridges. Assoc Eng

Geol and Groundwater Res Assoc of Calif, 38th Annual meeting, Sacramento, Ca.

Turpin (Tyler), Christy. *(2000) Seismic Profile of the Franciscan Formation Beneath the San Francisco-Oakland Bay Bridge, San Francisco Bay, California,* senior thesis, California State University, Sacramento, California.

Table of Content

Abstract …….. *i*

Related Publications ……..……..……... i*i*

Introduction …….……... 1

Instrumentation ……..…… 2

Sensor Description …… 11

Sensor Orientation ……...……. 12

Signal to Noise ……...……...……. 14

Geology of San Francisco Bay ….……..…… 16

Bay Bridge Microearthquake Analysis ...…… 19

Corner Frequency ……...…….…. 19

December 04, 1998, M=4.1 Event …….…….…….…. 22

Site Response Transfer Function at Yerba Buena Island ...…. 22

Coherency ..……...…….…. 28

Dumbarton Bridge Microearthquake Analysis ...…… 29

Site to Site Variability ……...…. 29

Site Response Functions at Dumbarton Bridge ……...…. 29

Strong Ground Motion Synthesis for the Bay Bridge …..…… 36

Modeling Approach ……...…. 37

EMPSYN ……..……...…. 38

Green's Functions……...…...…. 38

Empirical Green's Functions ……...…… 39

Synthetic Green's Functions ……...…… 39

Near-Source Ground Motion …..……...…...…. 40

Hayward Fault Rupture ……..……...…...…. 42

Strong Ground Motion Prediction …….……...…...…. 44

Ground Motions along the Bay Bridge …….…...… 52

Summary and Conclusions …..…….…….…...… 89

Bibliography ……...…..…….…….…...… 90

.

Introduction

This report provides documentation and analysis of microearthquake recordings of the Bay Bridges downhole network. Prior to this study few seismic recording instruments existed in bedrock in San Francisco Bay. This left a recording gap for engineering studies of the Bay bridges and in seismicity studies of the Bay Area. Analysis of wave propagation, coherency, ground motion variability, strong ground motion synthesis along the bridges, site response and, and up-an down-hole wave propagating is presented. Key to these studies is LLNL's effort to exploit the information available in weak ground motions (generally from earthquakes < M=3.0) to enhance predictions of seismic hazards. Although strong ground motion recordings are essential to calibrate models and understand the hazard of future earthquakes, we can obtain weak ground motion data immediately, whereas it may be years before strong motion data is recorded. Following is an expansion of research goals utilizing recordings from the Bridges Network.

1) prediction of strong ground motion: LLNL is developing a methodology of using weak ground motion to synthesize linear response strong ground motion and incorporating this with constraints on fault rupture scenarios to predict strong ground motion. These computations provide estimates of the full wavetrain ground motion at multiple points along long span structures.

2) ground motion variability: Recent studies have demonstrated the high variability of strong ground motion with site conditions. Recordings along Bay bridges are used both to improve calculations of ground motions for bridges, and to research the spatial sensitivity and significance of site variability to structures.

3) soils response: LLNL is researching means of using weak ground motion to constrain soils models for non-linear computations. Current research has shown that low strain constitutive properties are significant to non-linear ground motion computations, and that these values can be significantly improved by an iterative process of matching weak motion solutions.

4)bridge response calculations: Current developments in structural dynamics allow non-linear, three-dimensional calculation of bridge response. This requires realistic full wavetrain input ground motions. LLNL is conducting research on the sensitivity of synthetic ground motions to accurate non-linear computations, and the significance of utilizing multiple support input calculations.

5) seismicity: Location of small earthquakes within the Bay that may indicate the existence of active faults is possible with the instrumentation. Very small earthquakes (M<2) beneath the Bay cannot be recorded adequately to determine locations by regional networks.

6) strong ground motion: The network is capable of recording up to 0.5 g acceleration from local strong earthquakes. Since the sensors are implanted in bedrock, the peak acceleration from even very large local earthquakes should not exceed 0.5 g.

Instrumentation

As a result of collaboration between the Berkeley Seismographic Station Hayward Fault Network, Lawrence Livermore National Laboratory, and Caltrans, a seismic network of twenty-one sensor packages at fifteen sites was installed. Between 1 and 8 instruments have been spaced along the Dumbarton, San Mateo, Bay, Carquinez, and San Rafael bridges (Figure 1). The holes are between 100 and 1000 ft deep and were drilled by Caltrans. The down hole recording package is capable of recording a micro g from local M =1.0 earthquakes to 0.5 g strong ground motion from large Bay Area earthquakes. The Bridges network is part of a larger Hayward Fault Digital Network (Figure 2). This report lists earthquakes and stations where recordings were obtained during the period February 29, 1996 to November 11, 2003. Tables 1-5 list the recording site locations and information for instruments at all bridges in this study.

At the Bay Bridge, six instruments were installed in boreholes and two were operated at the surface. In addition, a temporary surface recorder was installed above the borehole on the east side of YBI near Pier E2 of the SFOBB (BE2U). Figure 3 shows locations of instruments along the Bay Bridge. At the Dumbarton bridge, three instrument sites were utilized: the east (Pier 1) and west end (Pier 44) and Pier 27 near the middle. A sensor was located at the bottom of boreholes at each site. In addition, additional sensors at the surface and at 200 ft were installed. Figure 4 shows location of instruments along the Dumbarton bridge. Figures 5, 6, and 7 show instrument locations along the San Rafael, San Mateo, and Carquinez bridges.

Table 1: Bay Bridge Recording sites

i.d.	sensors	latitude	longitude	Depth(m)	sensor hl, h2 + 090	Recording
SFA	S-6000	37.7861	122.3893	00.0 m,	N143^{0}E	6/98 - present
BBW2	Wil-731A, HS-1	37.79120	122.38525	57.6	N042^{0}E	4/96-present
BBW5	Wil-731A, HS-1	37.8010	122.3737	36.3	N142^{0}E	1/97-present
YBA	Wil-731A, HS-1	37.8094	122.3645	3.0	N150^{0}E	6/98-present
BE2U	S-6000	37.8143	122.3582	0.00	N310^{0}E	1999
BE2D (YBIB)	Wil-731A, HS-1	37.81427	122.35815	61.0	N165^{0}E	7/96-present
BE07	Wil-731A, HS-1	37.81847	122.34688	134.0	N117^{0}E	2/96-present
BE17	Wil-731A, HS-1	37.82086	122.33534	160.0	N168^{0}E	8/95-present
BE23	HS-1	3782167	122.32867	150	N---^{0}E	3/94-10/95

Table 2: Dumbarton Bridge Recording sites

i.d.	sensors	latitude	longitude	Depth (m)	sensor hl, h2 + 090	Recording
<u>Pier 01</u> DWA, DWS DWN DWB	 S-13 Wil-731-200, HS-1 Wil-731-200, HS-1 HS-1, HS-1	37.49947	122.12755	00.0 m, abut. 01.5, Pier 01 71.6, " 228.0, "	 N32^{0}E 000^0 --- 033^0	07/94 - 09/94 09/94 - 09/94 09/94 - 09/94 08/93 - present
<u>Pier 27</u> DMB CAP	 Wil-731, HS-1 Wil-731-200, HS-1	 37.50687 37.517	 122.11566 122.104	 189.2, Pier 27 pile cap, Pier 27	 N020^0	 07/94 - present 07/92 - 11/92
<u>Pier 44</u> DES DEM DEB	 Wil-731-200, HS-1 Wil-731-200, HS-1 Wil-731, HS-1	37.51295	122.10857	 01.5, Pier 44 62.5 157.9	 N000^{0}E ---- 097^0	 11/94 - 09/94 09/94 - 09/94 07/94 - present

Table 3: San Mateo Bridge Recording sites

i.d.	sensors	latitude	longitude	depth	sensor hl, he + 090	Recording
P343	Wil-731A,HS-1	37.59403	122.23242	298.0 m	N0°E	not recorded

Table 4: San Rafael Bridge Recording sites

i.d.	sensors	latitude	longitude	depth	sensor hl, h2 + 090	Recording
P34	Wil-731A, HS-1	37.93583	122.44540	109.0 m		8/97-present
P58	Wil-731A, HS-1	37.93372	122.41313	44.0 m	N0°E	6/97-present

Table 5: Carquinez Bridge Recording sites

i.d.	sensors	latitude	longitude	depth	sensor hl, h2 + 090	Recording
CRQB	Wil-731A, HS-1	38.05591	122.22402	-------	N0°E	6/98-present

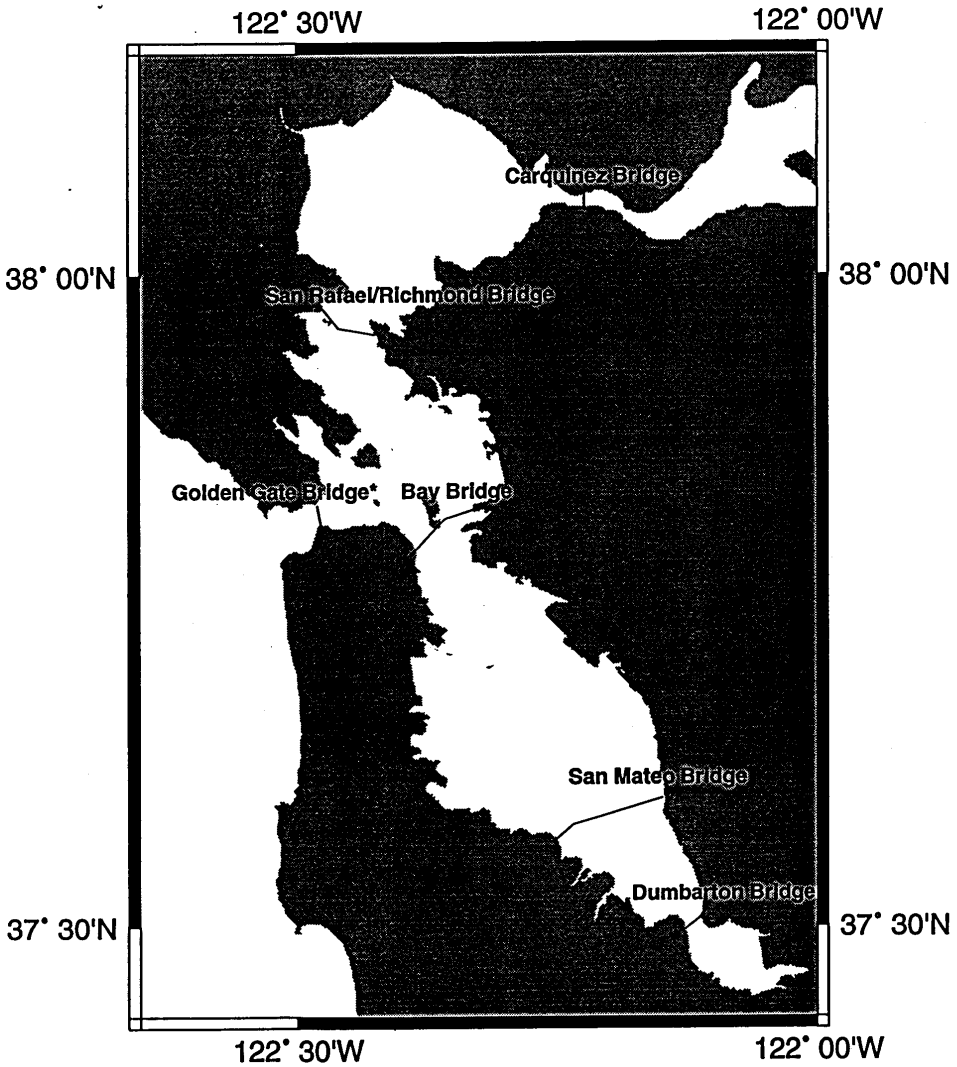

Figure 1: Map of the San Francisco Bay. (*Bridge not used in the bridge network study.)

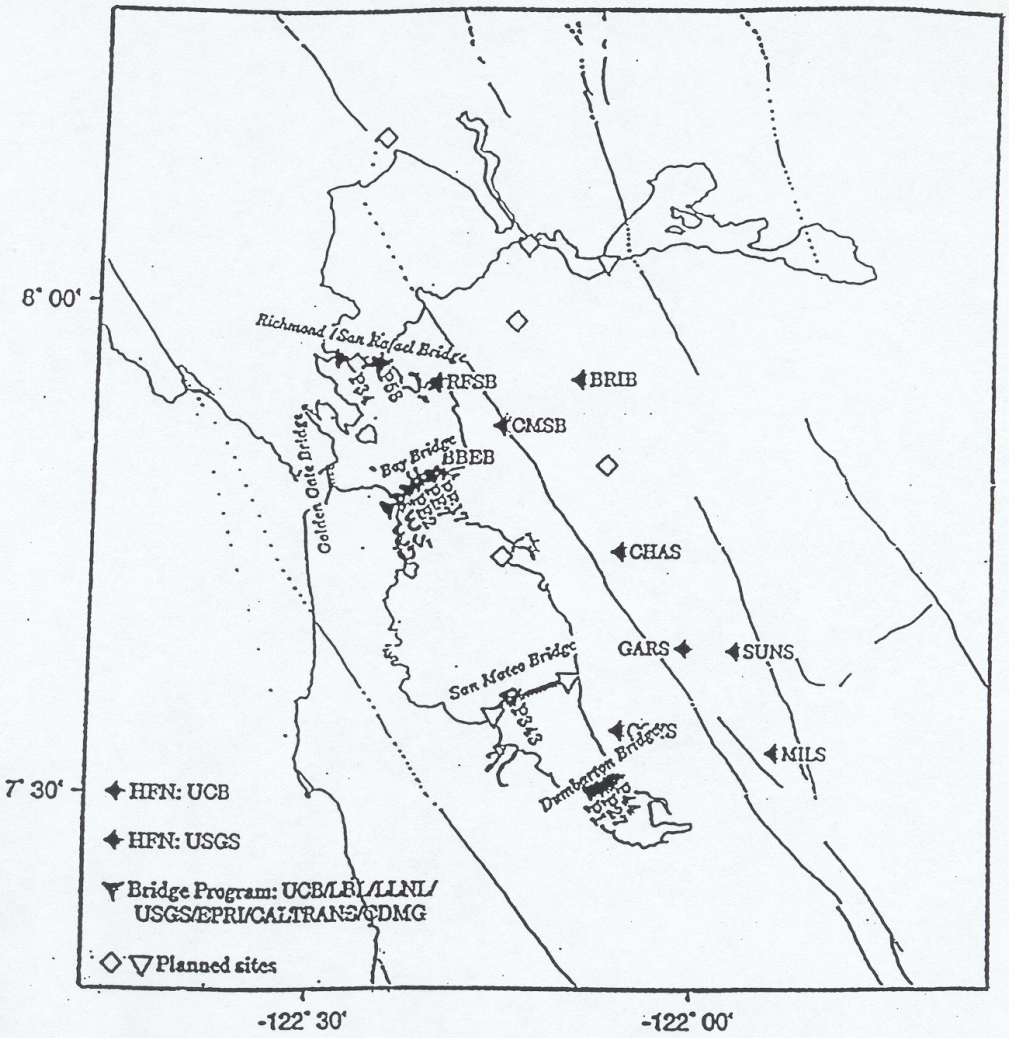

Figure 2: Locations of Bay Area Borehole Network. Instruments are placed 100' into bedrock.

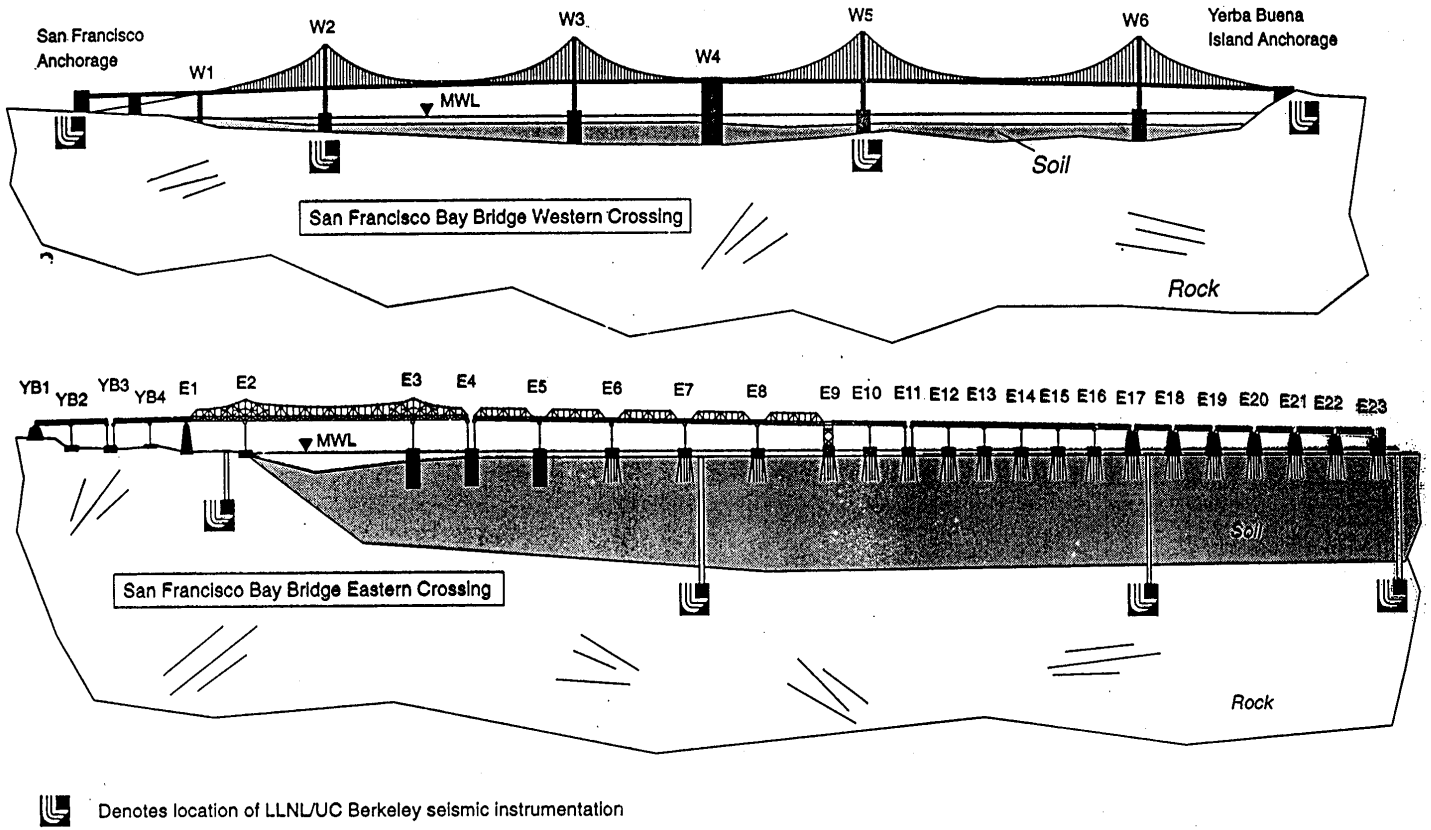

Denotes location of LLNL/UC Berkeley seismic instrumentation

Figure 3: Location of LLNL/UC Berkeley seismic instrumentation along the San Francisco-Oakland Bay Bridge.

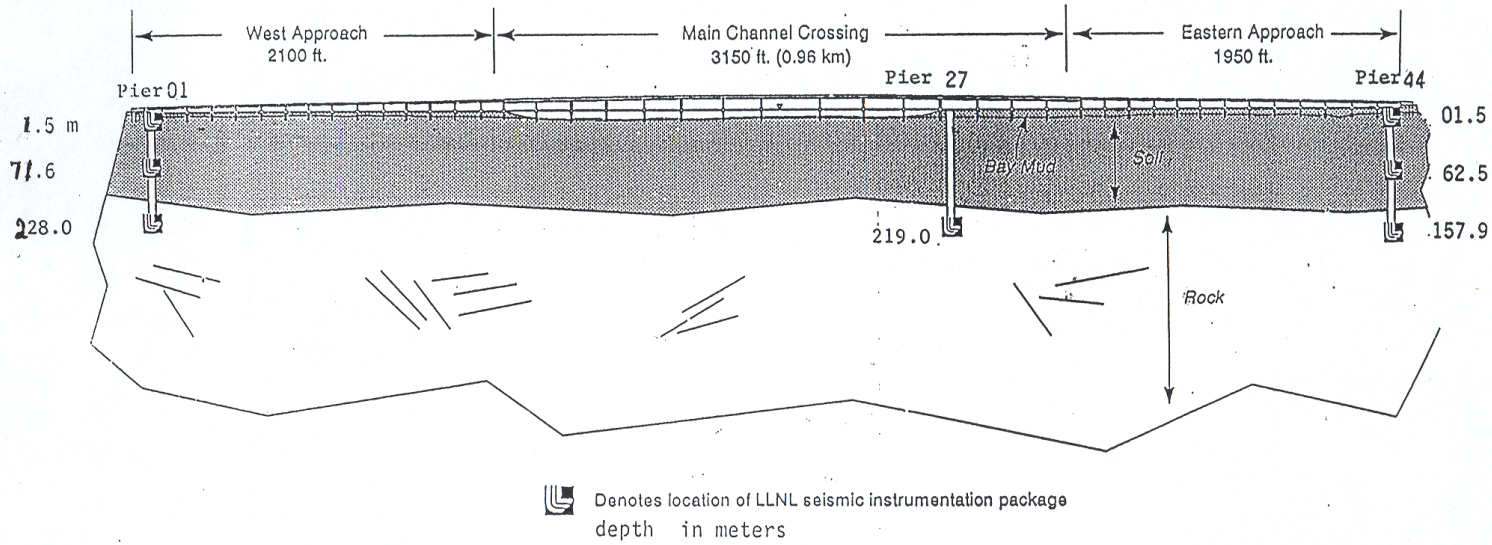

Figure 4. Location of the LLNL seismic instrumentation along the Dumbarton Bridge.

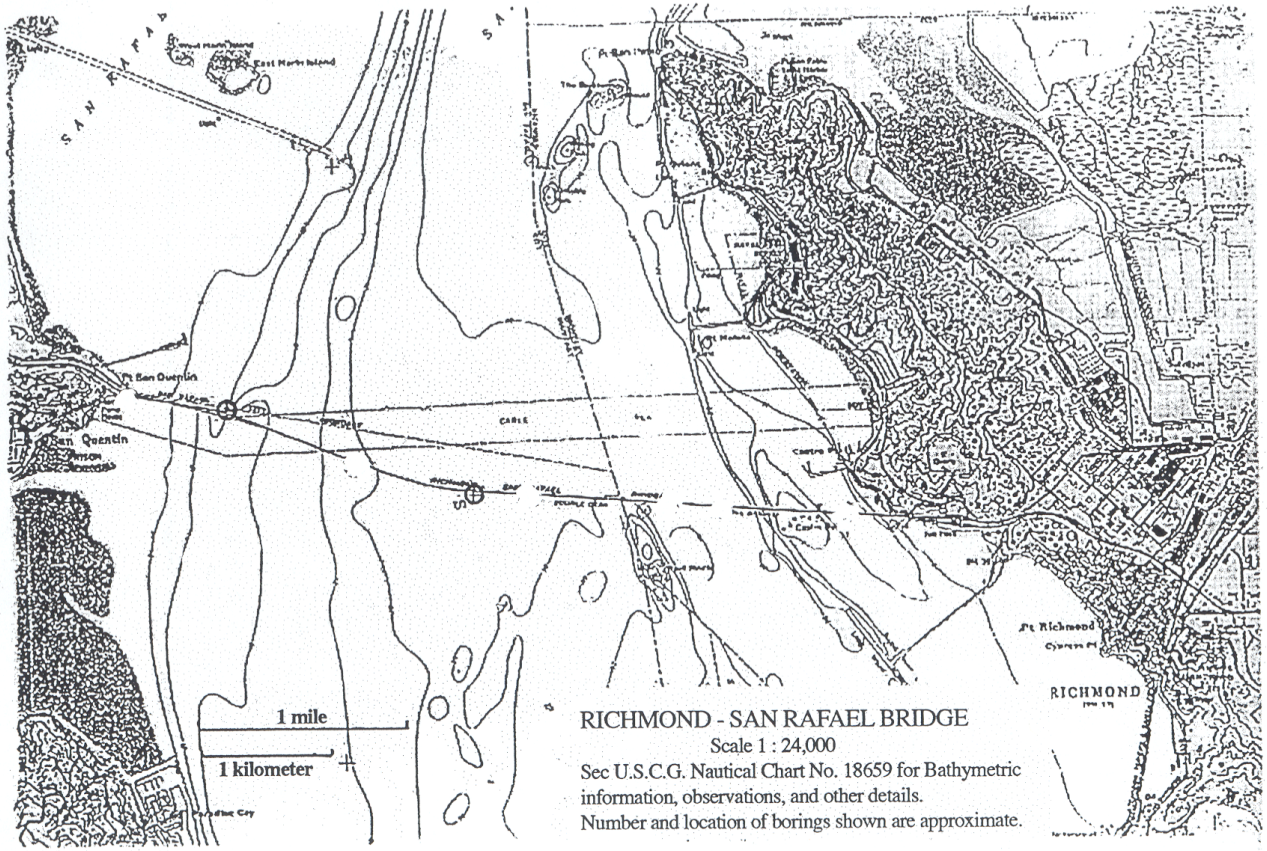

Figure 5: Location of seismic instrumentation along the Richmond-San Rafael Bridge.

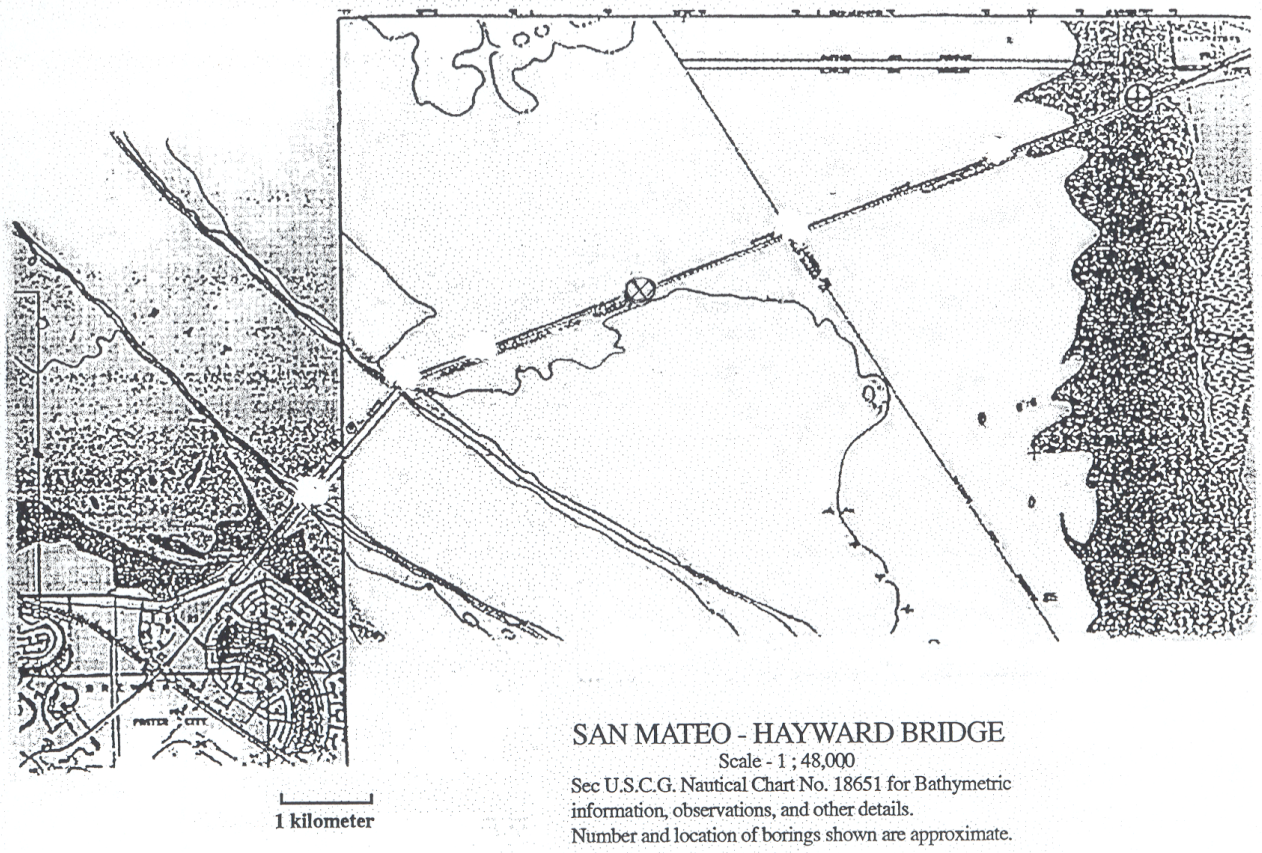

Figure 6: Location of seismic instrumentation along the San Mateo-Hayward Bridge.

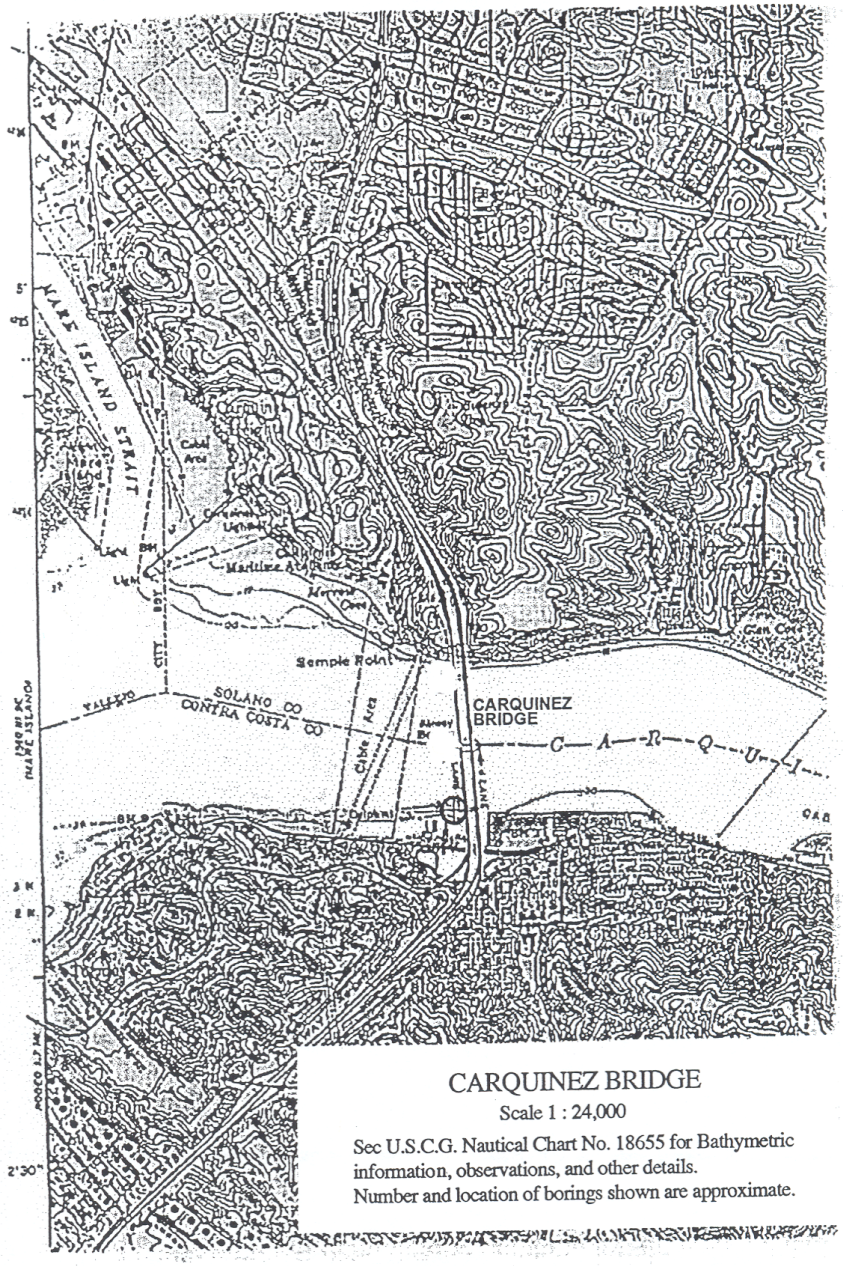

Figure 7: Location of seismic instrumentation along the Carquinez Bridge.

Sensor Description

The down-hole sensor packages were manufactured at LBL under the direction to Dr. Tom McEvilly, and is the same package used by the USGS and LBL for the Hayward Fault Digital Recording Network. This package contains three orthogonal Oyo HS-1 4.5 Hz geophones and three orthogonal Wilcoxon 731s l0v/g accelerometers. The dynamic range of the Wilcoxon package is from a micro-g to 0.5 g acceleration, and is flat to frequency response from 0.1 to 300 Hz. This allows recording of M =1.0 to 0.5 g strong ground motion from large Bay Area earthquakes. Typically, the Wilcoxon's are recorded over two dynamic ranges to capture weak and strong ground motions, and HS-l's are used as a backup for weak ground motion recording. Portable Refraction Technology 72A Data Acquisition Systems with 16 bit resolution and 200 Hz sampling are used to record the data at most sites. Three sites utilize Quantera-4120 24-bit resolution data loggers with 500 Hz recorders. The data is processed and managed at UC Berkeley.

We have removed the instrument response of each system to get ground motion to the frequency limit of the systems. The Wilcoxon accelerometers and Quanterra recorder (downhole system) are flat for acceleration from 0.1 Hz to the anti-alias filter at 100 Hz. The low frequency limit is from a high pass filter in the power box. It is down 3 db at 0.1 Hz and rolls off at 6 db per octave. The sensor has a roll-off at 0.05 Hz. The data was corrected for the 0.1 Hz high pass filter, so it is band limited by the sensor roll-off. A portable Refraction Technology 72A Data Acquisition Systems with 16-bit resolution was used to record the S-6000 seismometer at BE2U. The reftek recorder has a roll-off at 250 Hz and imposes an anti-aliasing filter at 40% of the sampling rate. We sampled the reftek data at 200 sps, so it has a band limit of 80 Hz. The S-6000 seismometer is flat to velocity to at least 100 Hz and rolls off at the low frequency end; it is down 3 db at 2 Hz and rolls off at 12 db per octavo. We have corrected for this high pass filter, so that the response is effectively flat to DC.

Sensor Orientation

We obtained an estimate of the orientation of the sensors by examining P-wave particle motion. We rotated the horizontal components until all P-wave motion was on one horizontal component, and assumed this was in a radial direction from the earthquake. Table 6 lists events used and calculated orientations at the Bay Bridge sites; the average values are listed in Tables 1-5. Figure 8 shows the original and rotated records from station BE2D for event 12/04/98 (Table 6). The T1 marker shows the limit at which the first arrival is considered uncontaminated by secondary arrivals.

Table 6: Sensor Orientation Calculations, Bay Bridge

Orientations of up on channel 2; ch3 = ch2 + 090; Channel 1 is vertical, positive down, except **	SFA**	BBW2	BBW%	YBA**	BE2D	BE2U	BE07	BE17	BE23
9812041216	N143E	N042E	N142E	N150E	N165E	N310E	N117E	N168E	
+prior 08/24/99 since 08/24/99 *prior 01/15/97 since 01/15/97	N131E N136E					 N143E N310E			
Vertical									
vertical: up on channel-1	UU	DD	DD	DD	DD	UU	DD	DD	

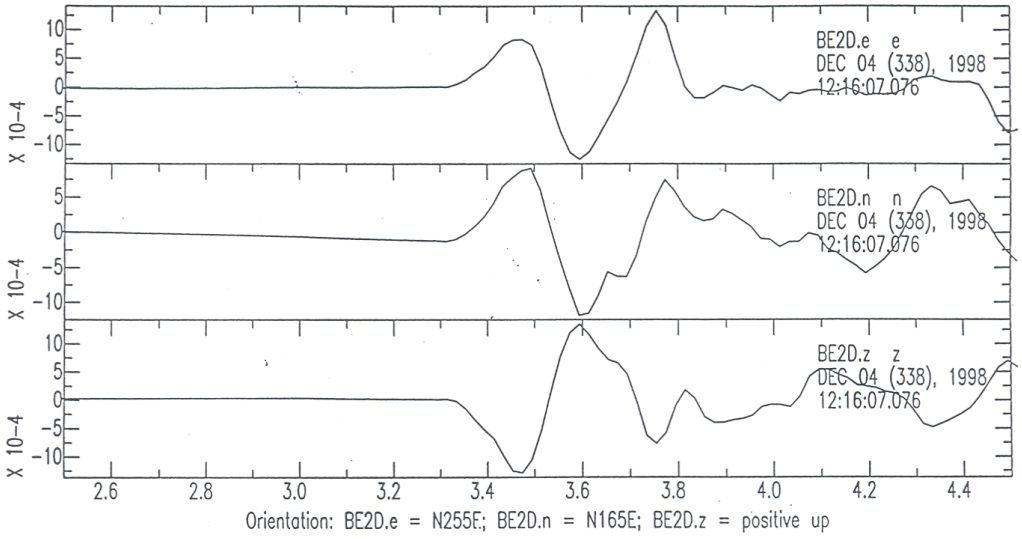

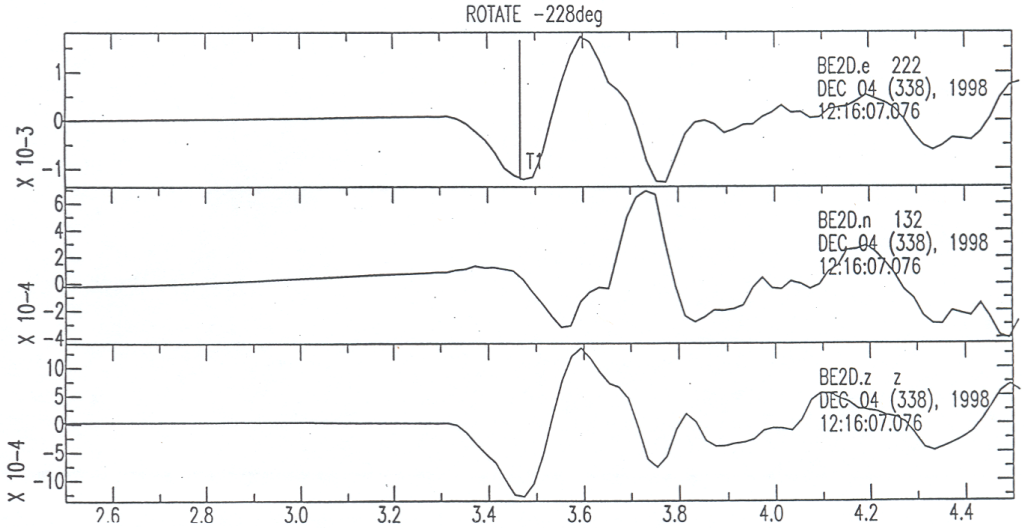

(b)

Figure 8: (a) original record from station BE2D for event 12/04/98, (b) rotated record.

Signal to Noise Ratios

For weak motion recordings, the noise in the signal is often the limiting factor for site response studies. The SNR for several earthquakes in this study was calculated by estimating the spectral content of the first 20 to 30 seconds of the record (depending on the length of noise recorded prior to the earthquake signal) and a similar length of the earthquake signal. The two components of horizontal motion were combined into a complex signal as described by Steidl et al (1996). Fourier amplitude spectra of velocity records are used for the analysis. The Fourier signal amplitude spectrum was then divided by the Fourier noise spectrum for that earthquake. The SNR was calculated for the uphole and downhole recorded motions at Yerba Buena Island.

Figure 9 shows the noise and signal spectra for both the uphole and downhole velocity recordings for a magnitude 4.1 earthquake at 15 km distance. This is one of the largest and closest recorded earthquakes and demonstrates the high quality of data that can be recorded. The uphole and downhole recordings are limited by instrument noise at 0.3 Hz at the low frequency end for the different components, and at 40 Hz at the high frequency end. The downhole recording is limited by instrument noise at 0.2 Hz and cultural noise at 60 Hz for the low and high frequency limits, respectively.

Figure 10 shows the velocity noise and signal spectra for both the uphole and downhole recordings for a magnitude 2.6 event located 31 km away from YBI and is near the recording limit of the network. The uphole recording is limited to frequencies 0.7 to 14.0 Hz and the downhole SNR is below three at all frequencies.

Examination of the noise and signal spectra for all 18 events studied results in the following conclusions. The SNR for the uphole recordings was generally greater than 3 over a frequency range of 0.5 to 30 Hz. The downhole recordings had a much smaller usable frequency range with SNR equal to or above 3, from 1 to 8 Hz. However, the usable frequency range varies over the recorded earthquakes. The earthquakes with magnitudes greater than or equal to 3.0 tended to have a wider frequency band of high SNR.

One of the potential advantages to downhole instruments is the reduced cultural noise Unfortunately for most of the recorded events in this study, instrument noise is more of a controlling factor. Because the YBI uphole and downhole instruments are different, the usable frequency band is also different for each instrument. The downhole Wilcoxon 731s 10v/g accelerometer can be limited by noise at low frequencies, generally below 1 H z, except for the larger events in the study where the SNR is greater than 3 down to 0.3 Hz. On the other hand, the uphole S-6000 seismometer is less limited at the low frequencies down to 0.2 Hz in some cases but can be limited at high frequencies for small amplitude events. In particular, the S-6000 has a significant increase in noise for frequencies above 30 Hz. The Wilcoxon instrument has less instrument noise at the higher frequencies and therefore results in a higher SNR above 10 Hz than the downhole instrument. So unfortunately for this uphole/downhole pair, the uphole instrument is limited by noise for high frequencies and the downhole instrument is limited at low frequencies when recording weak motion. Both instruments have high SNR for the larger earthquakes.

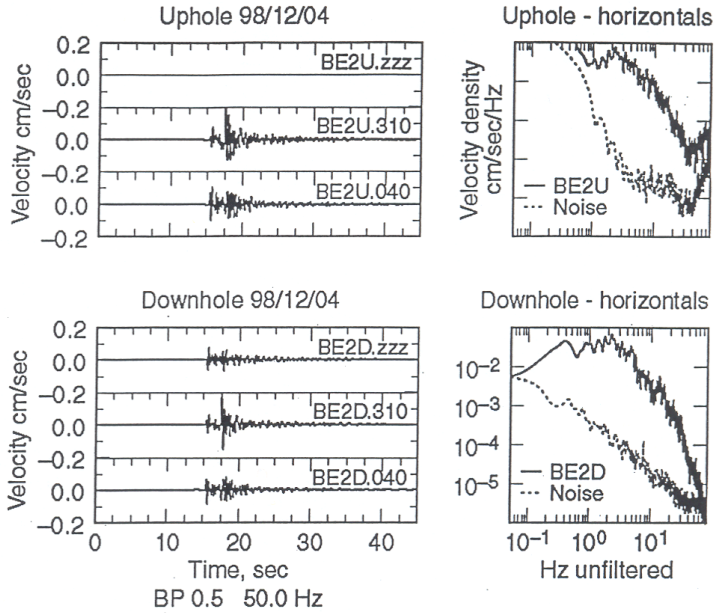

Fig. 9 Time series and Fourier amplitude spectra for a magnitude 4.1 earthquake on the Hayward fault, 15 l distant. Noise spectra are also shown. The uphole and downhole recordings are limited at 0.3 Hz by instrument no at the low frequency end, and at 40 Hz at the high frequency end, by cultural noise.

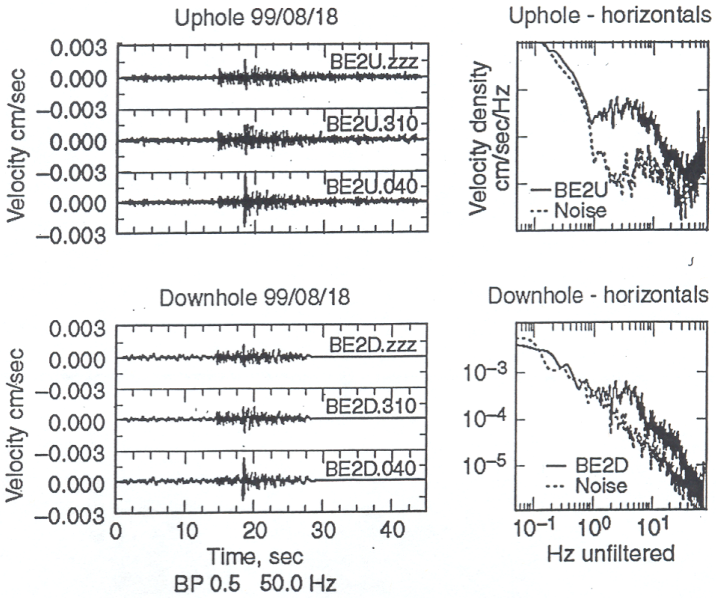

Fig. 10 Time series and Fourier amplitude spectra for a magnitude 2.6 earthquake recorded at the top and bottom of the borehole. Noise spectra are also shown. Cultural noise significantly reduces the usable frequency range.

Geology of San Francisco Bay

The San Francisco Bay is a shallow sedimentary basin bounded on the east and west by parallel ranges of the northwest trending Coast Ranges, and by the Hayward Fault and on the west by the San Andreas Fault on the east (Figure 11). YBI lies roughly midway between these two important faults, a bedrock knob in the middle of the San Francisco Bay.

The warping and faulting was caused by tilting blocks along fault zones, the eastern depressed edge of the San Francisco-Mann block lying against the uplifted Berkeley Hills block. The bay is affected by the San Andreas Fault system to the west and the Hayward fault system to the east. During the earlier part of the upper Pleistocene, the whole body of present hill lands, from the immediate bay region to the Great Valley, were slowly uplifted allowing the main river (Sacramento River combined with the San Joaquin River) to maintain its course toward the ocean. During or near the same time, similar uplift occurred to the west of the bay valley, cutting the Golden Gate canyon to a depth of more than 350 feet, thus creating the deepest part of the bay. Today, strong tidal currents within the Golden Gate canyon prevent deposition of mud and thus allows the deepest portions of the canyon to be floored by bedrock. This bedrock is though to represent the bottom of the main river as it flowed through the canyon towards the Pacific Ocean.

San Francisco Bay is composed of two distinct units; bedrock and a younger unconsolidated sediment sequence which can be further subdivided into the Alameda formation (oldest), San Antonio formation, Posey formation, Merritt formation and the Bay Mud (youngest). Figure 11 shows the subsurface geology beneath the San Francisco Oakland Bay Bridge. (Trask, P and Rolston, R., 1951, *Engineering Geology of San Francisco Bay, California:* Bull. Geol. Soc. Am.: v. 62, pp. 1079-1110.) These characterized here. The Franciscan material seismic velocities range from 4.3 to 6.1 km/s (Vp) and are slightly lower in the upper 100 m. The uphole/ downhole pair in this study are both located in the Franciscan mélange (Turpin, 2000).

The sedimentary sequence adjacent to the bedrock island in the San Francisco Bay includes normally consolidated clays, sands, and over-consolidated clays. To the east of the island the sedimentary layer reaches a depth of 200 m and to the west only a depth of 20 m. Treasure Island, a man-made island, is located north of YBI.

Unit	**Geologic Characteristics**
Bedrock	Composed of the Franciscan formation (Mesozoic). The Franciscan formation contains interbedded feldspathic sandstone, graywacke, siltstone, shale, limestone, radiolarian chert, metavolcanic rocks, and glaucophane schists. The total thickness of this unit is unknown but has been estimated to be at least 10,000 feet thick and at most 50,000 feet thick. (Figure 11).
Alameda formation	Composed of layers of firm sand, silt, clay, and fine gravel. The formation commonly appears gray but can be greenish gray or brownish gray. The gravel contains well rounded pebbles (up to lin in diameter) from the Franciscan formation. Plant fragments can be found throughout the unit but seem to be heavily concentrated within the upper portion. On the west side of the San Francisco Bay, at a depth of ~280 feet, a layer of clean white volcanic ash is interbedded within the unit. The volcanic ash is a dacitic vitric tuff which contains 10% crystals (feldspar, hornblende, quartz) and 90% glass.
San Antonio formation	The unit can be divided into three distinct layers. The first layer consists of a firm silty clay. The second layer contains fine- to medium-grained sand and silty clay with shell fragments. The second layer is not found on the western side of the San Francisco Bay. The third layer is composed of gray to greenish gray fine grained clay with interbedded layers of sand or sandy gravel containing Franciscan pebbles. This layer contains a continuous bed of plant fragments near the base.
Posey formation	Composed of firm sandy clay and fine- to medium- grained sand. It contains very round Franciscan pebbles up to l inch in diameter. It is often misidentified as the Merritt formation.
Merritt formation	Composed of a well sorted, medium grained, sand. It partially fills deep valleys carved into the underlying Posey and older formations. In some areas the Merritt formation consists of clay and well sorted silt.
Bay Mud	Consists of soft mud composed of gray silty clay, silty sand, and occasionally interbedded thin sand layers. The mud becomes firmer and contains less water as depth increases. The clay contains mica, montmorillonite, chlorite, kaolinite, quartz, and feldspar.

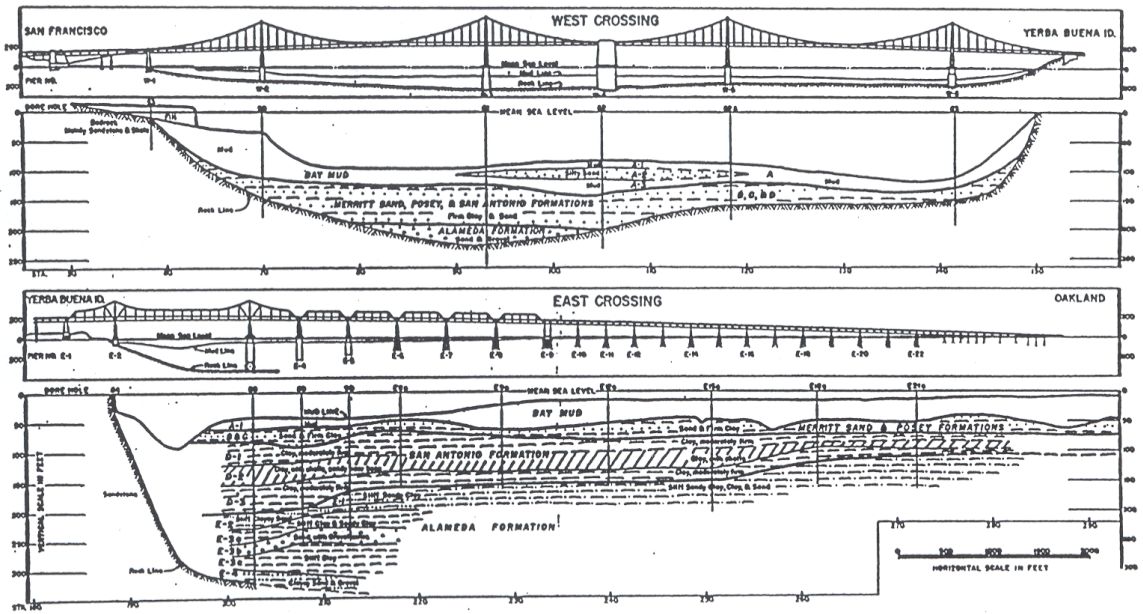

Figure 11: Subsurface geology beneath the San Francisco- Oakland Bay Bridge as inferred by Trask and Rolston (1951) and later updated by Rogers and Figures, 1991, *Engineering Geologic Site Characterization of the Greater Oakland- Alameda Area, Alameda and San Francisco Counties, California* : NSF Report, p. 46.

Bay Bridge Microearthquake Analysis
Source Corner Frequency

When spectra are plotted for events of differing magnitudes, the observed source corner frequency is expected to vary directly with magnitude. This is not the case for the spectra at YBI. Rather, most of the spectra show an apparent corner frequencies between 2 and 7 Hz, regardless of magnitude. This apparent corner frequency is the same for uphole and downhole spectra. Figure 12 shows spectra from events 9811030602 and 9902040021 with magnitude 2.4 and 3.7, respectively. Horizontal spectra of the signal and noise have been vectorially added. The corner frequency from a fit by eye is 6 and 5 Hz, respectively. Even though the magnitude 3.7 event is much larger and greater distance the frequencies are about the same. Hutchings (1991, Figure 3) plotted spectra of aftershocks, with magnitudes near 3.0, of the Loma Prieta earthquake recorded at YBI and they all had corner frequencies near 5 Hz. Table 7 lists the events recorded by this study.

We applied the program Specfit (Lindley et al., 1992) to the spectra to identify the Brune corner frequencies and found that the source corners are much higher than the apparent corners. A propagation path t* of about 0.1 was necessary to describe the spectra. Since, several sites are necessary to quantitatively identify the Brune source corner (Hutchings, 2001) and that is not the purpose of this paper, we only identify the apparent corner frequencies and analyze their implications. Corner frequencies are picked by eye because we are not attempting to fit the spectra to a specific model, rather to generalize their characteristics. Corner frequency picks for stations BE2U and BE2D of all the events obtained by an eyeball fit as was done, and corner frequency picks are all between 1 and 7 Hz. Figure 13 shows a plot of the corner frequency picks (triangles) as a function of moment (using the moment magnitude relation of Bakun, 1984), along with the prediction of corner frequencies with a Brune (1972) source model, stress drop of 100 bars, and source shear velocity of 3.0 km/sec. Only events with moment above about 1.0 x 10^{21} dyne-cm have corner frequencies near what would be expected from a Brune source model.

The constant corner frequencies could be explained several ways. First, there could be a breakdown of a constant stress drop Brune source model that calls for corner frequencies to increase with decreasing magnitude. Several authors have identified constant corner frequencies for small events and attributed it to a minimum source dimension for earthquakes, which results in a decrease in stress drop for smaller events (Archuleta et al., 1982; Papageorgiou and Aki, 1983).

An alternative explanation is that the constant low corner frequencies results from high whole path attenuation, or a local site effect at YBI, removing the high frequencies from the signals uniformly over the various events. Several studies have shown that corner frequency estimates from surface recordings are limited to a maximum value due to near site attenuation (Hanks, 1982, Anderson and Hough, 1984, Hutchings, 1990). Here it may be true for borehole records as well. A whole path Q effect would be greater for larger hypocentral distances; therefore, the corner frequencies are plotted against hypocentral distance in Figure 13. Corner frequency versus event azimuth is also plotted in the Figure 13. As evident from the figure, a relationship between hypocentral distance or azimuth and corner frequency does not appear to exist.

Table 7: Event Information and Spectral Parameters

Earthquake	ID	Latitude	Longitude	D	M	data band BE2U	data nd BE2D	fa Be2 U	fa Be2 D	fh BE2 D	Hypo Dist	Back Azm	Fault
1997/08/14 38:53	EV1+	37.737	-122.548	1.8	3.0	.6-40	.6-30	2	2	10	18.9	243	San Andreas
1997/10/27 14:30	EV2	37.727	-122.547	10.2	2.9	.7-60	2-10	6	6	-	21.8	240	San Andreas
1997/11/19 21:05	EV3+	37.619	-122.016	4.8	3.2	3-40	1-30	4	4	13	37.5	211	Hayward
1998/01/17 10:00	EV4+	37.811	-122.193	4.5	2.4	.4-40	3-20	4	4	10	15.2	92	Hayward
1998/10/20 12:46	EV5	37.878	-122.246	10.0	2.1	.6-30	20-30	7	-	-	15.7	55	Hayward
1998/10/22 01:28	EV6	38.525	-122.303	8.3	3.0	.2-20	1-6	3	3	-	79.5	4	Lake Co.
1998/10/22 19:49	EV7	37.945	-122.307	7.6	2.5	.7-10	20-30	7	-	-	17.0	17	Hayward
1998/11/03 06:02	EV8	37.876	-122.243	9.5	2.4	.7-20	5-8	7	-	-	15.5	56	Hayward
1998/12/04 12:16	EV9+	37.920	-122.290	6.8	4.1	.3-40	.3-40	2	2	10	14.8	27	Hayward
1999/01/26 06:02	EV 10	37.914	-122.288	4.7	2.0	1.3-7	NR	6	-	-	13.5	29	Hayward
1999/02/04 00:19	EVl1+	37.160	-121.554	6.1	3.9	.3-20	.4-20	3	4	NH	101.8	136	Hayward
1999/02/04 00:21	EV12+	37.161	-121.555	6.1	3.7	.5-15	.5-15	4	4	NH	101.7	136	Hayward
1999/04/04 06:00	EV13	38.843	-122.757	4.0	3.8	.3-10	.4-8	3	3	-	119.5	343	Rodgers
1999/06/23 23:48	EV14	37.874	-122.244	9.8	2.0	1-30	5-8	4	-	-	15.5	57	Hayward
1999/07/24 05:28	EV15	37.756	-122.138	7.8	1.9	1.5-15	NR	4	-	-	21.9	109	Hayward
1999/08/12 08:16	EV16+	37.866	-122.245	6.5	2.5	.9-40	3-40	3	-	8	13.2	60	Hayward
1999/08/18 01:06*	EV17+	37.907	-122.687	6.7	5.0	.3-60	.3-60	1	1	10	31.4	289	San Andreas
1999/08/18 06:44	EV18	37.915	-122.674	7.2	2.6	.7-14	NR	4	-	-	30.8	292	San Andreas

*clipped on the N310 component at BE2U
+used in spectral ratio study
D is depth of event
M is magnitude
NR no band had an acceptable ratio
NH no spectral hole identified
fa is the corner frequency estimate from a Brune source model
fh is the frequency of the spectral hole in the downhole component

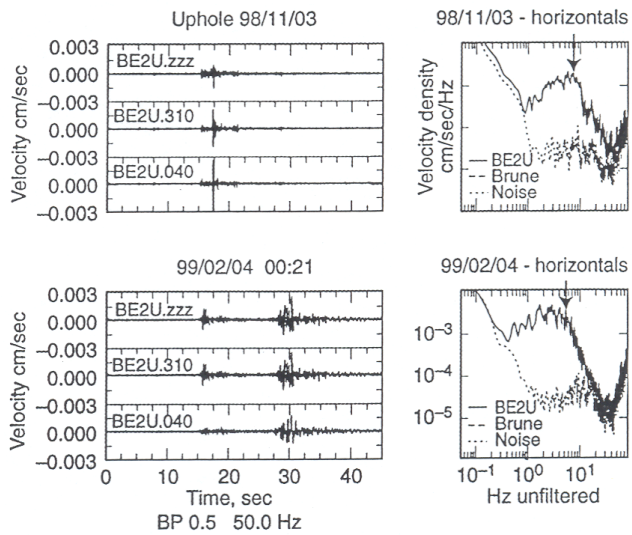

Fig. 12 Time series and Fourier amplitude spectra for a magnitude 2.4 (top) and a magnitude 3.7 (bottom) earthquake recorded at the top of the borehole. Notice the similarity of the shape of the spectra. The corner frequencies fit by eye are 6 and 5 Hz, respectively. Even though the $M = 3.7$ event is much larger and occurred at a greater distance than the $M = 2.4$ event, the corner frequencies are about the same.

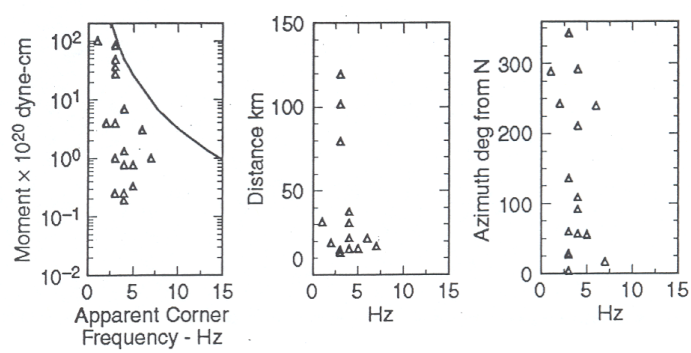

Fig. 13 Plots of moment (left), distance (center), and azimuth (right) as a function of corner frequency for all the events listed in Table 1. Also shown is the prediction of corner frequencies with a Brune (1972) source model (left) with stress drop of 100 bars. Only events with moment greater than 1.0×10^{21} dyne-cm have a corner frequency near the predicted.

In summary, any one of these causes could result in a constant frequency corner at YBI and the nearby stations. However, a wide body of literature has refuted the constant corner frequency observed for small earthquakes as being a source effect (Anderson and Hough, 1984; Hutchings, 1990; Blakeslee and Malin, 1991; Aster and Shearer, 1991; Abercrombie, 1995). Whole path attenuation doesn't appear to be the factor in this study, and site-specific site effect at YBI doesn't appear to be the cause either. We suspect, but cannot prove, that constant corner frequencies for the small events are due to attenuation caused by propagation through the highly heterogeneous basement Franciscan formation beneath the recording sites in the San Francisco Bay. Further study is required to fully resolve the issue.

December 04,1998, M=4.1 Event

We have performed a detailed analysis of records from the December 04,1998, M=4.1 event (Table 1 This event occurred on the Hayward fault approximately in-line with the bridge, and was recorded on all operating sites (BE23 was temporary out of operation). Figure 14 shows the location of the event and the recording sites. Figure 15 shows the transverse component of velocity at all sites (except BE23) across the bridge, and Figure 16 shows the transverse component of displacement. Records have been band-passed between 0.3 and 25.0 Hz. This is the effective frequency range of these recordings.

There was a timing problem at sites BE17, YBA, and SFA for this earthquake, where docks did not receive absolute GPS time. Start times were corrected by interpolation for site BE17 and YBA, and by extrapolation for site SFA. This was verified by comparison to relative times for events from other events when the GPS times were locked in. We identified a problem with a horizontal component at station BW02.132 at the Bay Bridge. This is evident when the spectra are compared to nearby sites from the same earthquake, and their components have been rotated to that of site BW02. Figure 17 shows spectra from BW02.132 and rotated BW05.132. Recordings at BW02.132 are about a factor of two too small at all frequencies. This factor has been multiplied into recordings for analysis. We have no explanation for this problem.

Site Response Transfer Function at Yerba Buena Island

We utilized the 18 events that were recorded on both the top and bottom of borehole sites at Yerba Buena Island, BE2U and BE2D (Table 7). We tested the spectral ratio, cross-spectrum, complex signal, and horizontal to vertical (HVSR) spectral ratio methods to obtained site response and transfer functions (phase included), (Baise et al., 2001). We identified a spectral hole in the down-hole records. This “hole” resulted in an apparent amplification when spectral ratios were taken between the bottom and top of the borehole We found that the complex signal method had the lowest variance for both and best predicted observed ground motions at the surface when the down-hole site was used as input. The HVSR best revealed the lack of site response at YBI, and calculations with just background noise gave just as good results as with seismic signals. Figure 18 shows the horizontal components for up (BE2U) and down (BE2D) recordings for a M=4.1 event and the mean and +/- standard deviation of the spectral ratios of the 18 events. The ratio is near one for frequencies less than about 5 Hz and this is the frequency range where the free surface effect is not occurring for long period arrivals. Figure 19 shows the results if only the surface recordings are used in the P-SV approach. The P-SV approach identified the resonances, but not the amplifications.

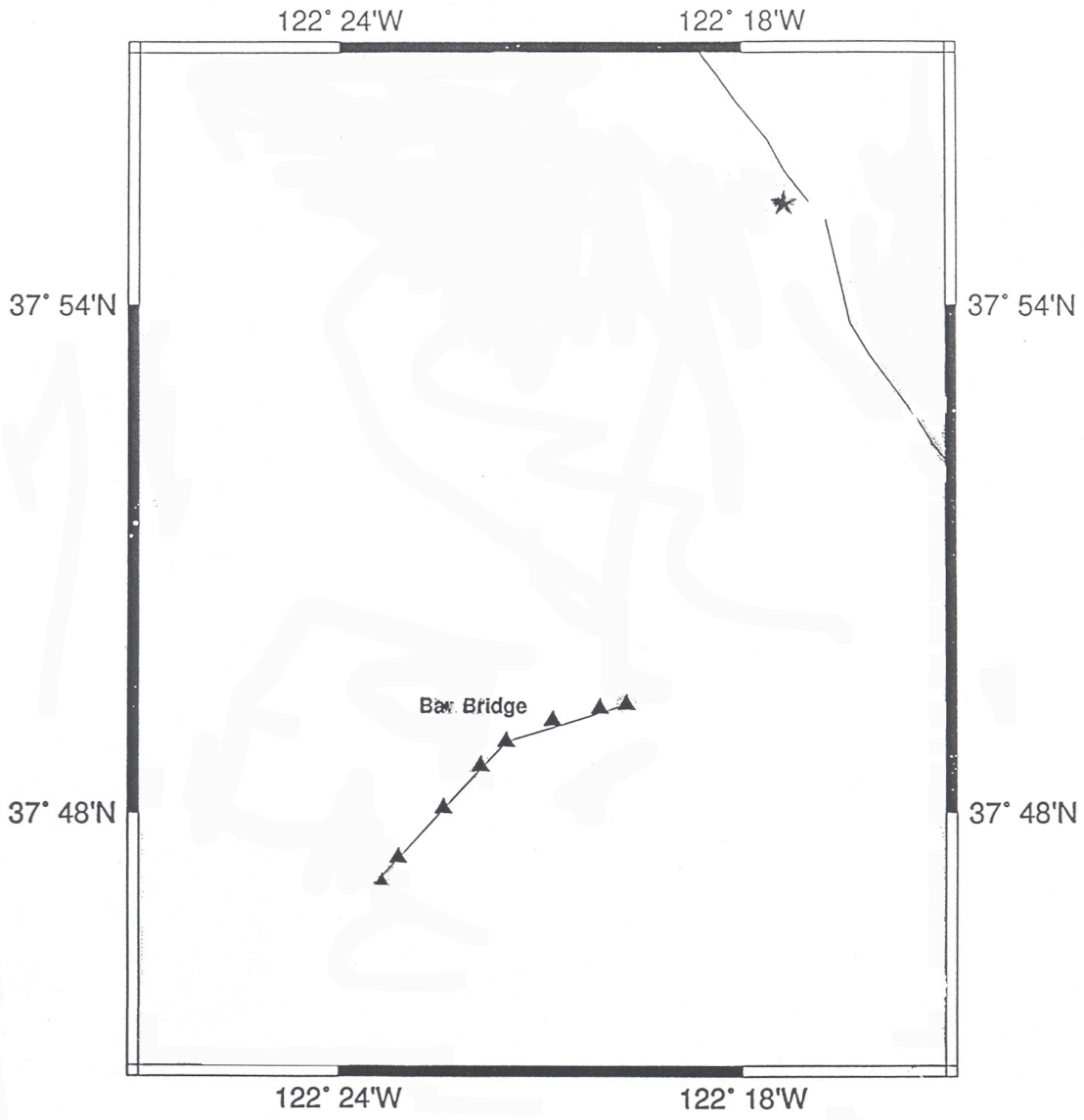

Figure 14: Locations of stations recording the December 4, 1998 event.

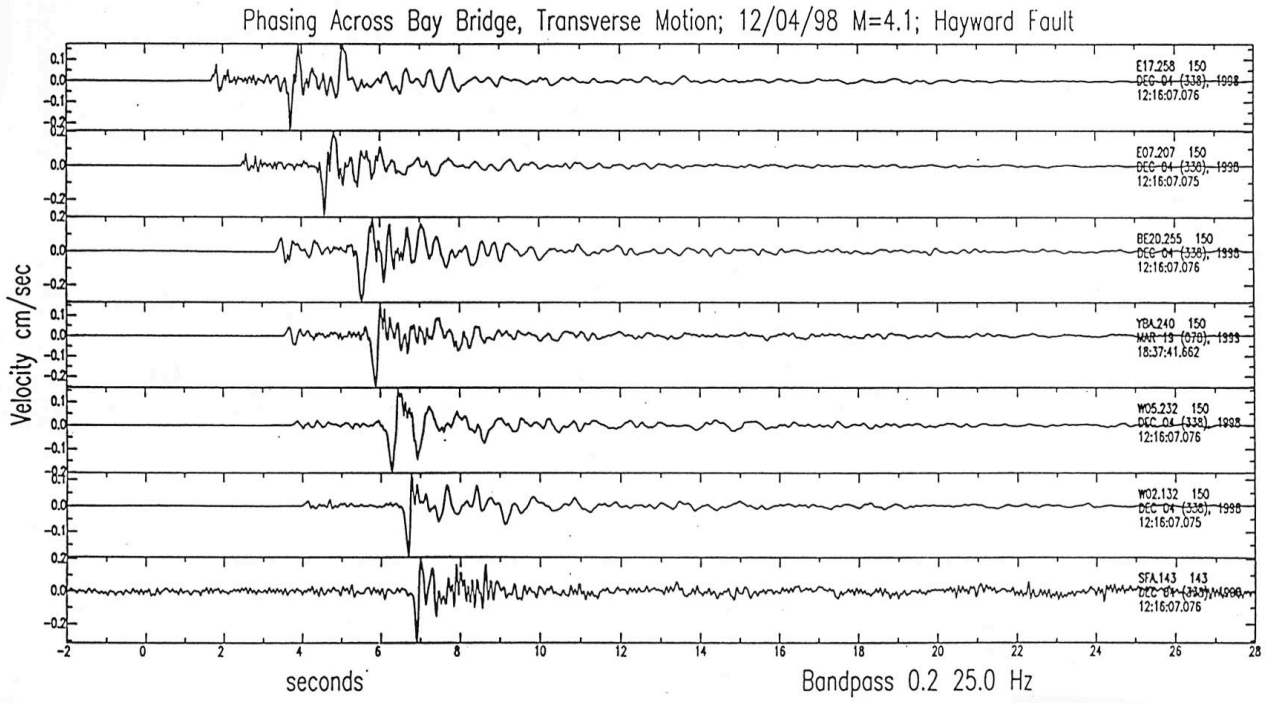

Figure 15: Velocity record of event December 04, 1998 recorded at the stations shown in Figure 14, transverse component.

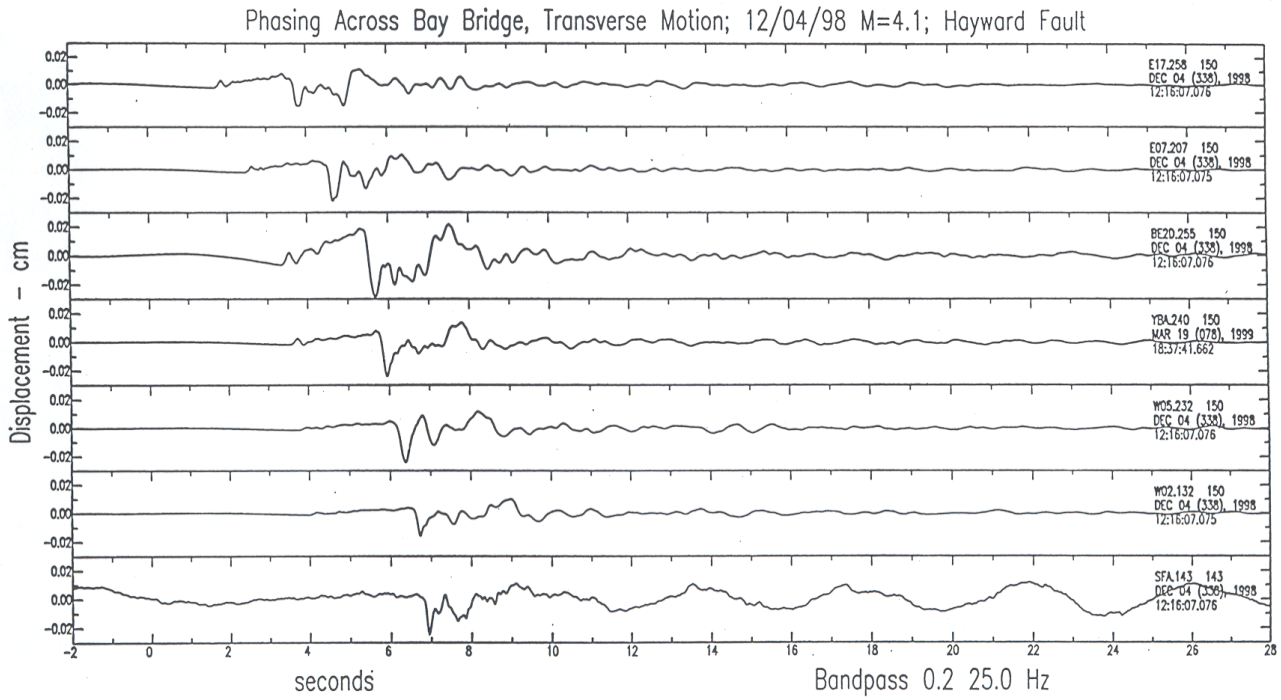

Figure 16: Displacement record of event December 04, 1998 recorded at the stations shown in Figure 14, transverse component.

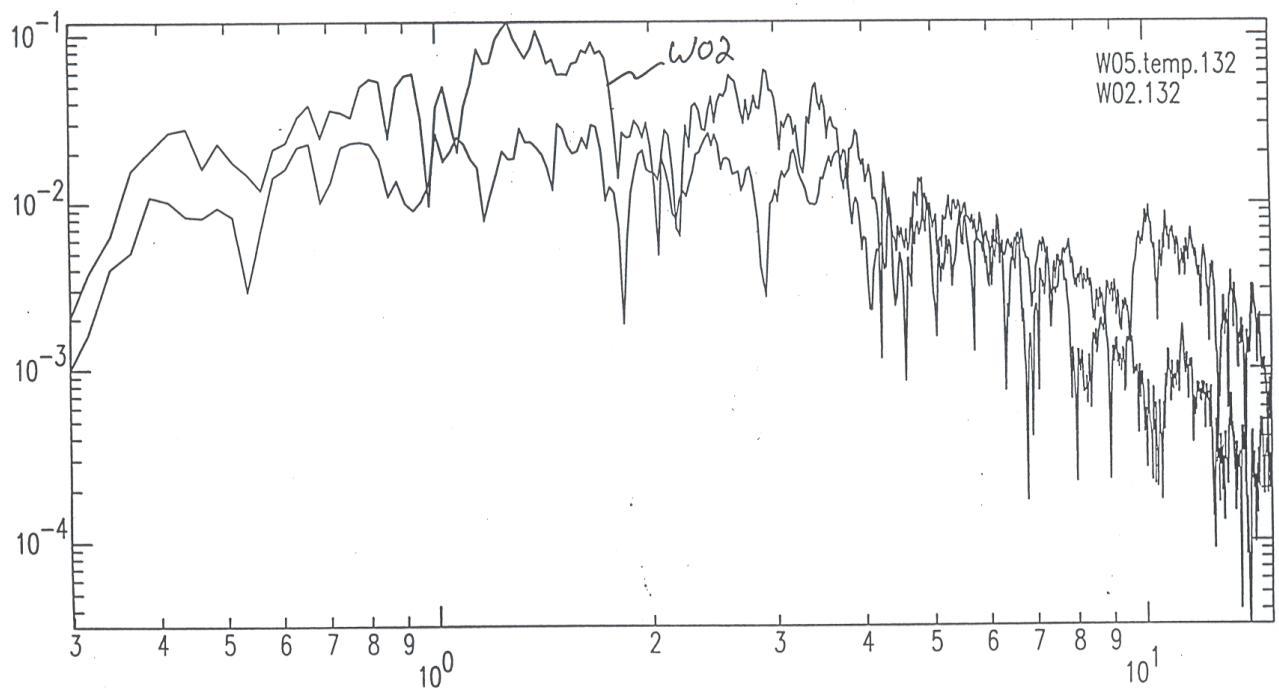

Figure 17: Spectra from BW02.132 and rotated BW05.132. Recordings at BW02 are about a factor of two too small all frequencies..

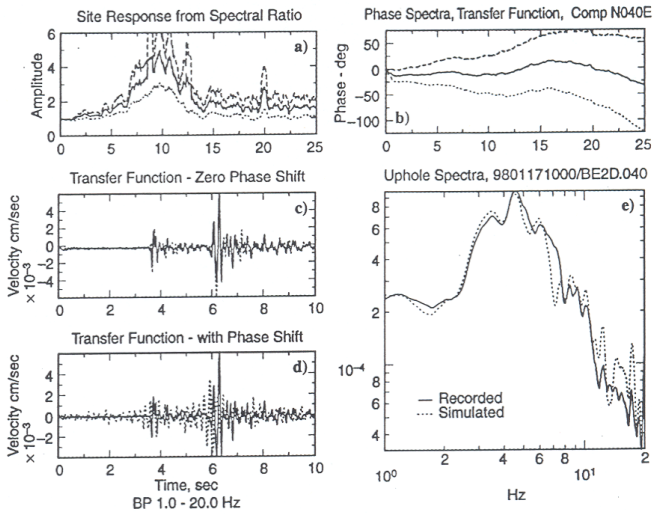

Fig. 18 - (a, b) Estimated horizontal-average site response function for eight events plotted with 95% confidence intervals. (c) Observed and simulated surface motion for EV4, N040E component, using the observed downhole motion as input and zero phase shift in the transfer function. (d) Using phase in the transfer function. (e) Corresponding observed and simulated spectra.

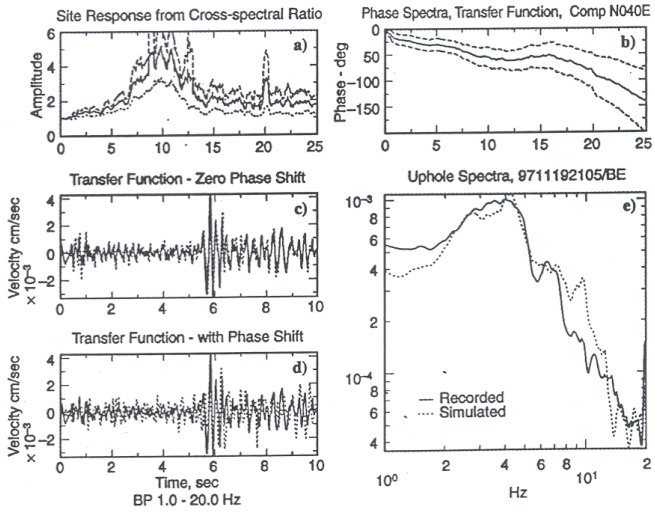

Fig. 19. (a, b) Estimated cross-spectra site response function for eight events plotted with 95% confidence intervals. (c) Observed and simulated surface motion for EV3, N040E component, using the observed downhole motion as input and zero phase shift in the transfer function. (d) Using phase in the transfer function. (e) Corresponding observed and simulated spectra.

Coherency

We have developed a coherency relationship between station pairs. At each station, the vector sum of the two horizontal components are calculated. These combined horizontal components are used to derive coherency relationships. Time series are shown in Figure 20 for several sites and for the same event. The coherency plots arc only for the S-wave portion of the seismograms because the S-wave contains a major proportion of seismic wave energy and it is significant for lateral force considerations in design engineering. Figure 21 shows coherency as a function of frequency for the station pairs indicated.

For the purpose of this paper, coherency values of 0.5 and above are considered as "coherent" and those below 0.5 “incoherent", this is discussed in detail in Hutchings and Wu (1990). In this study, with relatively smaller earthquakes, the lower frequency cutoff is 2 Hz. Generally, arrivals remain coherent up to about 15 Hz for the station spacing considered. Larger earthquakes will extend these calculations to lower frequencies, and thee are expected to be even more coherent.

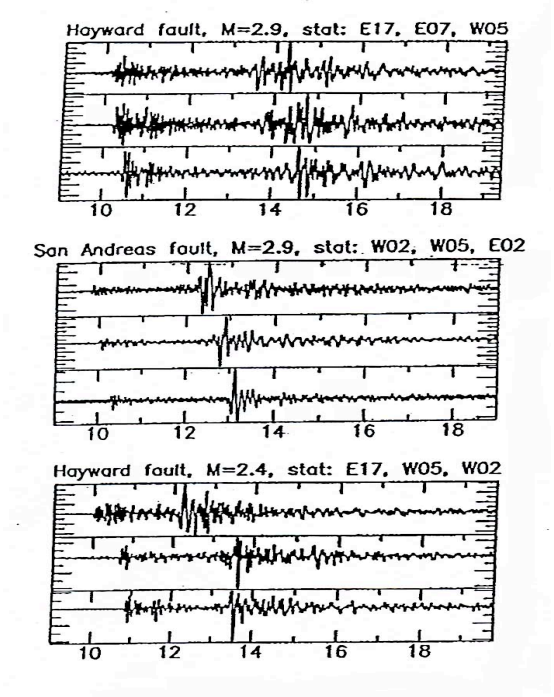

Figure 20: combined horizontal components for three events.

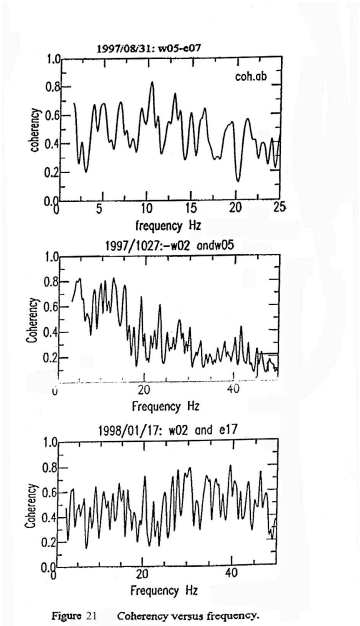

Figure 21:

Dumbarton Bridge Microearthquake Analysis

Site to site variability

Figure 23 shows recordings of acceleration at each of the deep borehole sensors along the Dumbarton Bridge (north component only) from a M=1.9 earthquake located 19 km to the west, on the San Andreas Fault. Since the lithology at the boreholes is similar, we might expect the waveforms to be similar at each borehole from the same earthquake. However, waveforms change significantly at the three deep borehole sites. There are significant amplitude differences between the recordings, which are not consistent with propagation attenuation effects; and secondary arrivals are present at Pier 27 (center span) that are not present at the two end sites, which is typical of recordings interior to a basin. These same differences will occur in strong ground motion from future earthquakes, and result in phasing and amplitude variations across the bridge.

Figure 24 shows accelerograms from the top and bottom sensor pairs, respectively, for a M=6.5 earthquake located 490 km distant, near the Mendocino triple junction, and Figure 25 shows the spectra of the east component from the three sensors located at the top middle and bottom, respectively. Notice that there is a spectral amplitude difference of about a factor of 10-20 between 0.4 and 3.0 Hz, and about a factor of 1.0 to 5.0 at higher frequencies. The signal is above noise from about 0.4 to 25 Hz. Notice that spectral values (site response) do not converge to a common long period value. This presumably occurs at lower frequencies than plotted. Figure 26 shows accelerograms from an M=4.9 earthquake located 45 km distant, on the Calaveras fault. Accelerograms show from the top to the bottom of the borehole at Pier 1 and from the top of the pile cap at Pier 27. The amplifications are obvious.

Site Response Functions at the Dumbarton Bridge

The assumption utilized in this work is that the initial waves generated from point shear sources are approximated by a whole space solution and resulting complexity of seismograms results from near recordings site geologic complexities. Therefore, in this study, Green's functions for frequencies 0.5 to. 25.0 Hz are approximated by point shear source solutions convolved with site response functions. Site response functions are utilized by the EMPSYN by selecting EGF's from anywhere in the region and deconvolving out the source and propagation path effects. A simple point shear sources double couple solution for a homogeneous whole space, with Q, is used to deconvolve out the propagation and source effects from the seismograms. These are then convolved back with the solution for point shear source from the appropriate locations on the fault. Table 8 lists the events used to obtain site response functions at the three sites, and Figure 27 identifies their locations.

Figure 23 Recordings of acceleration at each of the deep bore sensors along the Dumbarton Bridge (north component only) from a M= 1.9 earthquake located 19 km to the west, on the San Andreas fault.

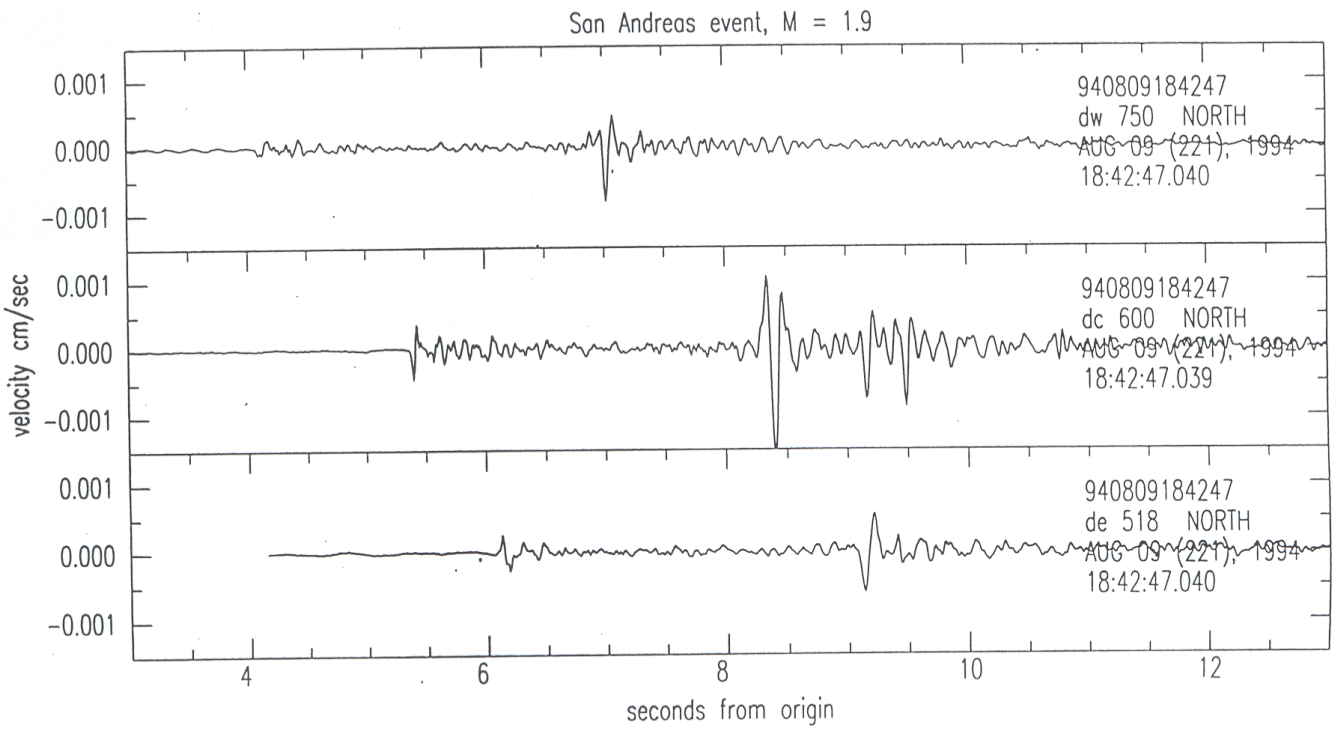

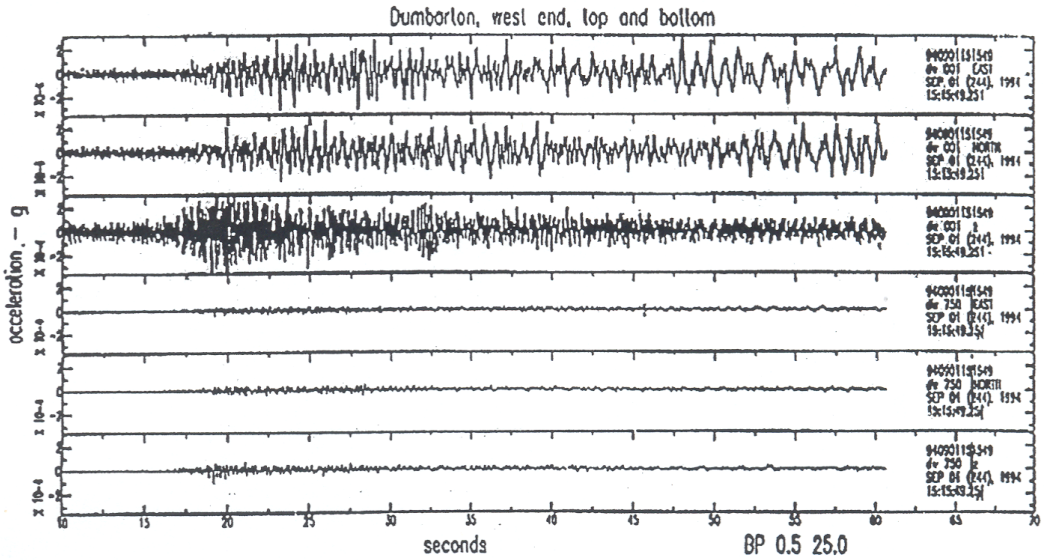

Figure 24: Accelerograms from the top and bottom sensor pairs for a M=6.5 located 490 km distant, near the Mendocino triple junction.

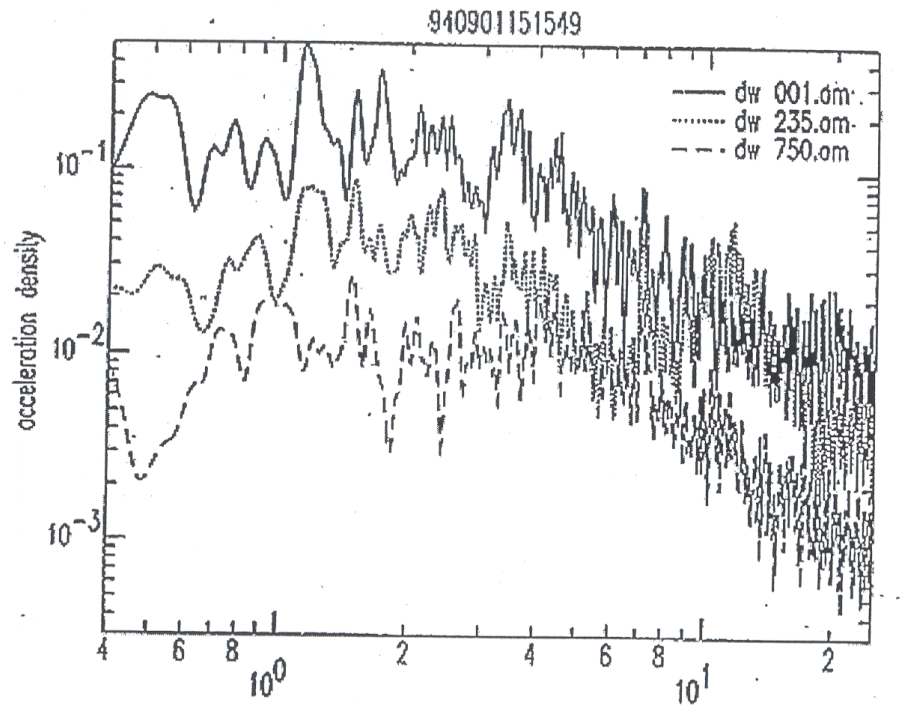

Figure 25 Spectra analysis of the eastern component from the top, middle, and bottom of the borehole on the Dumbarton Bridge.

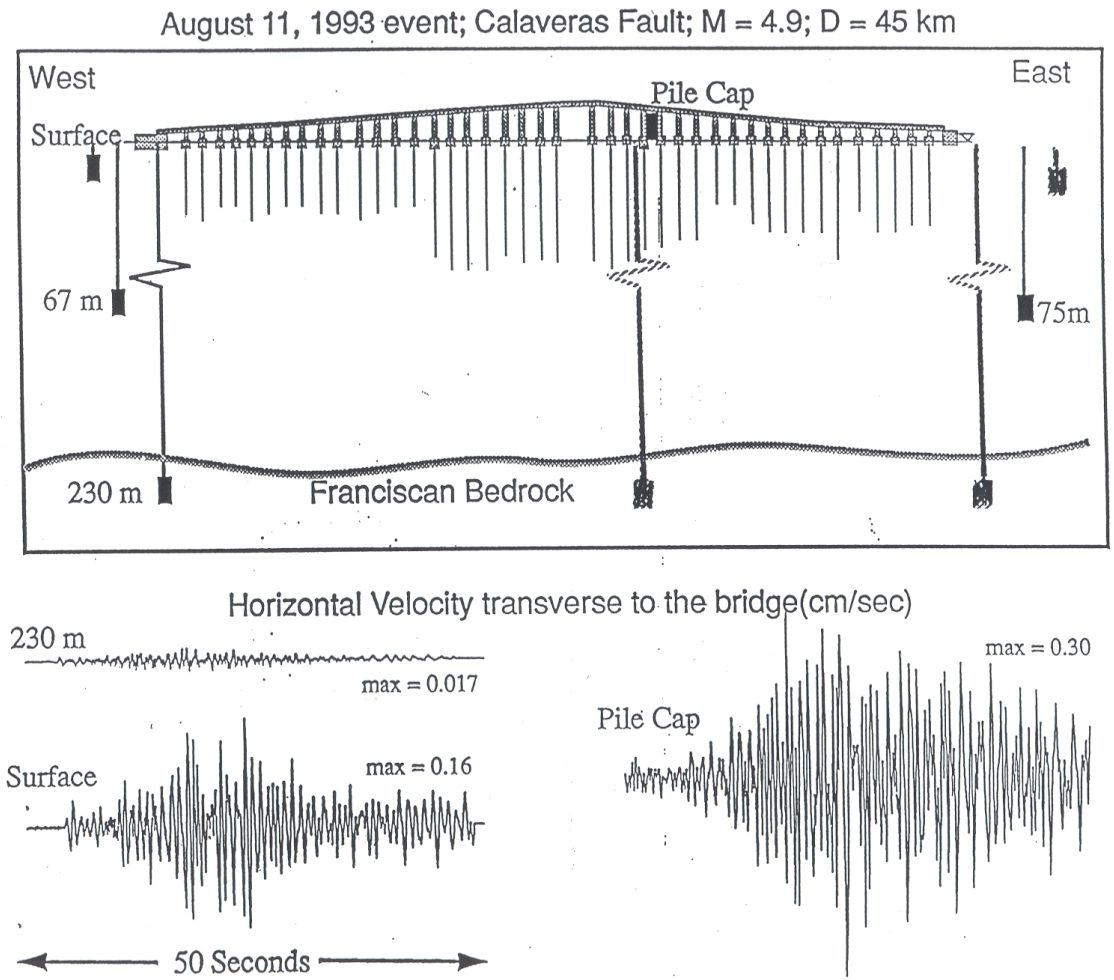

Figure 26. Recordings of acceleration from the top to the bottom of the borehole at pier 1 and from the top of the pile cap at pier 27 along the Dumbarton Bridge.

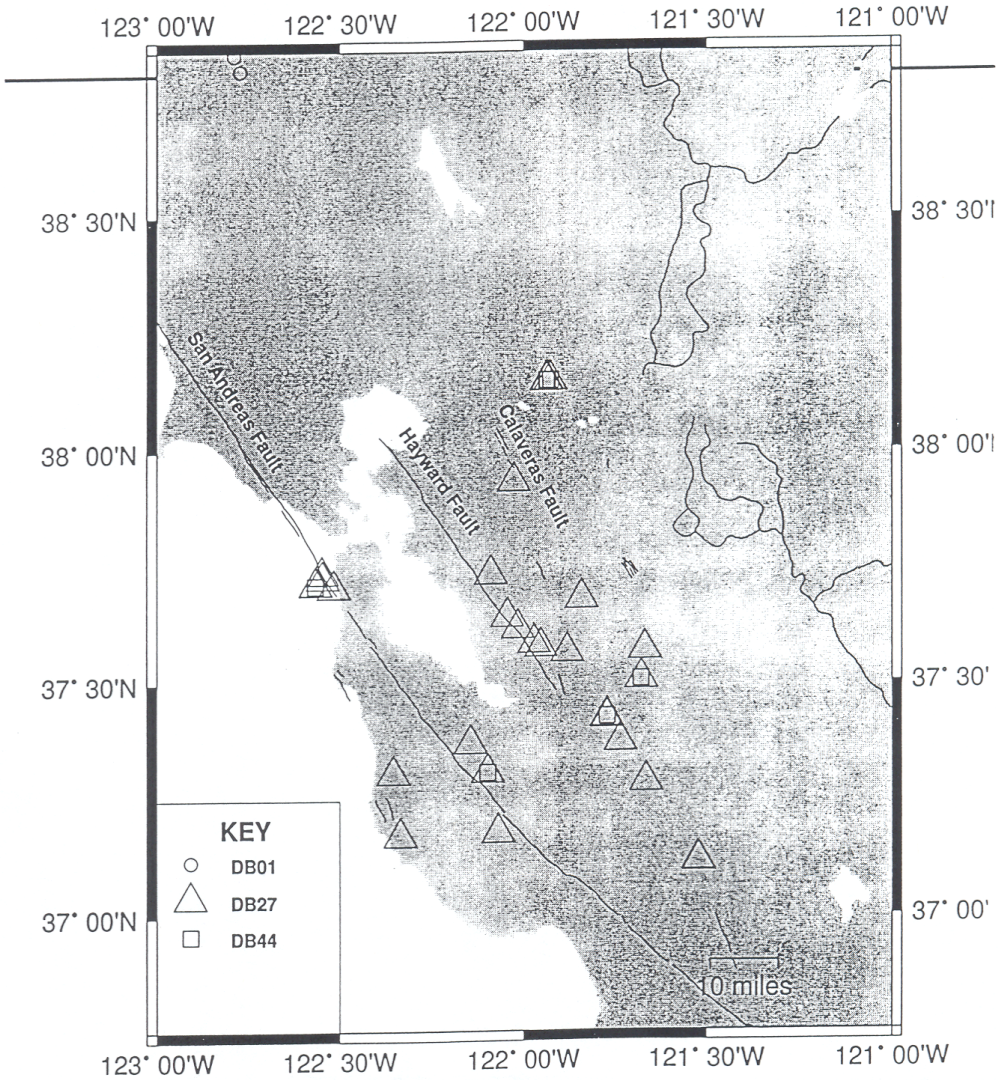

Figure 27 Plot of earthquakes recorded by the Dumbarton Bridge recorders.

Table 8: Events for Site Response Study

Earthquake	Time	Latitude	Longitude	Depth	Mag	Fault
1998/10/20	12:46:18.87	37.878	-122.246	10.0	2.1	Hayward
1998/10/22	01:28:36.34	38.525	-122.303	8.3	3.0	Unknown
1998/11/03	06:02:16.32	37.876	-122.243	9.5	2.4	Hayward
1998/12/04	12:16:07.76	37.920	-122.290	6.8	4.1	Hayward
1999/01/26	06:02:42.51	37.9143	-122.2883	4.71	2.0	Hayward
1999/02/04	00:19:36.92	37.1602	-121.5537	6.10	3.9	Hayward
1999/04/04	06:00	37.	-122.			
1999/06/23	23:48:10.36	37.8735	-122.2435	9.84	2.0	Hayward
1999/08/12	08:16:37.44	37.8663	-122.2453	6.54	2.5	Hayward
1999/08/18	01:06:18.93	37.9068	-122.6868	6.67	5.0	San Andreas

Strong Ground Motion Synthesis for the Bay Bridge

The purpose of this project is to provide a computation of linear strong ground motion along the San Francisco/Oakland Bay Bridge (western and eastern spans). We synthesized ground motion from a possible M=7.25 Hayward fault earthquake. We synthesize the entire wavetrain and for three components in acceleration, velocity and displacement, and for frequencies from DC to 25.0 Hz. These computations are for equivalent rock surface sites (up-going energy) and can be used directly as input into non-linear finite element modeling of the bridge for sites with no sedimentary cover, or as input into soils models of the Bay sediments.

The proximity of the bridges to Hayward fault requires broadband ground motion calculations and at several points along the bridge to account for the effects of finite rupture and directivity, fling, wave passage, and high frequency incoherency. This is achieved in this study by (1) providing a numerical solution in finite rupture along the faults; (2) using a three-dimensional finite element method (Larsen, 1994) for synthesis of ground motion frequencies below 0.7 Hz; (3) using a empirical Green's functions for synthesis of ground motion for frequencies from 0.7 to 25.0 Hz; (4) computing the ground motion at four locations along each of the western and eastern spans of the structure. Empirical Green's functions are obtained from actual recordings at sites along the structure and explicitly account for high frequency incoherency due to variations in the geology. The high and low frequency solutions are merged into broadband ground motions from 0.0 to 25.0 Hz.

Generally, dimensions of structures less than one-quarter wavelength of passing seismic arrivals will respond coherently to the wave passage. The 5 Km long western Bay Bridge, for example, will have differential motion at the ends of the bridge from seismic wavelengths less than 20 Km that are axially incident. The collapse of the eastern Bay Bridge section during the Loma Prieta earthquake, for example, has been attributed to 30 cm differential motion of two ends of the Bridge. Similarly, 25 m bridge supports will have differential motion from wavelengths less than 100 m (about 25 Hz for P-waves); seismic energy at frequencies greater than 25 Hz is generally insignificant to earthquake hazard analysis. Further, the rupture process will affect a structure located near a large fault. First, seismic arrivals from all portions of the fault will impact structures, and the radiating source can be simultaneously from locations that are several kilometers and even tens of kilometers apart. The superposition of arrivals from extended source locations and from body-waves and surface-waves will result in an extremely complicated wave field. Also, directivity effects can result in accumulation of energy at long periods at certain locations. In addition, elongated structures positioned transverse to a large fault rupture will be affected by the propagation of strain due to the tectonic shift (D.C.) to the final plate position after the earthquake. This is achieved over a period of time comparable to the duration of the earthquake and will result in a ramp in displacement to achieve the final D.C. offset. This is phased in time and amplitude across the structure. To model all these effects we develop solutions of extended source earthquake rupture and apply physically based rupture parameters. We use empirical Green's functions (EGF's) to model high frequency propagation effects and synthetic Green's functions to model low frequency effects.

Modeling Approach

We model large earthquakes by solving the representation relation (Aki and Richards, 1980) for a finite earthquake rupture. In this solution, we discretize a potential fault rupture surface and appropriately sum point source Green's functions that are convolved with slip functions. This is the Green's function summation approach (Heaton, 1982). We have developed an exact solution to the representation relation that utilizes either empirical or synthetic Green's functions (Hutchings and Wu, 1990, Jarpe and Kasameyer, 1996). Empirical Green's functions are defined here as recordings of effectively impulsive point source events. Synthetic Green's functions are computed for the same point source events with the finite difference method (Larsen, 1994). This method includes all arrivals, including near-field terms. The latter results in permanent offsets. The calculation is for frequencies 0.0 to 0.5 Hz. The synthetic and empirical Green's functions solutions are matched filtered and added together to give a broadband solution of 0.0 to 25.0 Hz (borehole) or 15.0 Hz (surface).

This modeling approach only requires that the number of times small earthquakes are used in the synthesis be such that the sum of their moments add up to the moment of the large earthquake. Therefore, low frequency amplitudes match those of observed seismograms. The high frequency is matched simply by using appropriate rupture parameters (Hutchings, 1994). This modeling approach has been described in a series of publications: Hutchings and Wu, 1990; Hutchings, 1991; Hutchings, 1994; Foxall et. al., 1994; Jarpe and Kasameyer, 1996; Hutchings and Jarpe, 1996; and McCallen and Hutchings, 1996. The computer code EMPSYN is used to generate synthetics and is described in Hutchings (1988). Moments for the empirical Green's function source event are calculated from a regional recording network.

We model the rupture process as a continuous rupture over the fault surface with variable slip amplitudes that can include multiple areas of high slip and variable stress drop. We attempt to simulate rupture slip amplitudes as observed in geologic studies and derived from inversion studies. The rupture initiates at the hypocenter and propagates racially at a percentage of the shear wave velocity. A Kostrov slip model is used, as described below. Fault rupture parameters defined for a rupture scenario includes fault: strike, dip, slip vector, rupture area, rupture and healing velocity (rise times), roughness, hypocenter, and number and location of large asperities. Moment is held fixed. Since we do not know in advance which rupture parameters will occur, they are varied to provide 100 rupture scenarios. Parameters were varied about a central (preferred value) with a triangular distribution and selected by a Monte Carlo technique.

Log-normal average and one standard deviation values of peak acceleration and absolute acceleration response spectra (AARS) were derived from the suite of 100 scenarios and used to slesuite of synthesized strong ground motion. The scenarios were developed by randomly varying rupture parameters within a range of physical limits obtained from the work of others. The time histories used for input into the soils or bridge models are those whose absolute acceleration response spectra most closely match the median (log-normal mean) and the +1 standard deviation values. By having a suite of rupture scenarios of hazardous earthquakes for a fixed magnitude and identifying the hazard to the site from the one standard deviation value of engineering parameters, we have introduced a probabilistic component to the deterministic hazard calculation.

EMPSYN

EMPSYN numerically computes the discretized representation relation, and it utilizes the from (Hutchings and Wu, 1990 and Hutchings, 1991):

$$u_n(X,t) = \sum_{i=1}^{N} \frac{\mu_i A_i S(t_i')_i}{M_{0i}^e} \otimes e_n\left(X, t_i' - \frac{\overline{\chi_i}}{V}\right)_i \tag{1}$$

This is an exact solution for the representation relation under certain conditions, and it is our intent to keep as close to the mathematically exact solution as possible, with approximations adding to the uncertainty of the solution. The fault rupture surface is divided in N small areas A_i such that $\sum A_i$ equals the total rupture area. $e_n(X,t_i')_i$ is the empirical Green's function for the ith element obtained from recordings of small earthquakes. u_n has the same units as e_n. At this point the focal mechanism solution of the large and small event are assumed to be the same, and the small event is assumed to have a step dislocation source time function (discussed further below). We can use any elemental area size as long as it is small enough to satisfy the point source criteria, and we do not need a scaling relation between small and large earthquakes. Also, we do not need to know the stress drop of the little earthquake (Hutchings, 1994). e_n provides the elastodynamic Green's function ($G_{np,q}$) in the conventional representation relation (see Hutchings and Wu, 1990). $G_{np,q}$ is isolated from the empirical Green's function by deconvolving out the source function and normalizing by the scalar seismic moment of the small event M_{0i}^e. The deconvolution with the source function of the small earthquake is included in the analytical solution for the slip function of the larger event. Therefore, $S(t_i')_i$ is the desired slip function analytically deconvolved with the step function, and t_i' is time at the element, which is equal to 0.0 at the arrival time of the rupture front. Empirical Green's functions are interpolated to have a source at each element and are adjusted to have origin time when t_i' is 0.0. $\overline{\chi_i}$ is the radial distance from the hypocenter to the elemental source, and V is the rupture velocity. The main advantage of the empirical Green's function approach is that if e_n is managed properly, then it provides the exact elastodynamic Green's function for the real earth.

Green's Functions

The basic premise in synthesizing with empirical and synthetic Green's function is that each offers the best accuracy over particular frequency bands. The empirical Green's functions have a better accuracy over high frequencies where geologic in homogeneities are not well modeled, and the synthetic solution have better accuracy over lower frequencies where empirical Green's functions do not have sufficient energy. The overlap is in the rant from 0.5 to 1.0 Hz. In this range, the geology can be modeled with some accuracy and the empirical Green's function has sufficient energy to be recorded.

Empirical Green's Functions

Empirical Green's functions include the actual effects of velocity structure, attenuation, and geometrical spreading. It is not possible to record empirical Green's functions from all locations along a fault of interest and with the same focal mechanism solution, so source locations of empirical Green's functions have been interpolated to fill in the fault. The spatial dependence of empirical Green's functions was studied by Hutchings and Wu (1990), and they found that the variability in ground motion due to differences in source location and/or focal mechanism solutions are much less than those due to the site response. Hutchings (1991), Hutchings (1994), and Jarpe and Kasameyer (1995) found that interpolation for different source locations along a fault. Works quite well, and that source events do not have to fall directly along the fault of interest, but can be located near the fault. In synthesis, we have the option of correcting for different focal mechanism solutions, but Hutchings and Wu (1990) and Jarpe and Kasameyer (1995) found that, for high frequencies, corrections to empirical Green's functions do not improve the synthesis. Interpolation is performed by correcting for attenuation, geometric spreading by //distance (1/R), and P- and S-wave arrival times due to differences in source distance. We include the radiation pattern effect for low frequencies when we use synthetic Green's functions.

All available recordings of small earthquakes along the Hayward fault during the time of this study were used (Figure 31) as empirical Green's functions and interpolated to provide the high frequency Green's function for each element. The use of small earthquakes for empirical Green's functions as applied in this study is discussed extensively in Hutchings and Wu (1990) and Hutchings (1991). Using several empirical Green's functions averages out random errors and provides wave propagation information from different travel paths (Wossen et al., 2001). Events were used in two frequency bands. Events with magnitude $1.5 < M < 2.5$ were used as impulse point sources for frequencies $2.0 < f < 25.0$ Hz, and events with magnitude $2.5 < Hz < 4.5$ were used as point sources for frequencies $0.7 < f < 2.0$ Hz. Detailed instrument and event source information can be found in Hutchings (1999). Borehole locations are generally 100 ft north of the existing towers identified in the, so that empirical Green's functions are not recorded exactly at each pier.

Synthetic Green's Functions

We model wave propagation for frequencies from DC to 0.7 Hz using the finite difference wave propagation program E3-D (Larsen, 1994; Larsen and Schultz, 1995). This solution includes full 3-D elastic modeling, extends to zero frequency and the full wavefield of seismic energy. The underlying methodology of the program is based on the elastodynamic formulation of the full wave equation on a staggered grid (Madariaga, 1976; Virieux, 1986; Levander, 1988). In this formulation, the velocities and the stress tensor components are solved by an explicit finite-difference scheme (indices correspond to the x, y, and z Cartesian coordinates). Each variable is staggered by 1/2 grid point spacing from the other variables. A staggered grid implementation is beneficial because of the spatial differencing stencils are centered around each variable, which minimizes the computational burden for a given level of accuracy. A 4th-order

spatial stencil is applied to each differential term on the equations of motion. We coupled a complex geologic model for northern California (Stidham, et al., 1999) to the finite difference code. The geologic model represents the local near-surface geology averaged over a few kilometers. Deeper and more distant geology is represented in less detail. The model was coupled to the computer code in a volume 175 x 100 x 40 km in size.

The finite-difference code is coupled with a source model to replicate source models as described above, but does not use finite-difference point source Green's functions. However, the fully coupled source and wave propagation code is identical to using individual Green's functions with a kinematic rupture. The Gaussian source represents the moment-rate time history, which is equivalent to the slip velocity. The point source equivalent Green's functions have a Gaussian moment rate function with standard deviation of 1.0 sec. The 250 m spacing of the finite-difference grid can numerically accurately propagate energy only up to about 1.0 Hz.

Near-Source Strong Ground Motion

Locations very near fault rupture are dramatically affected by fault rupture velocity, fault slip rate, directivity, radiation pattern, and superposition of seismic waves. In addition, these effects are significantly different for ground displacements, velocities, and accelerations, as each of these has dominant energy at different frequency bands. *Two* terms describe aspects of ground motion near 'a fault. *Near source* refers to distances within about 2 fault lengths of the earthquake. In this distance range, significant finite rupture effects are observed in strong ground motion and simple point source models of earthquakes are not sufficient. We account for these effects by modeling the complex evolution of the rupture. For example, the radiation pattern of shear waves works to enhance amplitudes of strong ground motion near a fault as the maximum amplitudes occur along the fault plane. Directivity due to fault rupture propagation also enhances or diminishes long period amplitudes. All these effects will be demonstrated below. *Near-field terms* refer to wave arrivals that are recorded very near an earthquake and attenuate away at $1/R^2$ and $1/R^4$, and are a result of the effects of fault offsets. *Near-field* terms dominate within a fraction of a wavelength from the source, independent of rupture length. Near-field signals are typically long period in nature, and as discussed above.

Near-source effects produce significant aspects of seismograms. One means to examine this effect is to study synthetic calculations of strong ground motion. Figures 28 and 29 show synthetic ground motions for the fault parallel (N145E) and fault normal (N235E) components, respectively, of ground velocity at locations on the fault (Figure 28, at BKS) and 4.3 Km distant from the fault (figure 29, at STK). The shear wave radiation pattern has a maximum for locations along the fault and a nodal solution at points normal to the dislocation. Figure 30 shows the rupture model used and discussed below, and the locations of stations BKS and STK. Only solutions with synthetic Green's functions are shown, and here we use Green's functions solutions from the reflectivity code of Kennett (1983) and for frequencies 0.1 to 5.0 Hz. For purposes of strong ground motion prediction, only frequencies less than 0.5 Hz ere considered reliable, but for analysis of near-field effects we examine frequencies less than 5.0 Hz. The interpretation of Figures 28 and 29 is that the first large amplitude arrivals are made up of shear waves. These are followed by surface waves, which are primarily Love waves on the N235E component and Rayleigh waves on the N145E component. They are purely Love and Rayleigh waves for the 0.0 Km distant solution.

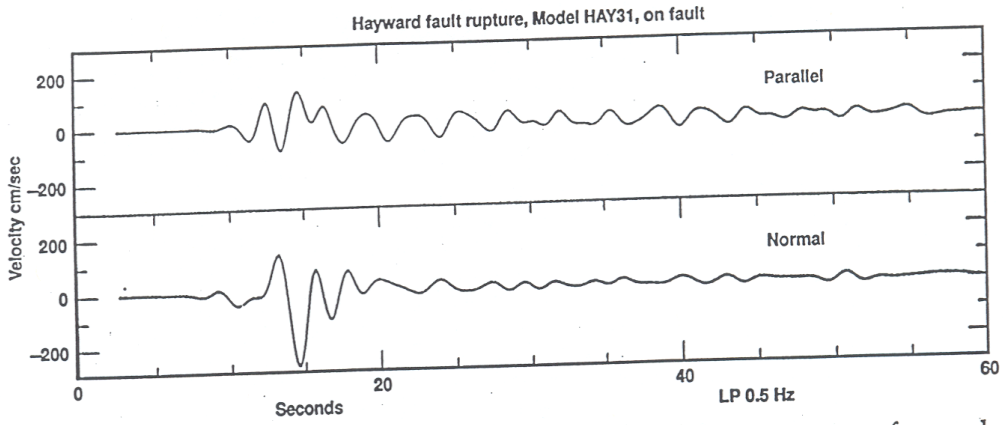

Figures 28 Synthetic ground motion for the fault parallel (N145E) components of ground velocity at locations on the fault.

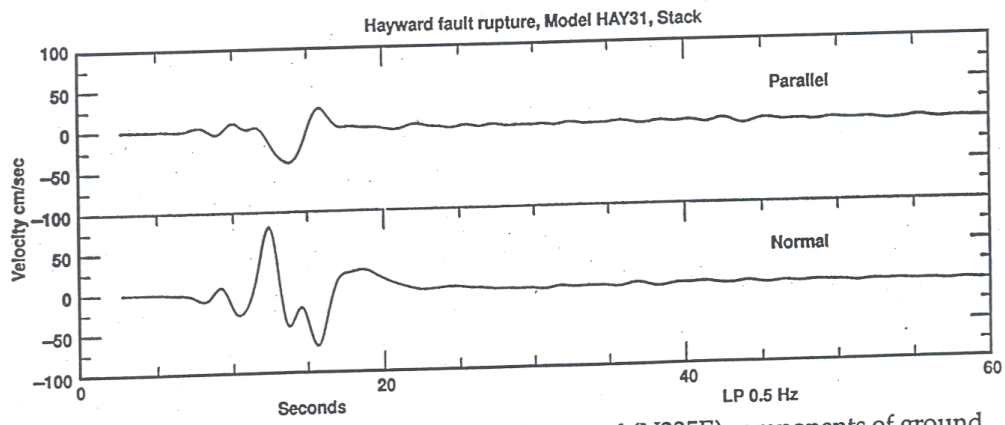

Figures 29 Synthetic ground motion for the fault-normal (N235E) components of ground velocity at locations at the Stack (4.3 km distant).

The amplitude of the first arriving shear wave (first arriving large pulse at about 10 sec) diminishes by a factor of 3 from locations on the fault to the location of the Stack. The shear wave is presumably enhanced both by the directivity effect and the radiation pattern maximum along the fault. Rayleigh waves immediately follow the shear waves, and their amplitudes also diminish significantly away from the fault. Geometrical spreading is not considered a strong factor in the near-field ground motion, as large motion arrive from portions of the fault some distance up and down the fault strike, and radial distances are not greatly different for most of the fault surface. However, portions directly in-line with the sites are significantly affected by the geometrical spreading, and this would contribute a factor of 4.3 km at the Stack.

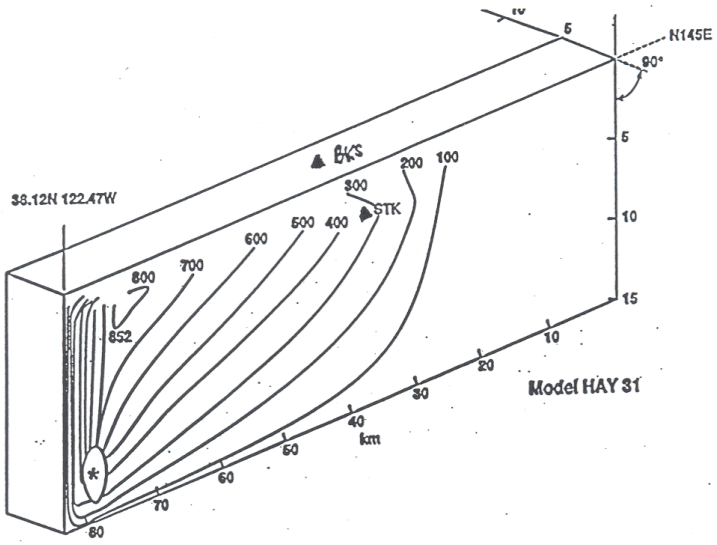

Figure 30. The slip distribution and hypocenter of scenario HAY31. There is one small asperity at the hypocenter for this model.

Hayward Fault Rupture

The Hayward fault extends from Mission San Jose to northern San Pablo Bay (Figure 31). The working Group on California Earthquake Probabilities (1988 and 1990) have identified two segments of the Hayward that may rupture separately: the northern and southern segments. Both are considered capable of a magnitude 7.0 earthquake. In addition, the working group has posed the possibility of both segments rupturing

during the same earthquake. The coordinate ends for the segments as defined by the working group (1990) plot the Hayward fault 4 km east of the mapped trace of the Hayward fault. Therefore, the latitudes provided by the working group are used to segment the fault, but the longitude is obtained from mapped surface traces: 37.500°N 121.935°W, 37.733°N 122.137°W for the southern segment, and extending to 38.117°N 122.472°W for the northern segment. The extension of the northern segment through San Pablo Bay has been supported by recent high resolution seismic profiles and seismicity (Lienkaemper et al., 1989). The Working Group did not consider the Hayward fault south of Mission San Jose capable of large earthquakes. Surface expression of the fault is weak or nonexistent and has very little microearthquake activity. The segments are shown in Figure 31. These segments are 50 and 32 km long, respectively. We have modeled the northern segment earthquake as $M = 7.1$ ($M_0 = 5.0 \times 10^{26}$ dyne-cm) with 2.0-m average slip (strain release) and the southern segment as $M = 7.0$ ($M_0 = 3.5 \times 10^{26}$) to keep average slip equal for the two segments. The combined Hayward fault earthquake is modeled a $M = 7.25$ event ($M_0 = 8.5 \times 10^{26}$) with 2.1-m average slip. We are using the characteristic earthquake model (Schwartz and Coppersmith, 1984; and Sieh, 1984) to project the magnitude of the combined rupture as a linear sum of the segments.

Two earthquakes occurred along the Hayward fault in the past century (1836 and 1868), and both have been estimated by the working Group to have magnitude about 7.0. Slip rate estimates of about 9 mm/yr result in 1.4 m of accumulated strain since 1836 for the northern segment. This number is within the range that is possible within the near future (Wells and Coppersmith, 1994).

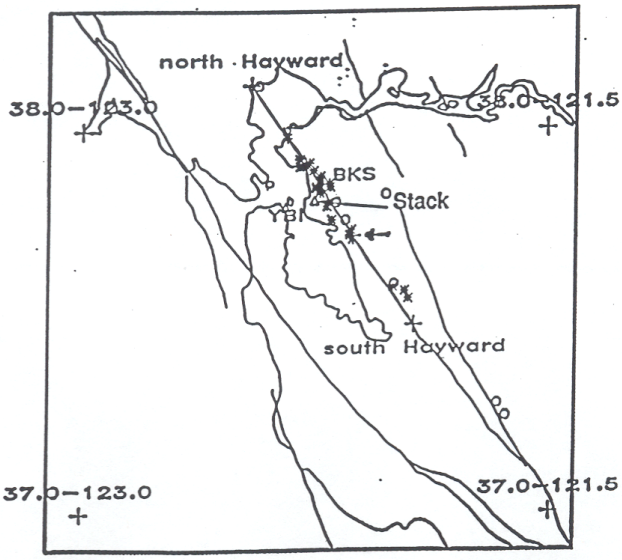

Figure 31. Faults in the San Francisco Bay area. For this study, the area of the Hayward fault between the two crosses is assumed to rupture. Asterisks indicate source locations of small earthquakes recorded at BKS, and the octagons indicate events recorded at YBI.

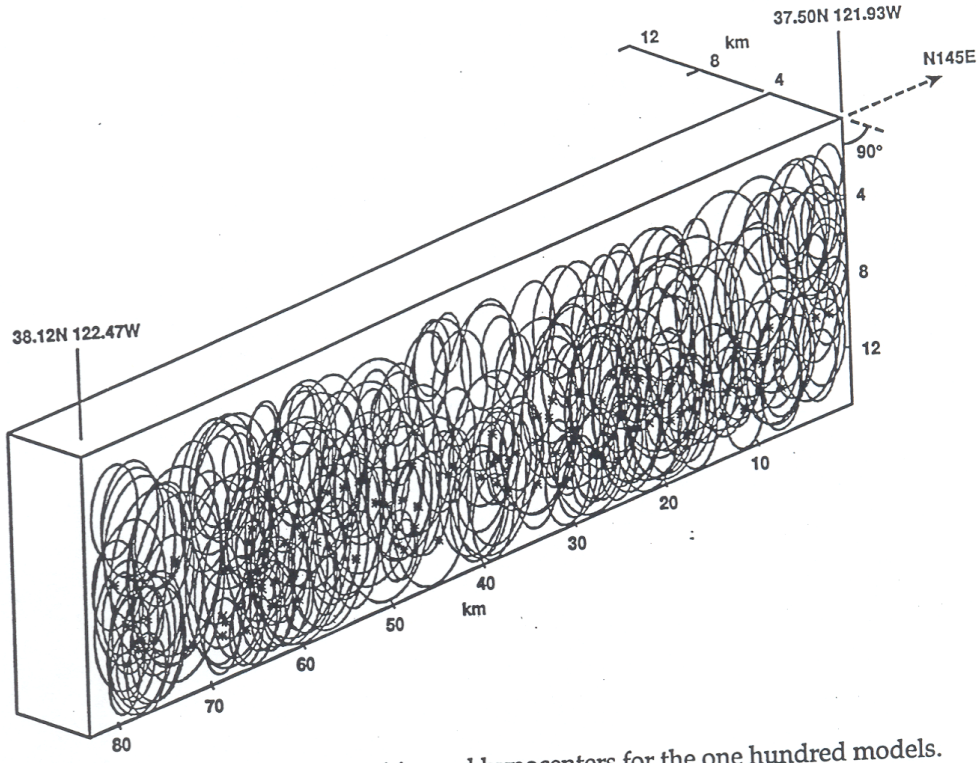

Figure 3a The location of all asperities and hypocenters for the one hundred models.

Strong Ground Motion Prediction

We use a physically based kinematic source models to generate rupture scenarios that span the variability of potential ground motion in a predictive situation. We calculated the hazard at a location midway between the Hayward fault and the SFO bridge to identify the mean and one standard deviation hazard for Hayward fault rupture. Physically based here refers to models that are consistent with the elastodynamic equations of seismology and fracture energy, and they are consistent with a physical understanding of how earthquakes rupture, laboratory experiments, numerical modeling, and field observations of earthquake processes. Physically based source models allow one to vary input parameters and generate combinations that have not yet occurred in nature. Bounds on input parameters are based on physical understanding and naturally bound the synthesized ground motions. The basic premises of the methodology are: 1) accurate synthesis of recorded ground motions for a particular fault rupture scenario, sufficient for engineering purposes, is possible, 2) a general description of the rupture is sufficient for synthesizing realistic ground motions; 3) the rupture characteristics of a fault can be constrained in advance by interpreting physical properties such as geologic structure, seismicity, and tectonics of the region, 4) the range of possible fault-rupture scenarios is narrow enough to functionally constrain the range of strong ground motion predictions, and 5) a discrete set of rupture scenarios is sufficient, for engineering purposes, to span the infinite combinations possible from a given range of rupture parameters. An important corollary is that if a scenario earthquake matches observed seismograms, then the rupture parameters of that scenario are close to what actually happened. This methodology has been validated by several studies (Hutchings 1991; Hutchings, 1994; Hutchings and Wu, 1990; Hutchings et al., 1997; Hutchings et al., 1998; and Jarpe et al., 1996). Parameters used for rupture models are:

ASPERITIES are included to add variation to the slip distribution. The slip distribution for asperities is added to the main rupture. Asperities have a circular shape and have a diameter randomly chosen to be between 0.2 and 0.8 times the fault width. The number of asperities is randomly chosen to be between 0 and 6. Six was arbitrarily chosen as the maximum number from the fault length divided by its width. Asperities are not allowed to overlap. The asperity numbers listed in Table 1 are specific to the model; asperities are randomly selected for each scenario. Stress drop in asperity portions of the rupture are higher than other portions of the rupture area. Figure 2 shows the location of all asperities for the one hundred models.

ROUGHNESS (%) is the percentage of the rupture surface for which we applied randomness to the rise time so that we could simulate roughness. The percentage is randomly selected to be either 0, 10, 20, 33, or 50%. This percentage of elements has rise time randomly shortened to between 0.1 and 0.9 times the original value. The difference in rise time is applied as a delay to rupture initiation so that the rupture reaches the full value at the original time. Areas of roughness have corresponding high stress drop.

MOMENT is constrained to be 8.5×10^{26} dyne-cm for the total rupture, including asperities. However, the moment of asperities is randomly selected. Their moment is constrained such that the maximum displacement is between 5 and 10 m.

HYPOCENTER is constrained to occur at least one kilometer from the fault ends, 2.0 km from the lower limit of the fault, and at depth >7.5 km. The limit at the ends is due to a physical model that has at least a small amount of bilateral rupture. The limit at the lower portion of the fault is because the material greater than 13-km depth is modeled as weakening in rigidity as the aseismic zone is approached, and the limit to >7.5 km is due to the observation that past earthquakes originate at depth (Sibson, 1982; Tse and Rice, 1986). Figure 5 shows the location of all hypocenters for the one hundred models.

RUPTURE VELOCITY (xVs) is the percentage of shear-wave velocity for the rupture velocity. This was allowed to vary from 0.75 to 1.0 times the shear wave velocity. This is the range from the Rayleigh to shear wave velocity.

HEALING VELOCITY (xVr) is the percentage of the rupture velocity for the healing velocity. Healing velocity controls the rise time. It is the shortest time for the rupture front to reach an edge and travel to a point at the healing velocity. If the healing velocity is greater than the rupture velocity, it will shortly overtake the rupture front, and thus, no rise time will develop. Clearly, the simple crack model for healing velocity is not sufficient, i.e., with healing at 0.6 to 1.0 times the P-wave velocity. Therefore, we randomly varied healing velocity to between 0.8 and 1.0 times the rupture velocity, which is between the Rayleigh wave velocity and

the shear wave velocity. In addition, the surface is not allowed to be a healing boundary for rupture since significant seismic pulses, which are necessary to shut down slip, are not generated from the surface (discussed below) (Das and Kostrov, 1989; and Schultz, 1990). Also, the time of propagation from hypocenter to an element utilized in the Kostrov slip function is limited to less than or equal to the shortest distance to a fault edge from the hypocenter divided by the rupture velocity. This is somewhat arbitrary, but limits the linear growth of displacement with rupture distance for very long ruptures. We equate this limiting value to a limit of "memory" of fault rupture and a departure from a pure crack solution for an extended rupture.

STRESS DROP is a dependent variable derived from the Kostrov slip function and allowed to vary due to two other effects modeled in rupture. First, asperities are allowed to have a different stress drop than surrounding portions of the fault rupture. Second, stress drop is constrained to diminish near the surface of the earth at the rate of $10 + 0.75x$ the confining pressure due to the lithostatic load (300 bars at 1.7-km depth). The minimum of this and the full rupture stress drop is used. Initially, the full rupture stress drop (without asperities) is assumed to be 300 bars, then the slip and rise times are computed over the fault surface (including asperities). If the moment is different than prescribed, the stress drop is adjusted to give the slip amplitudes necessary. The rise time is not adjusted.

RIGIDITY varies with the shear wave velocity over all depths except it diminishes at the same rate as the stress drop near the surface. The diminishing of stress drop and rigidity near the surface has two effects. First, reducing the rigidity results in very little moment contribution for rupture near the surface. Second, the commensurate diminishing of stress drop and rigidity result in significant displacements (although not significantly seismogenic) at the surface.

SLIP VECTOR is constrained to 180° for a right-lateral strike slip fault.

Figure 33 shows displacement contour plots of two of the one hundred scenarios; plots for two other scenarios are shown in figures 37 and 39. Figure 34 shows the absoluate acceleration response (AAR) for the one hundred scenarios. There is about a factor of 10 variation in values, and this is due to the wide variation in rupture scenarios. Figure 35 shows the distribution of the AAR values for 0.5 sec period. The histogram is not quite symmetrical, but is sufficiently close (by eye) that we assume that the calculated AAR are log normally distributed. Figure 36 show the shows the log-normal mean (arithmetic median), and plus and minus one standard deviation absolute acceleration response spectra values (16 and 84% confidence limits) from the one hundred scenarios. The confidence limits include the parametric and "random plus modeling" error estimates.

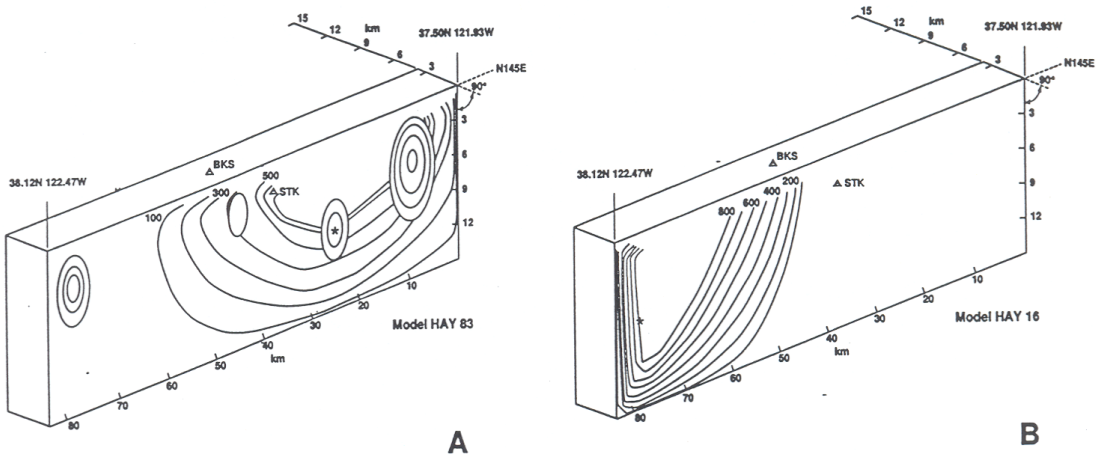

Figure 33 Displacement contour plots of various scenarios. The slip distribution varies considerably between the different scenarios.

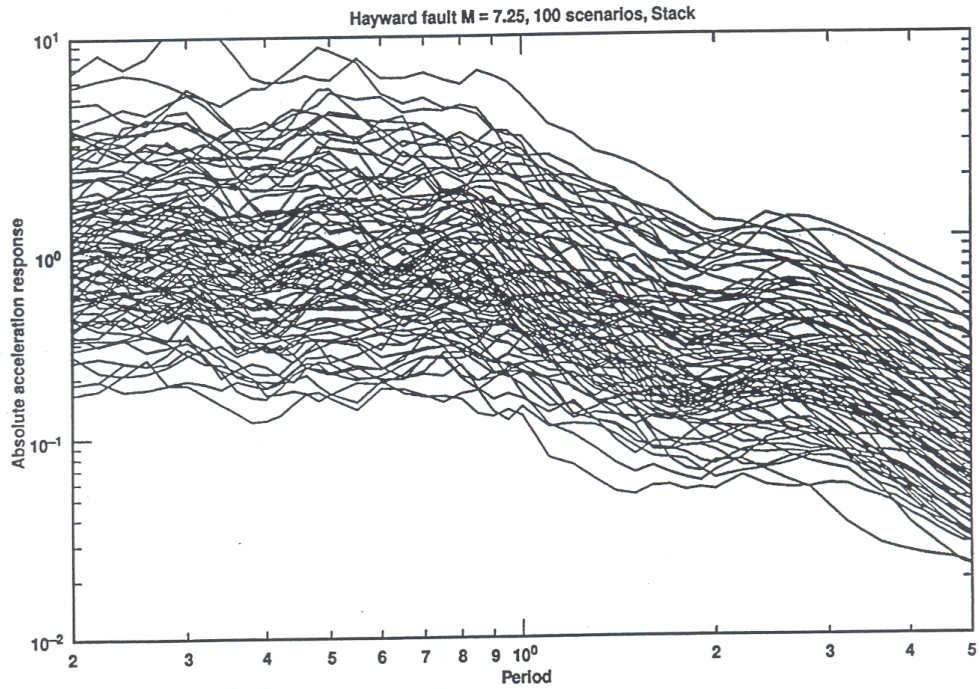

Figure 34 The absolute acceleration response spectra (average for two horizontals) computed from accelerograms from the one hundred scenarios.

The hazard is defined as either the median or 84% (+1 std) AAR at station STK. Model HAY31 generated time histories that most closely match the +1 std AAR and model HAY06 generated time histories that most closely match the log-normal mean (Figure 36). Figures 37 and 39 show the slip distribution and hypocenter of scenarios HAY31 and HAY06, respectively. There is one small asperity at the hypocenter for model HAY31. Figures 38 and 40 show their time histories at the station STK.

The median and one standard deviation time histories shown in Figures 38 and 40 have significant differences. These differences are due to the different rupture models. Model HAY31, which is the one standard deviation model, has high slip amplitude mostly in the northern portion of the fault and has a strong directivity effect as rupture propagates from the hypocenter towards the site. This contributes to the higher ground motion. The rupture velocity is also relatively high (0.94xVr, Table 1), which also added to higher amplitudes. Model 06, which is the median model has slip more evenly distributed throughout the fault and with lower amplitudes; the rupture has more a bilateral effect relative to the site; it has asperities, but they are located away from the site; and, the rupture velocity is lower (0.77xVr). The peak accelerations for the two models are 0.86 and 0.41 cm/sec^2, for models HAY31 and HAY06, respectively.

The ground velocity is higher from model HAY31 than from HAY06 (Figures 38 and 40, middle traces), with peak values of 158 and 81 cm/sec, respectively. This is due to the long period velocity pulse, which is larger for model HAY31 because of a stronger directivity effect. Also, the long period pulse is more pronounced for different components from the two models. For model HAY31, the pulse is more pronounced on the N235E and vertical components. While, for model HAY06, the pulse is more pronounced on only the N145W component. The directivity effects are different because of the different locations of the hypocenters.

The ground displacements are more similar for the two models HAY31 and HAY06 (Figures 38 and 40, bottom traces), with peak values of 106 and 86 cm, respectively. This is because this effect is more due to the final offset of rupture, which is more similar for locations near the site from the two models.

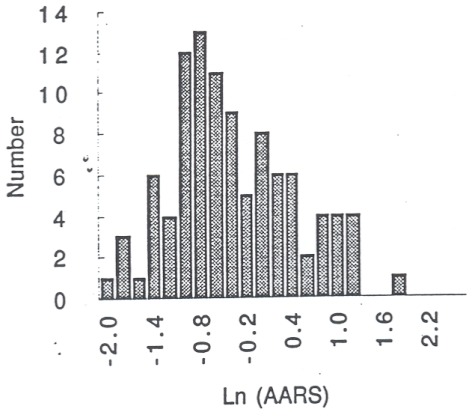

Figure 35 The distribution of the natural log of the calculated AARS value at a period of 0.5 sec.

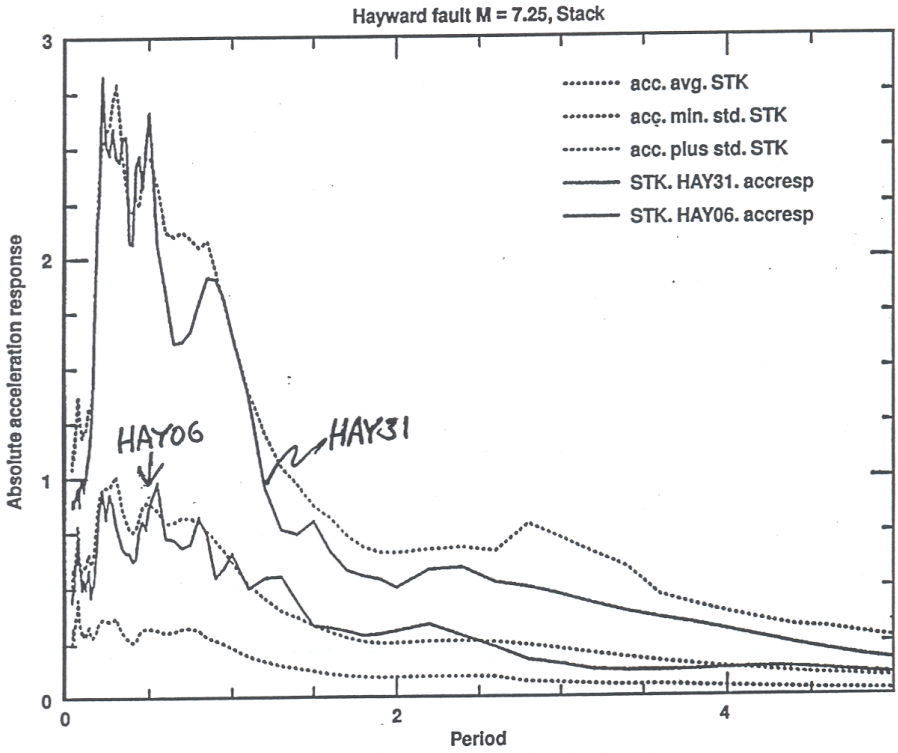

Figure 36 The median (log-normal mean), ±1 standard deviation response spectra from the 100 rupture scenarios. Model HAY31 generated time histories that most closely match the +1 standard deviation value.

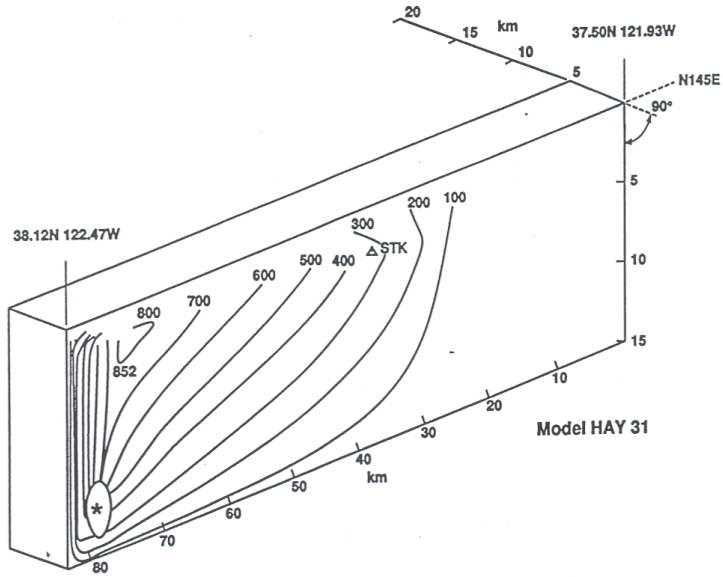

Figure 37 The slip distribution and hypocenter of scenario HAY31. There is one small asperity at the hypocenter for this model.

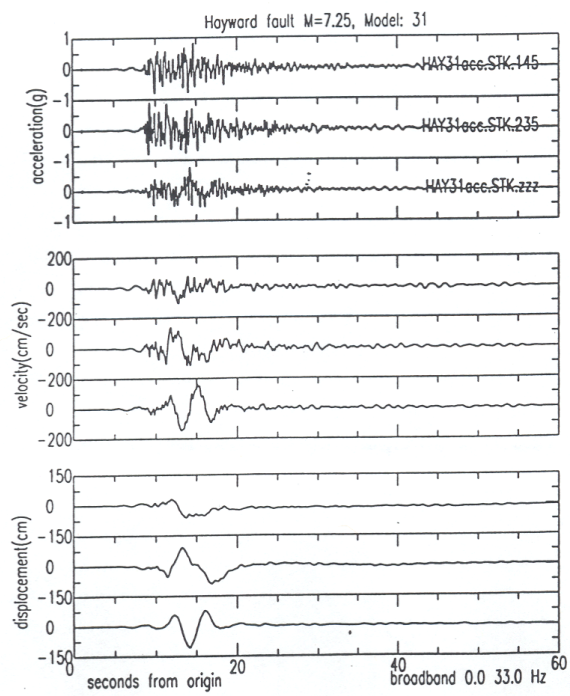

Figure 38 Time histories for frequencies 0.05 to 33.0 Hz; the top three are the three components of acceleration, the middle three are the same records integrated to displacement, and the bottom three are the displacement values.

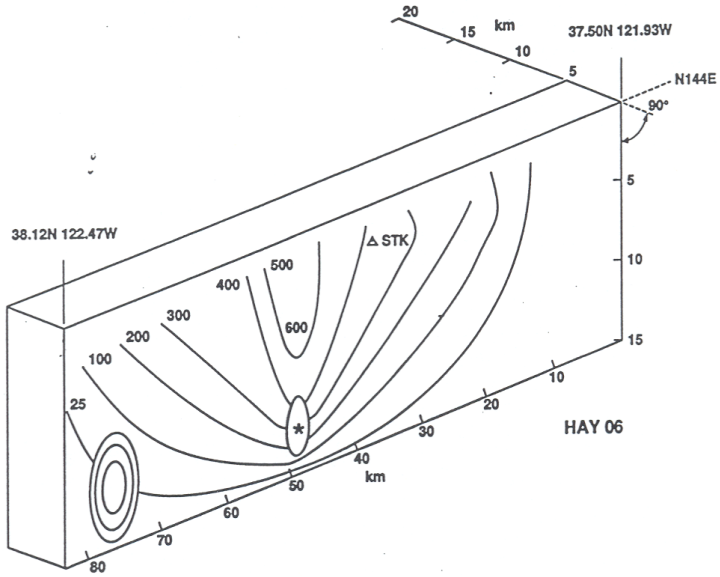

Figure 39 The displacement contours and hypocenter for model HAY06. There are two asperities for this model, one at the hypocenter and one between 70 and 80 km near the bottom of the fault.

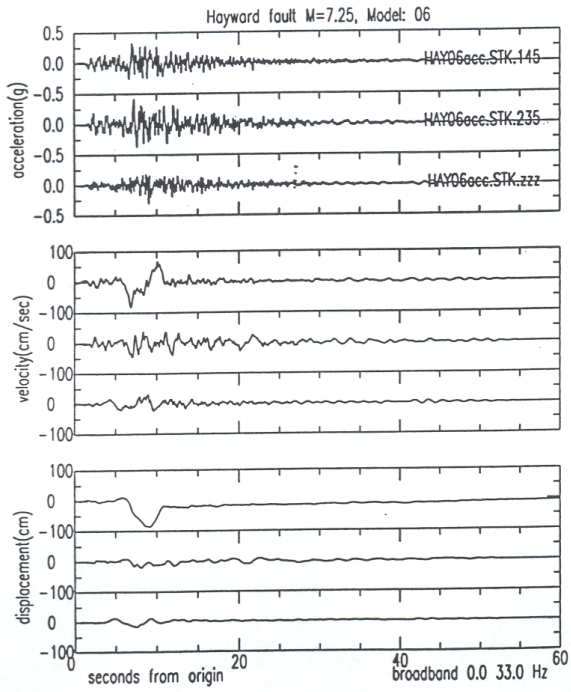

Figure 40 Time histories; the top three are the three components of acceleration, the middle three are the same records integrated to displacement, and the bottom three are the displacement values.

Ground Motion along the Bay Bridge

We generated synthesized ground motion at nine locations along the San Francisco/Oakland Bay Bridge (western and eastern spans). Table 9 lists sites for the synthesis, and locations are plotted in Figure 3. The western span ranges in distance from about 12 to 15.5 Km from the Hayward fault, and the eastern span ranges in distance from about 9 to 11.5 Km. Ground motion was generated for three frequency bands, 0.0 – 0.7 Hz, 0.7 – 2.0 Hz, and 2.0 – 25.0 Hz, and merged with bandpass filtering. The lowest frequency band was modeled with finite difference, the middle frequency band with EGF's with 4.0>M > 3.0, and the highest frequency band with EGF's with magnitude M < 3.0. The magnitude ranges insured that the EGF's had effectively point sources for the frequency bands for which they were used. A four pole Butterworth filter was used at frequencies spaced to eliminate spectral holes or bumps in the frequency domain merging. EGFs for site E23 were extrapolated from E17, and those for W04 were extrapolated from W05.

Table 9: Sites for Ground Motion Synthesis

Pier Location	GM id.	latitude	longitude
Western Span			
S.F. Ancorage	SFA	37.7861	122.3893
W2	W02	37.79120	122.38525
W4	W04	37.7978	122.3775
W5	W05	37.8010	122.3737
Yerba Buena Is. Anchor	YBA	37.8094	122.3645
Eastern Span			
E2	E02	37.81427	122.35815
E7	E07	37.81847	122.34688
E17	E17	37.82086	122.33534
E23	E23	3782167	122.32867

A site transfer function developed by Baise et al. (2002) for Yerba Island was used in deconvolution to eliminate borehole effects of downgoing energy at site E2. The complex spectral ratio site transfer function of Baise et al. was used. Baise et al. identified a spectral hole in borehole recordings at location E2 due to down-going energy. Other sites in this study did not have spectral holes in the EGF's. The borehole at E2 was deeper into bedrock than at the other sites. It is assumed that at other sites,

the EGF's were recorded close enough to the surface or that the soil overburden was soft enough to absorb down going energy. So, synthesized ground motions in this report are records of up going energy that can be used directly into soil models or structural models.

We modeled ground motion for two rupture models that were identified as the mean and one standard deviation models (discussed previously and shown in Figures 37 and 39); models HAY06 and HAY31, respectively. Figures 41-43 show ground motion accelerations (g), velocities (cm/sec), and displacements (cm), at the five locations along the western span of the bridge for fault rupture model HAY06 and for component N223E. This component direction is parallel to the span, and roughly perpendicular to the Hayward fault. Figures 44-46 show commensurate ground motions for component N313. This component direction is perpendicular to the span. Figures 47-49 show commensurate ground motions for the vertical component. Figures 50 – 58 show commensurate ground motions for the eastern span. The effect of an asperity at the northern end of the Hayward fault is seen as late arriving energy on the acceleration records. The eastern span is rotted relative to the western span, so components are N252E for bridge parallel and N342E for bridge perpendicular directions. Figures 59-76 show the same ground motions for fault rupture model HAY31.

It is interesting that the "mean" fault rupture model (HAY06) generated greater long period ground displacements at the bridge than the "one standard deviation" model (HAY31), However, the "one standard deviation" model created greater accelerations. While, both models had comparable velocities. The HAY031 rupture model has near unilateral rupture away from the bridge and the near field pulse and far-field shear waves are not as large as for rupture model HAY06. However, in the high frequency accelerations the amplitudes are greater and the duration longer than for the bilateral rupture model (HAY06).

For the HAY06 model, the bridge perpendicular component of ground motions (N313E and N342E) for the western and eastern spans, respectively, are significantly greater than the bridge parallel motion (N223E and N332E) component. This is partly because these components are aligned close to the strike of the Hayward fault, so what one observes is the tectonic plate "rebound" during the earthquake. However, for the HAY31 model, the component of ground motions (N223E and N242E) for the western and eastern spans are roughly the same, with the bridge parallel motions slightly greater. Clearly, the rupture model and final fault dislocation offsets and orientation have a significant impact on the displacements at the bridge. In both models, accelerations, velocities, and displacements generally decrease for positions farther from the fault.

Displacements show final static offset values. For the HAY06 model, the western bridge moved about 65 cm north and the eastern bridge moved 110 cm north as a result of the earthquake. The bridges moved about 35 and 75 cm west, respectively. For the

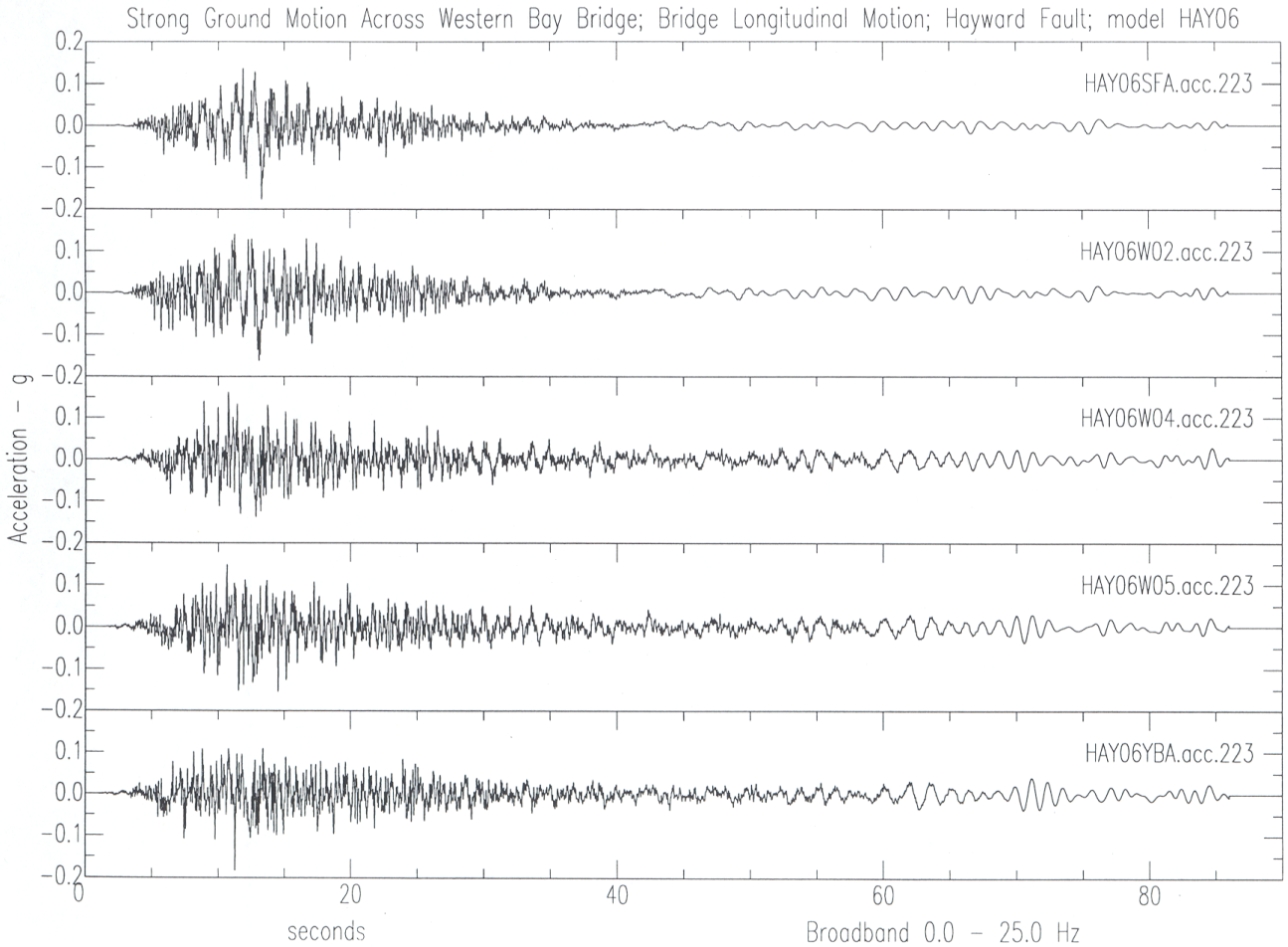

Figure 41: Bridge parallel accelerations (g), eastern span, rupture model HAY06.

Mor

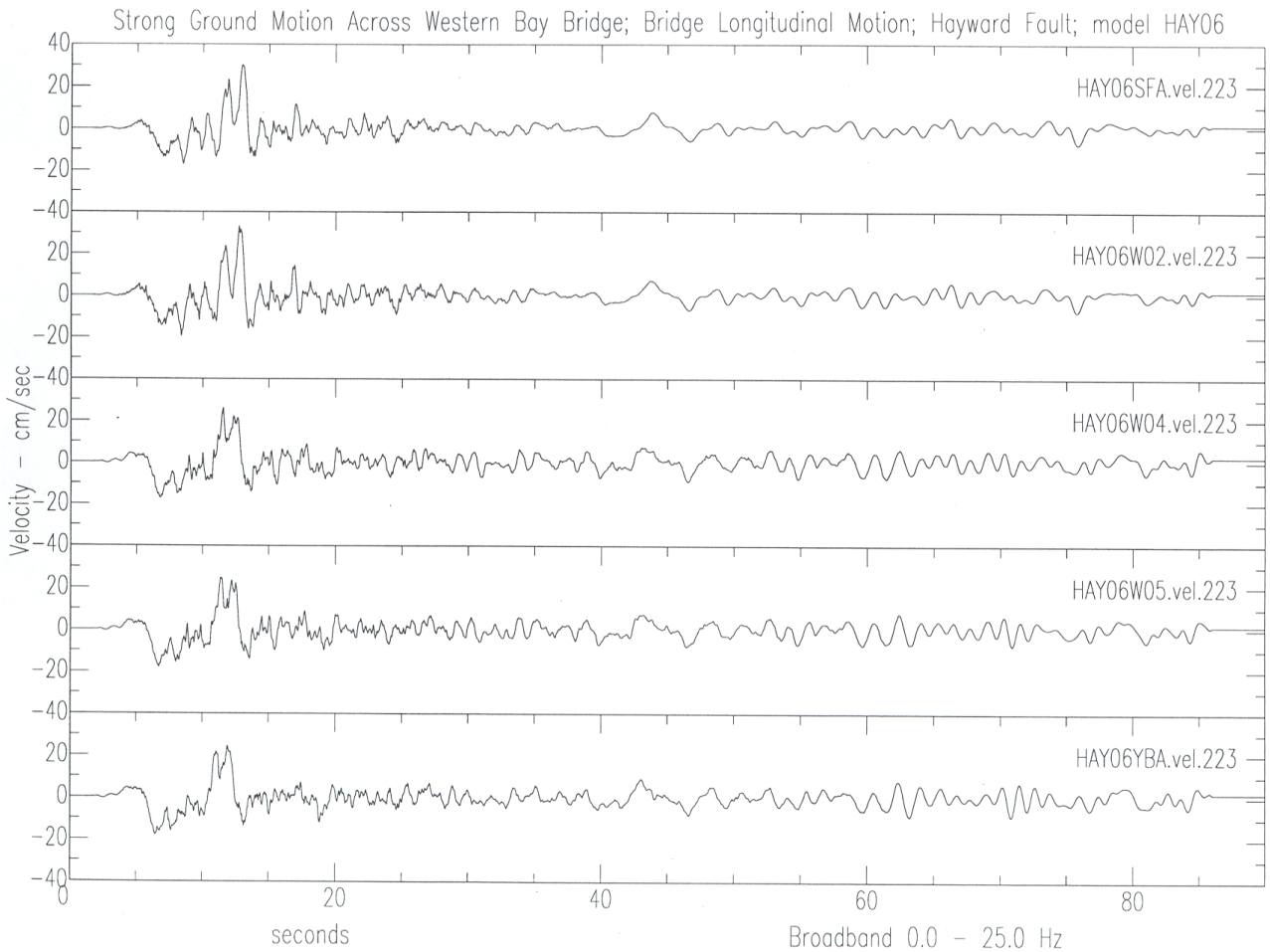

Figure 42: Bridge parallel velocities (cm/sec), eastern span, rupture model HAY06.

Sat

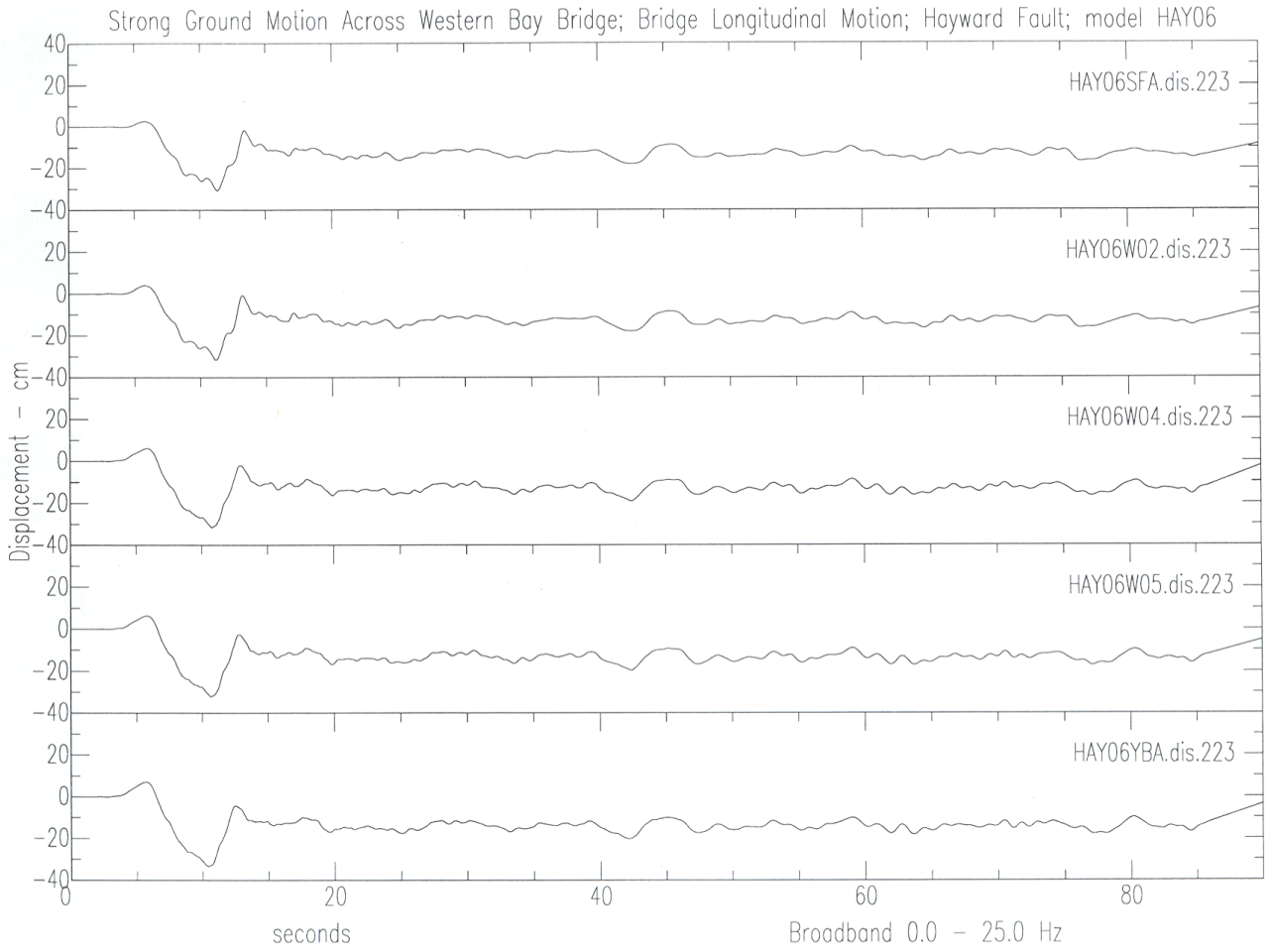

Figure 43: Bridge parallel displacements (cm), eastern span, rupture model HAY06.

Sat

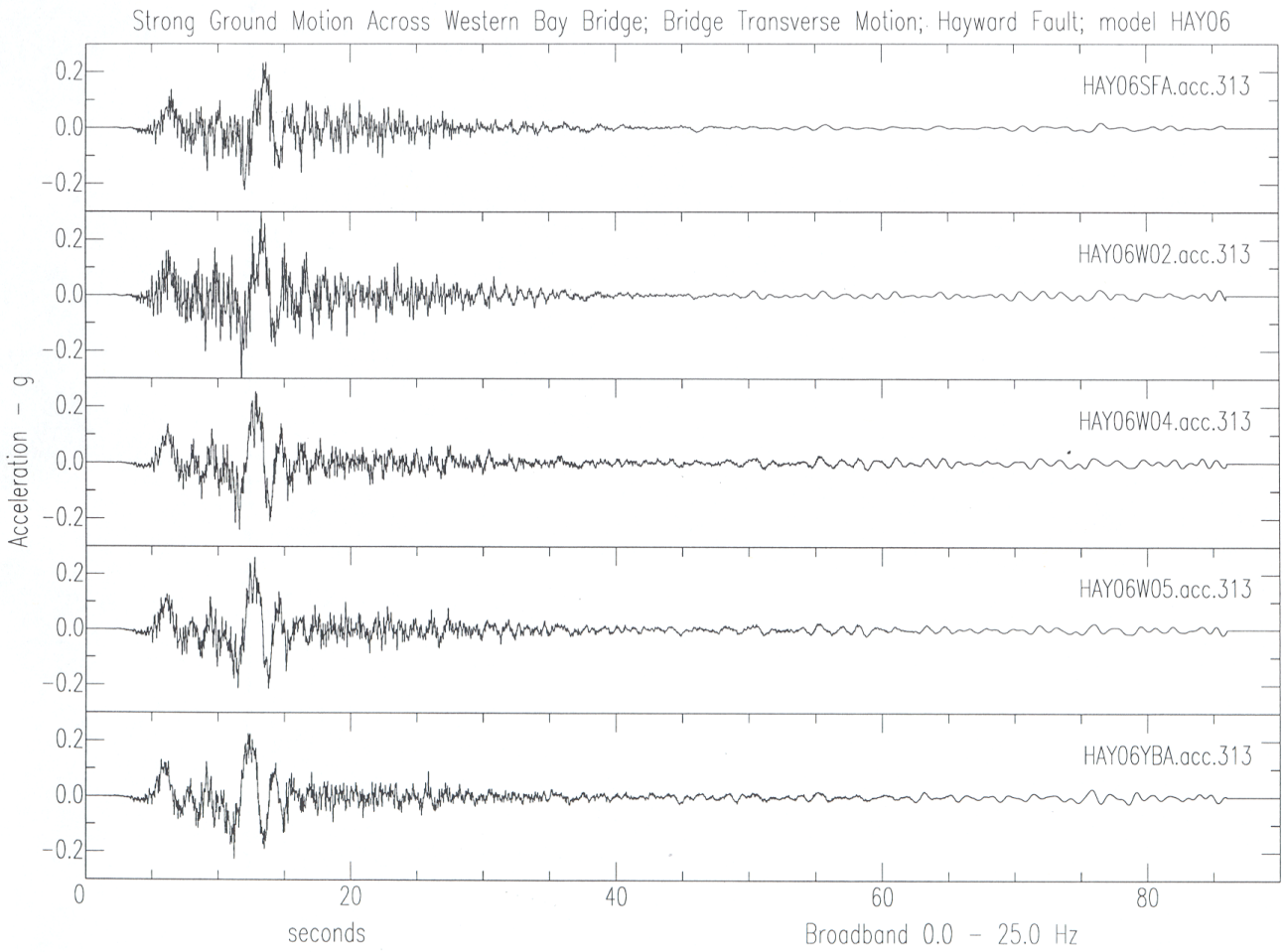

Figure 44: Bridge transverse accelerations (g), eastern span, rupture model HAY06.

Sat

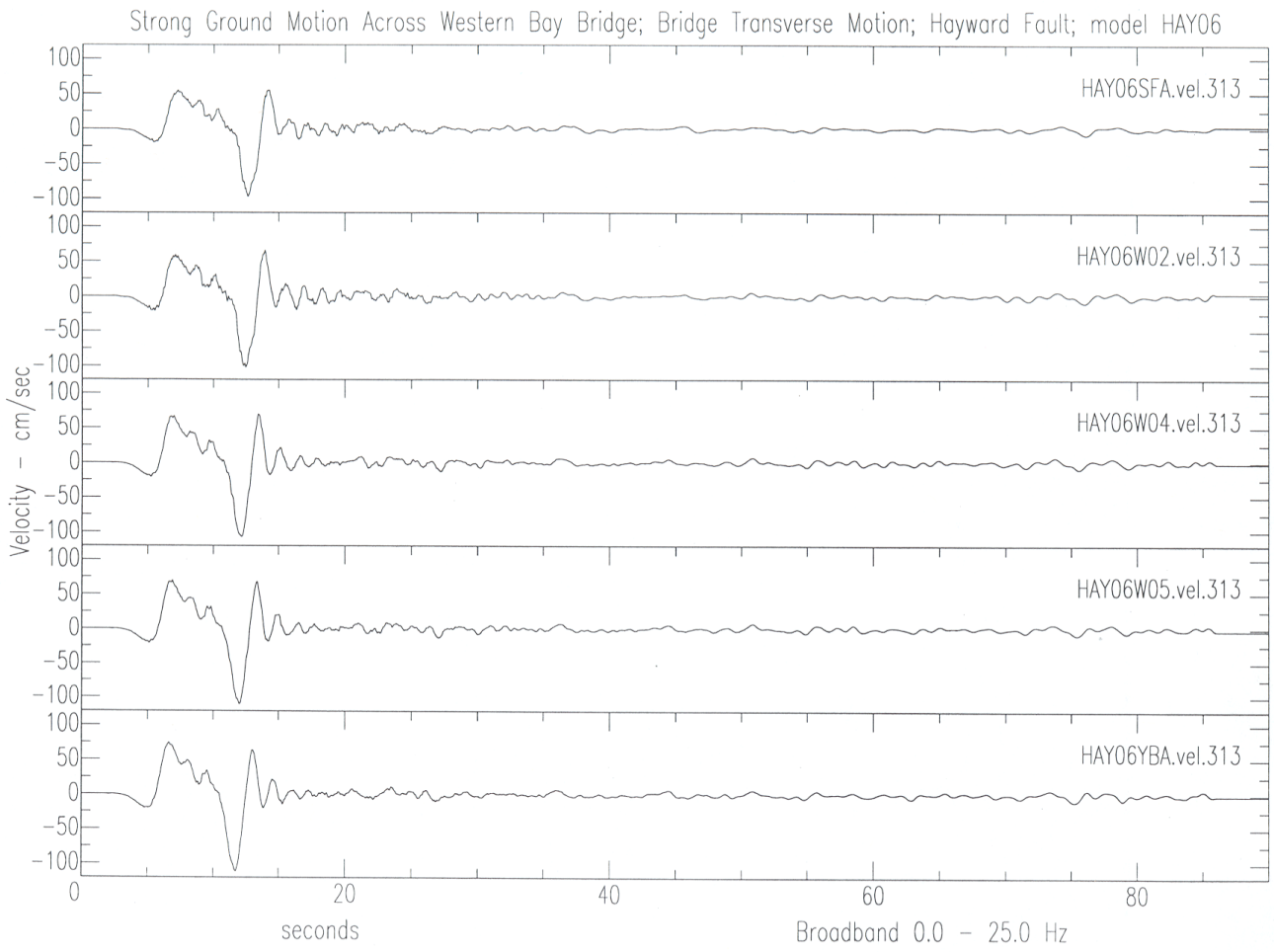

Figure 45: Bridge transverse velocities (cm/sec), eastern span, rupture model HAY06.

Sat

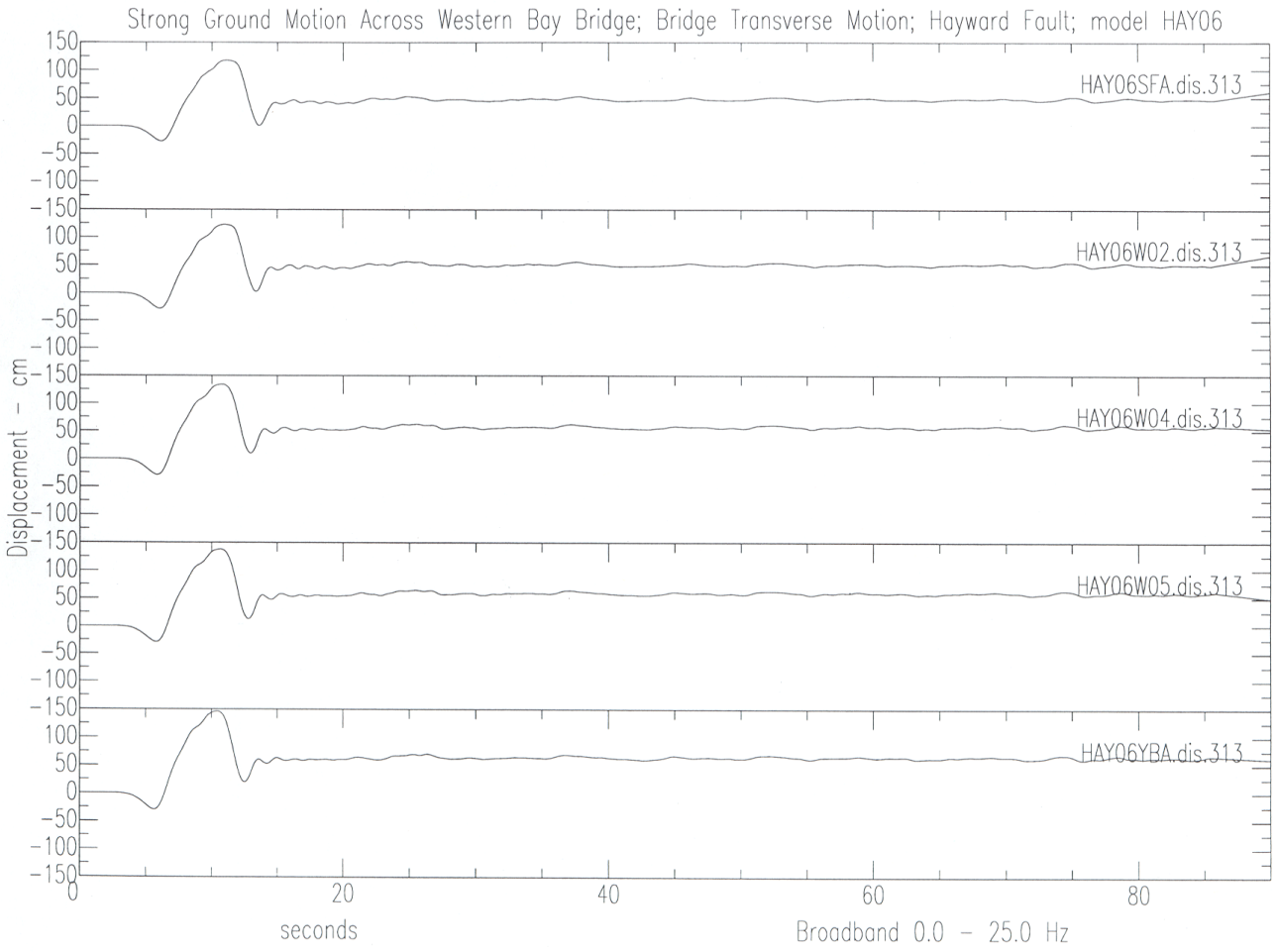

Figure 46: Bridge transverse displacements (cm), eastern span, rupture model HAY06.

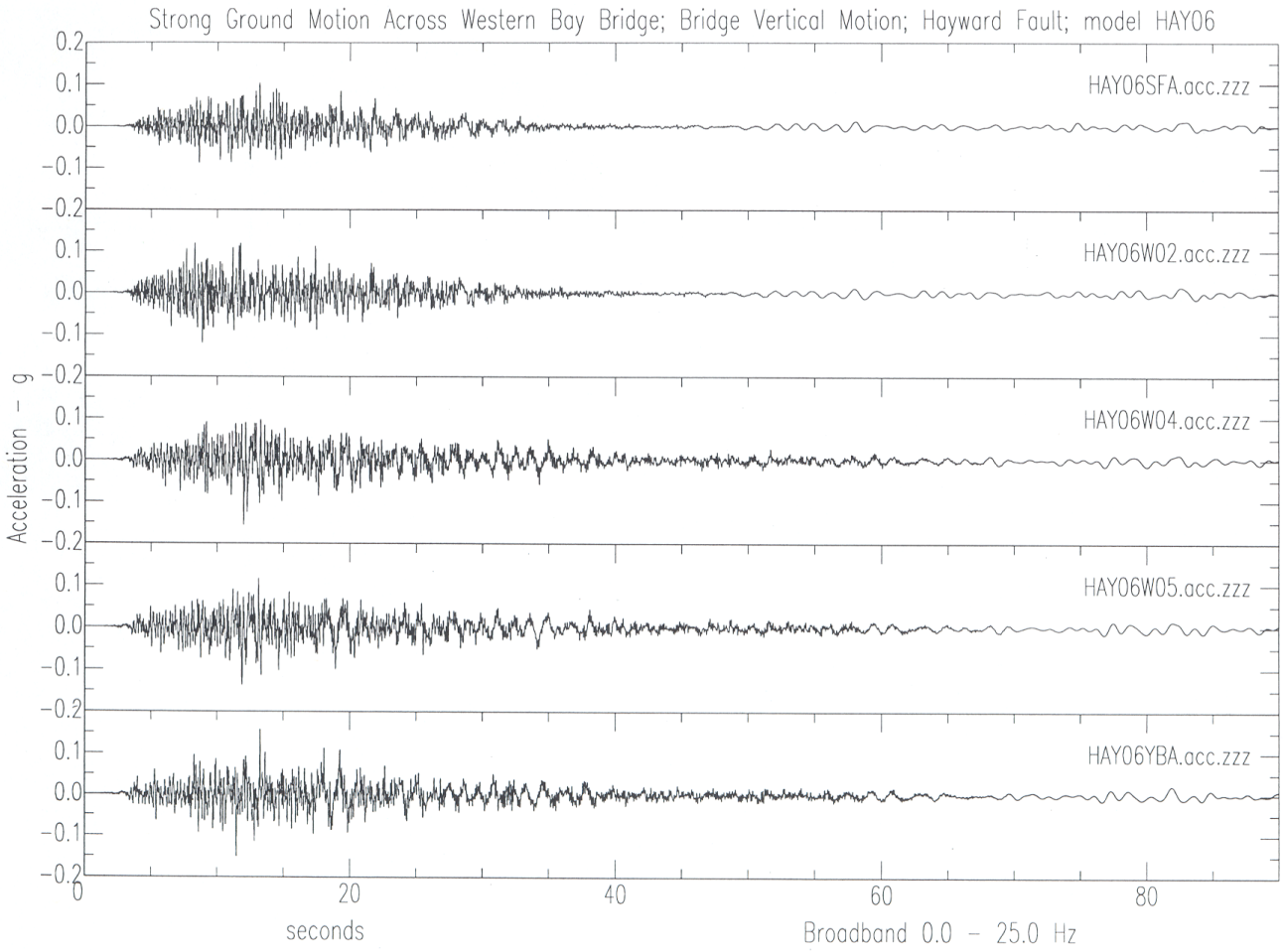

Figure 47: Bridge vertical accelerations (g), eastern span, rupture model HAY06.

Sat

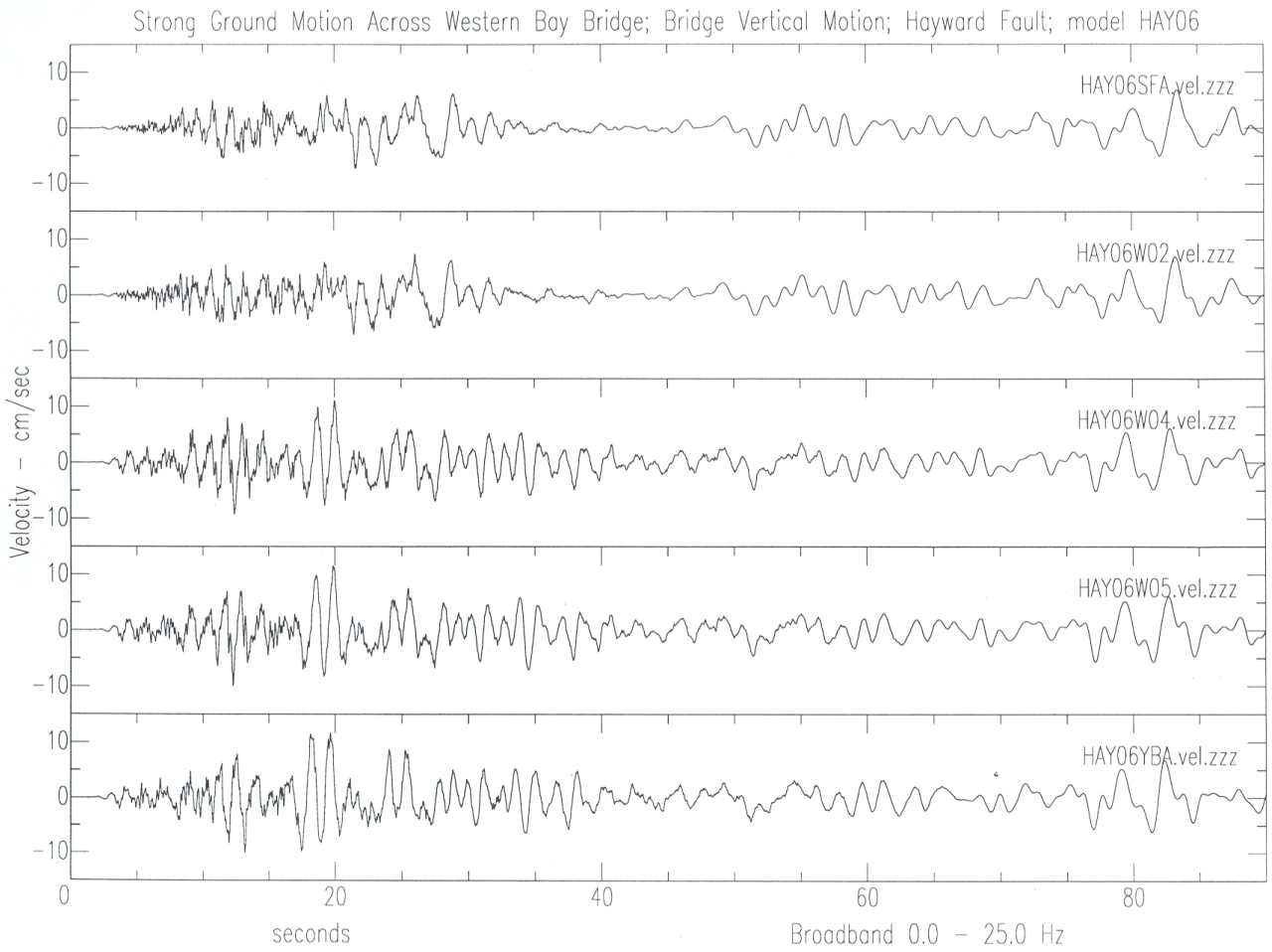

Figure 48: Bridge vertical velocities (cm/sec), eastern span, rupture model HAY06.

Sat

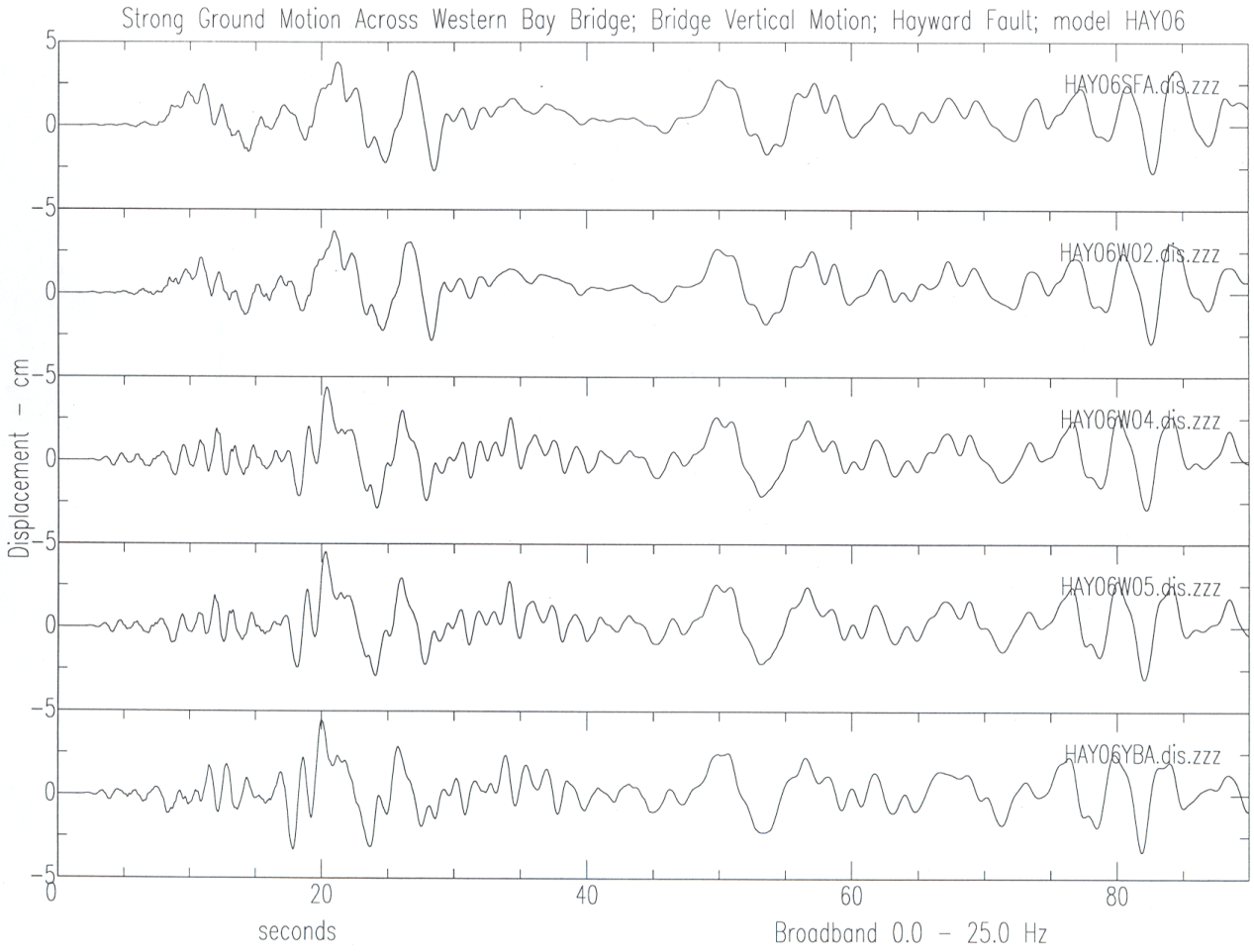

Figure 49: Bridge vertical displacements (cm), eastern span, rupture model HAY06.

Mor

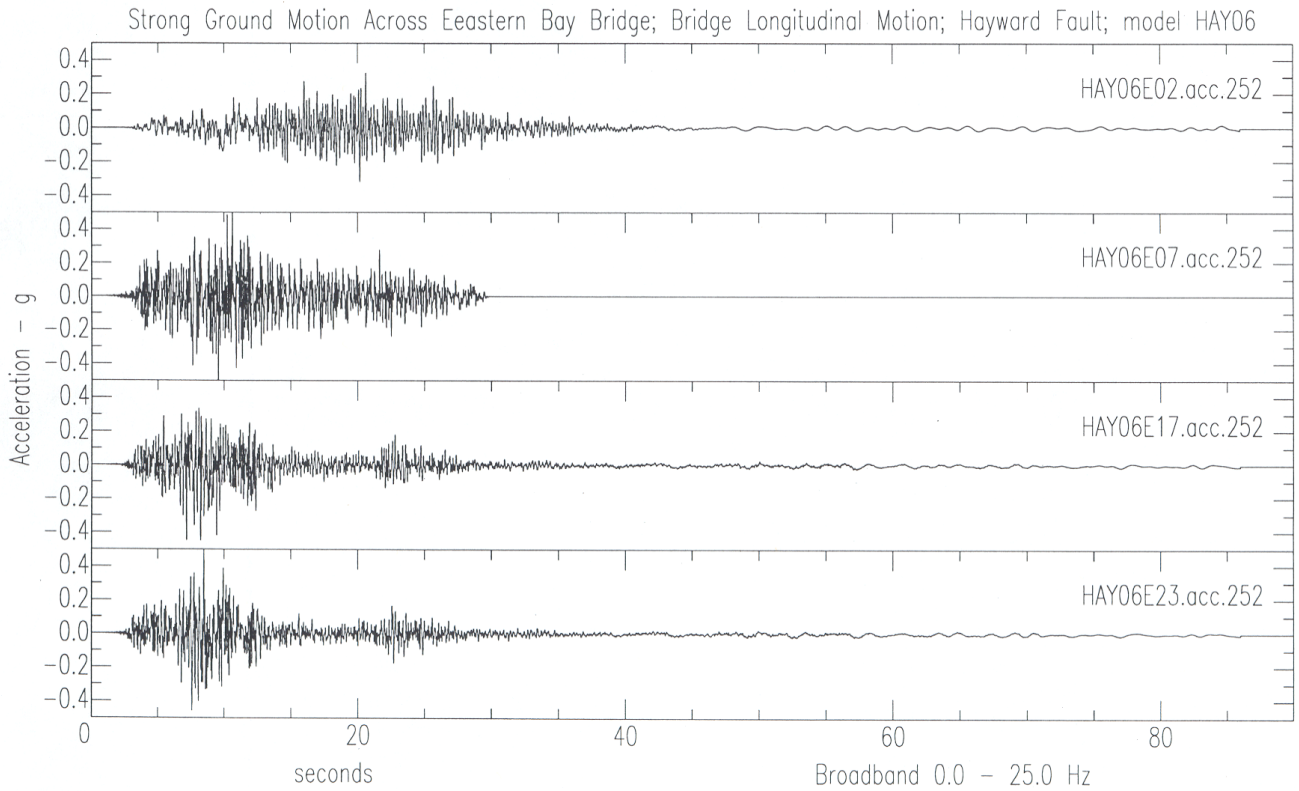

Figure 50: Bridge parallel accelerations (g), western span, rupture model HAY06.

Mor

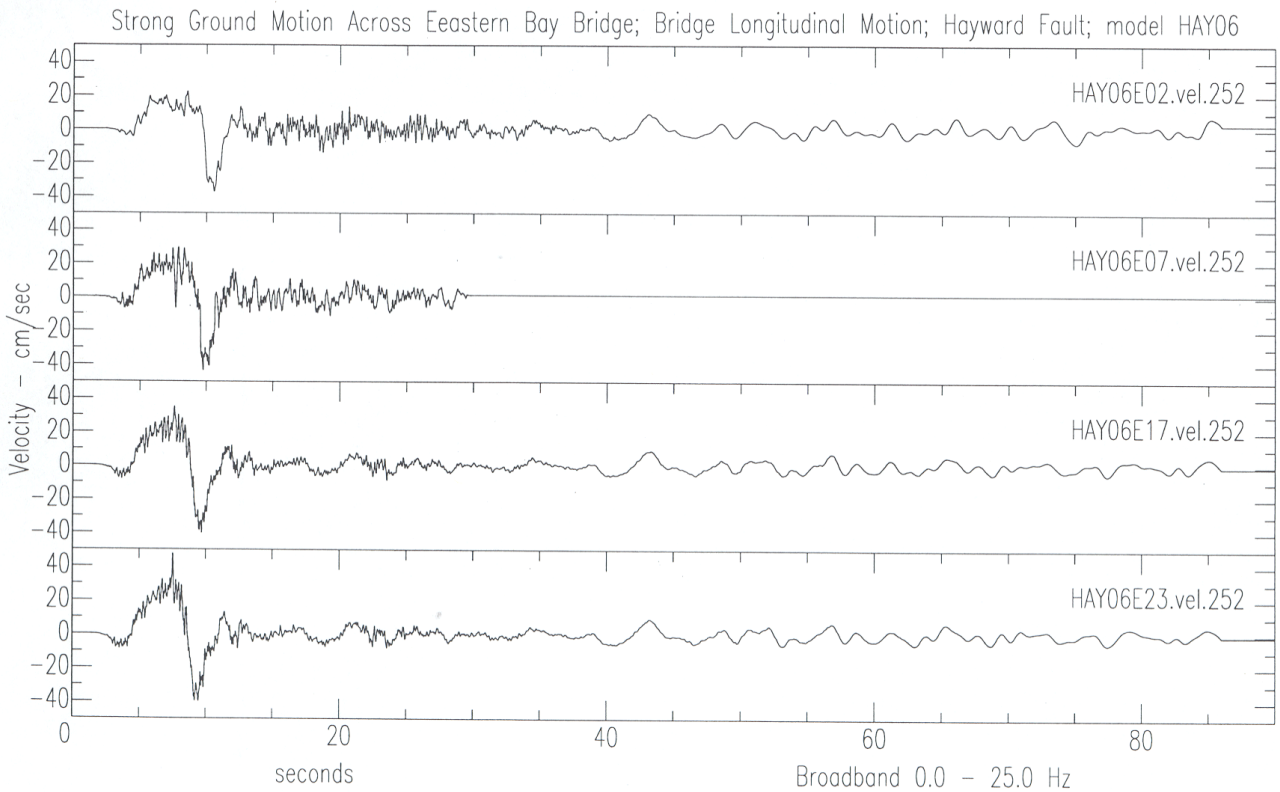

Figure 51: Bridge parallel velocities (cm/sec), western span, rupture model HAY06.

Mor

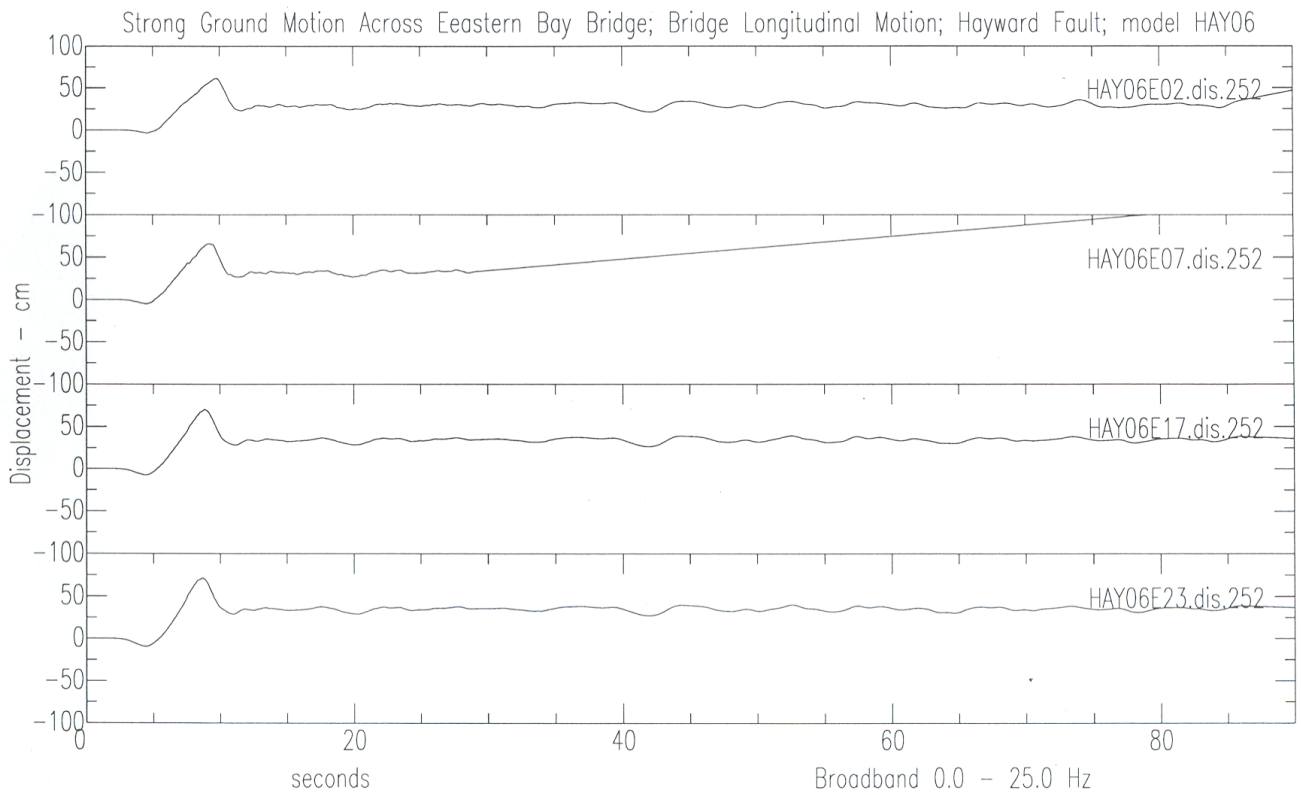

Figure 52: Bridge parallel displacements (cm), western span, rupture model HAY06.

Mor

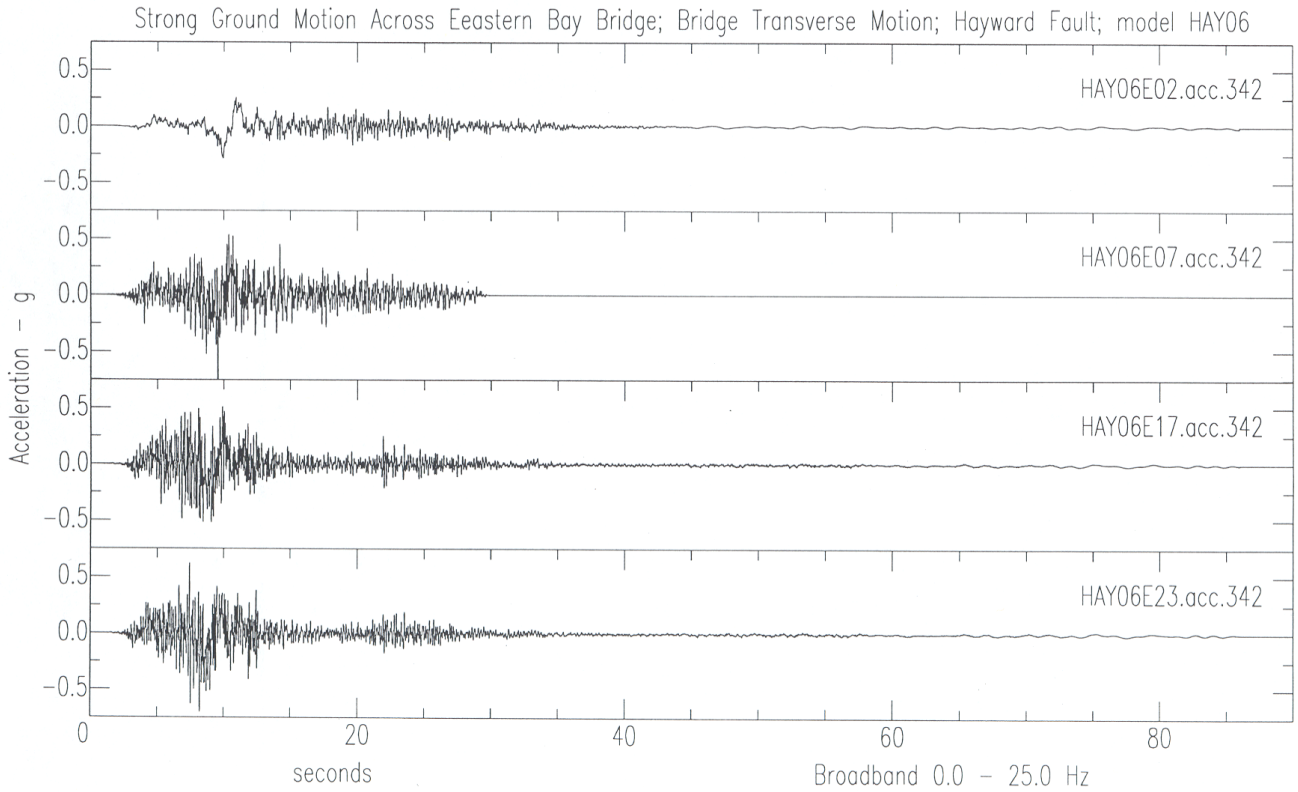

Figure 53: Bridge transverse accelerations (g), western span, rupture model HAY06.

Mor

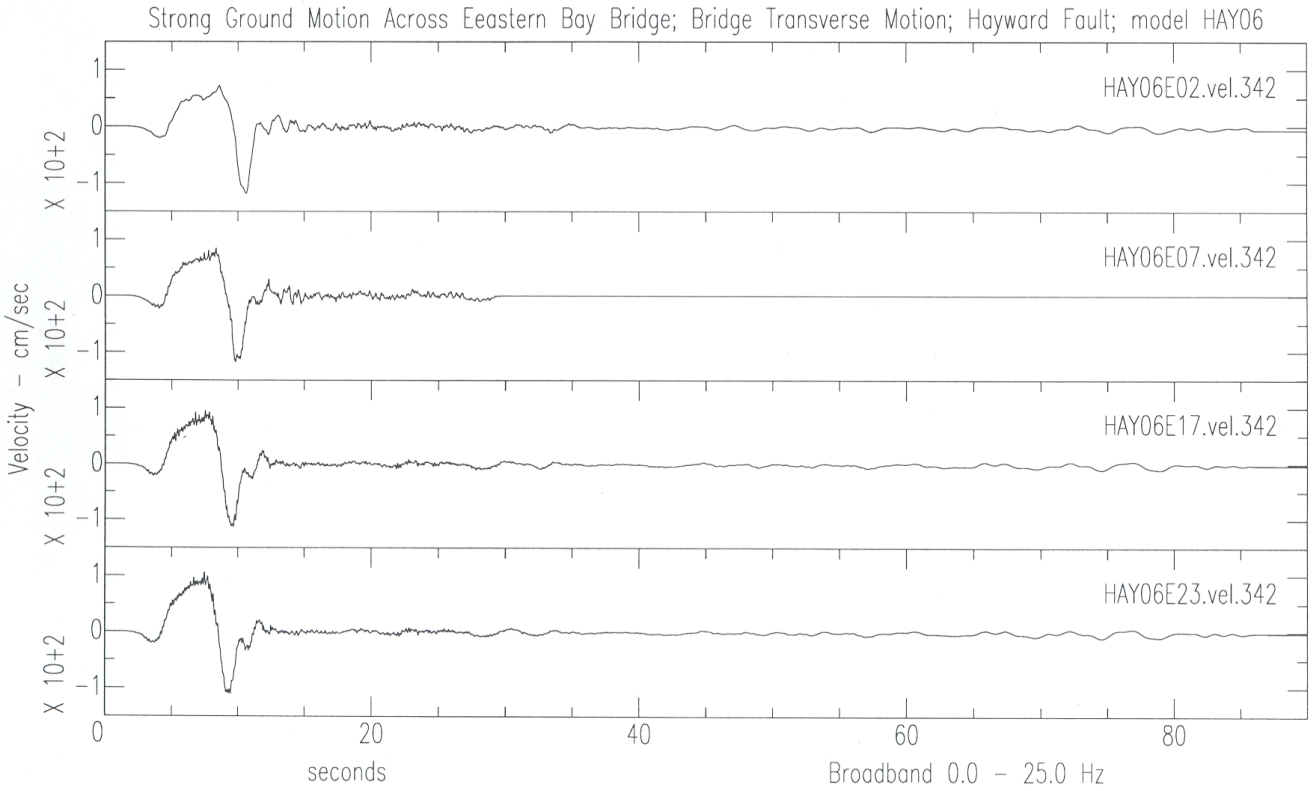

Figure 54: Bridge transverse velocities (cm/sec), western span, rupture model HAY06.

Mor

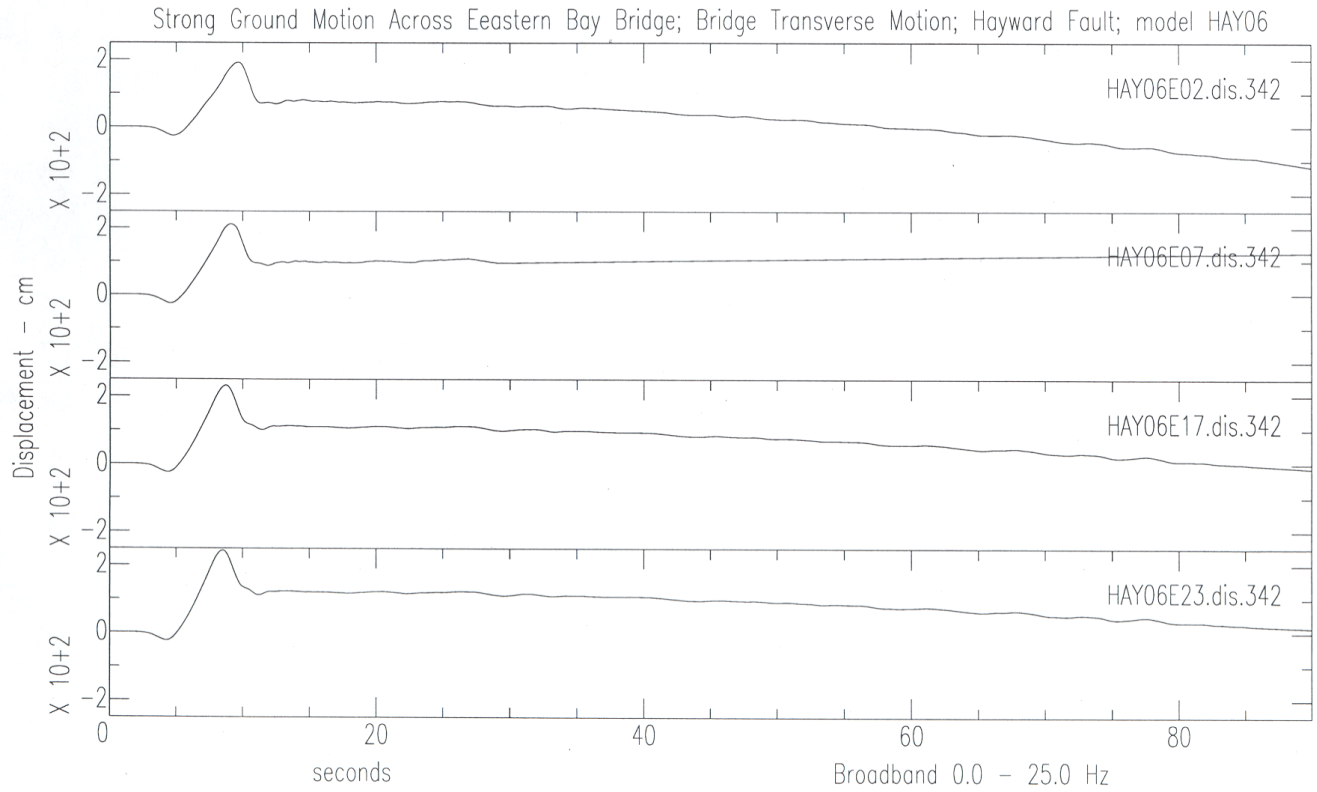

Figure 55: Bridge transverse displacements (cm), western span, rupture model HAY06.

Mor

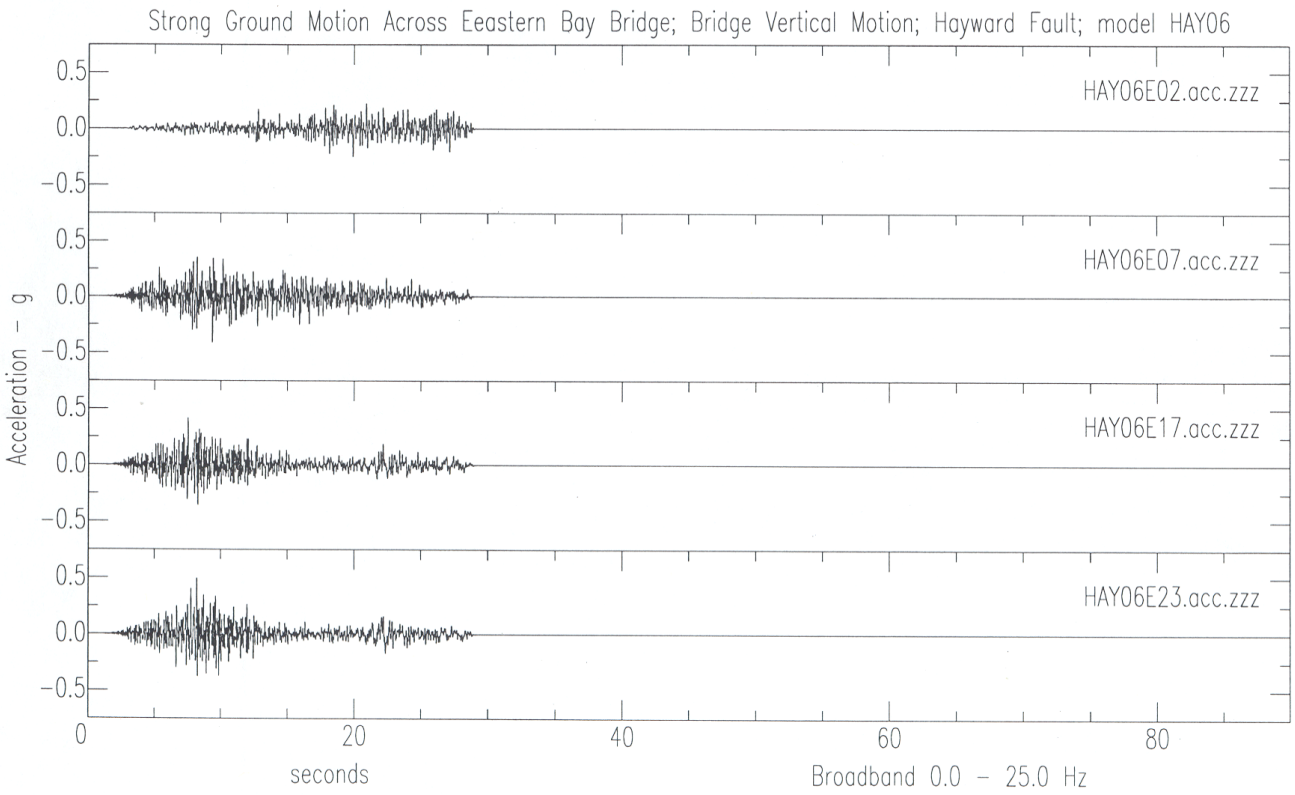

Figure 56: Bridge vertical accelerations (g), western span, rupture model HAY06.

Mor

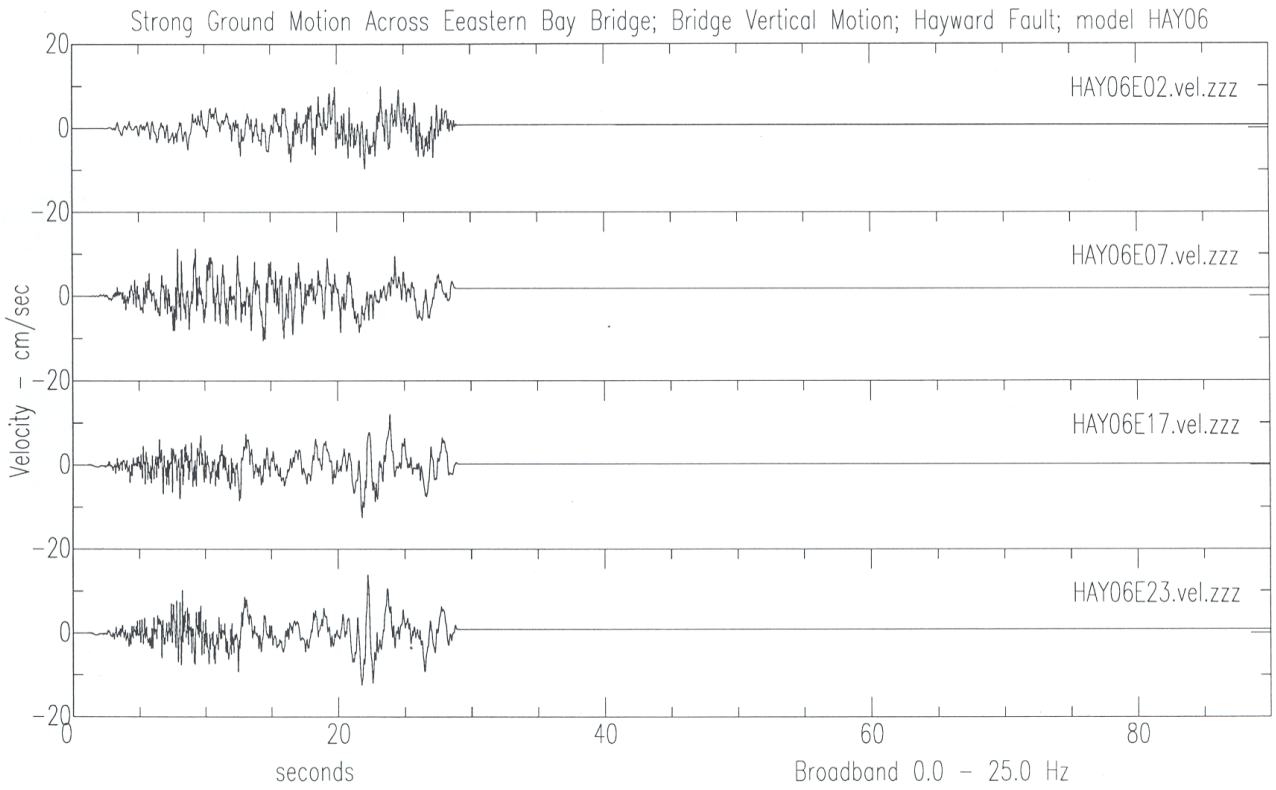

Figure 57: Bridge vertical velocities (cm/sec), western span, rupture model HAY06.

Mor

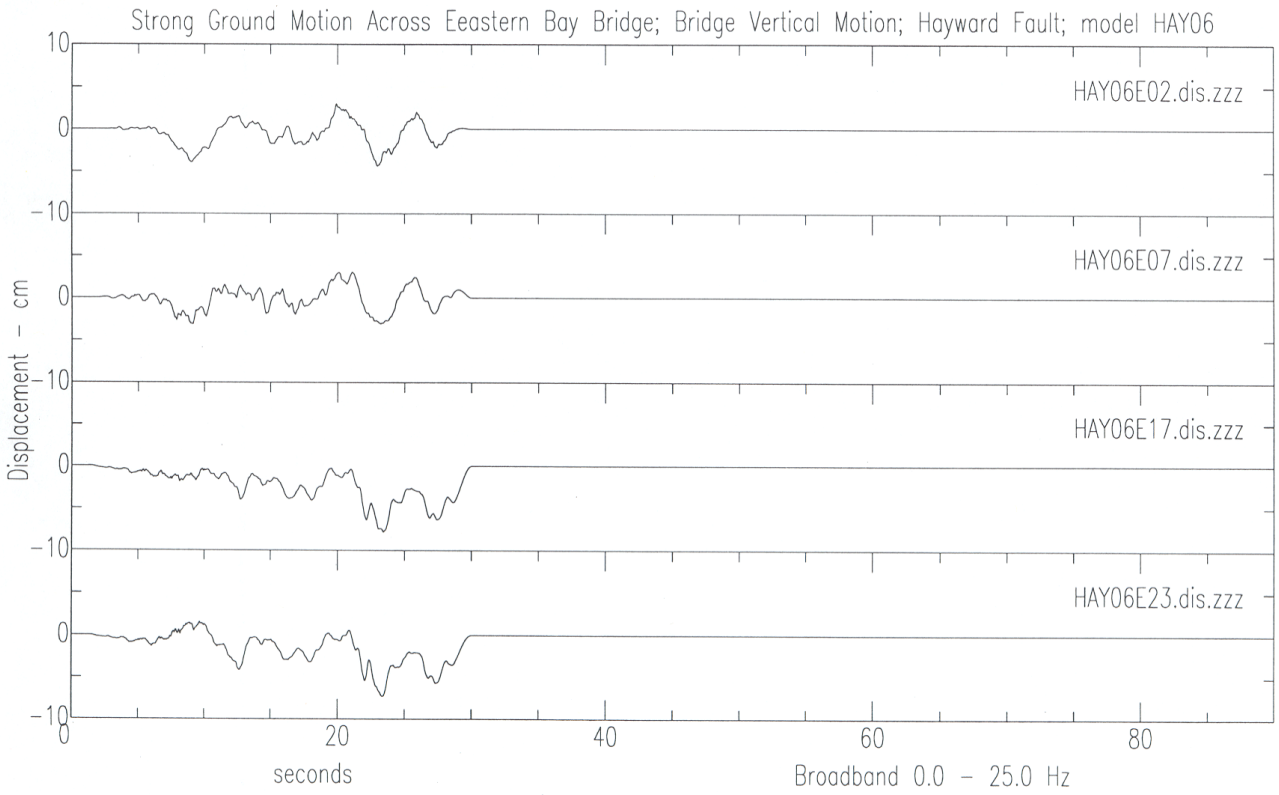

Figure 58: Bridge vertical displacements (cm), western span, rupture model HAY06.

Mor

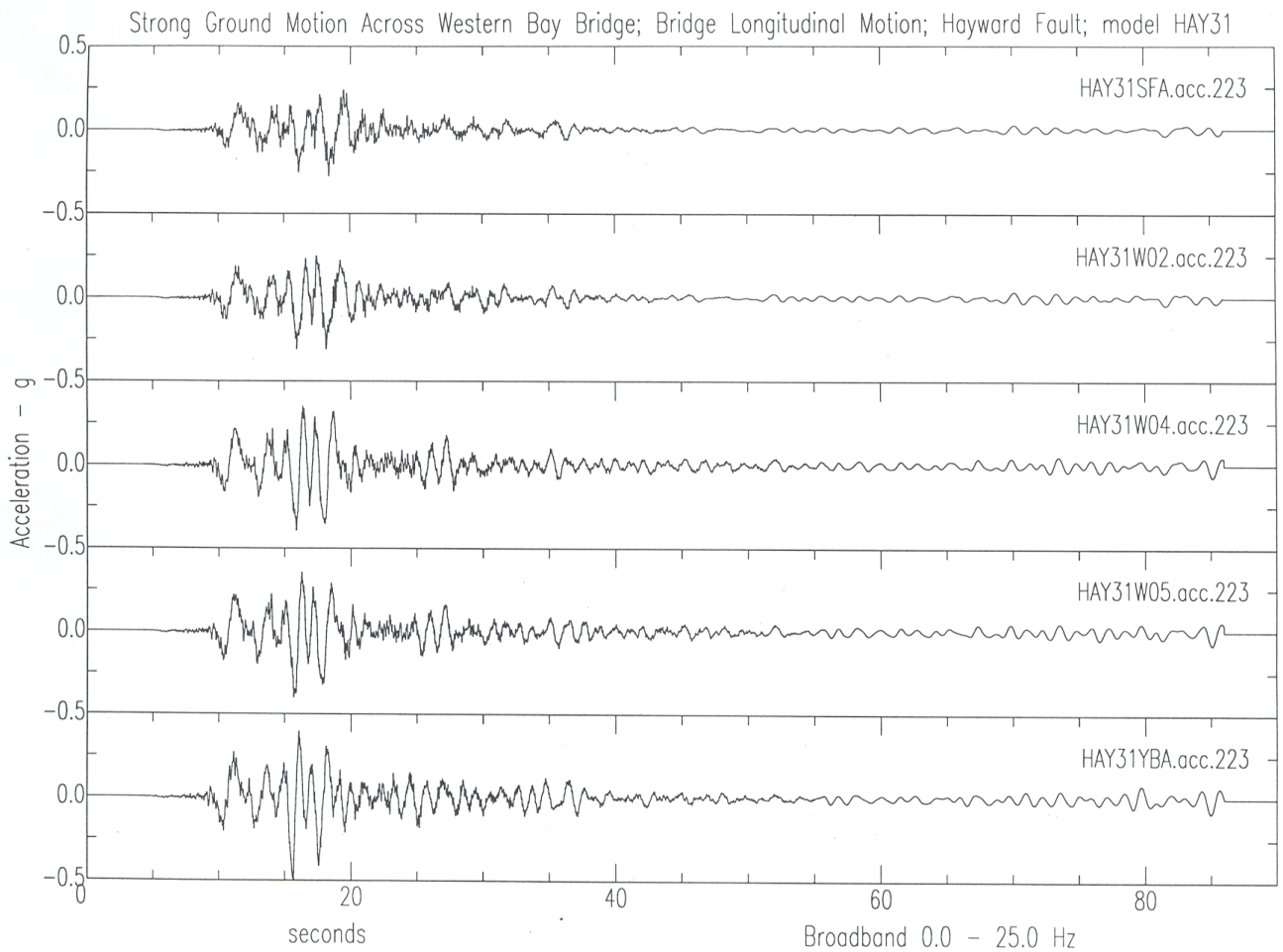

Figure 59: Bridge parallel accelerations (g), western span, rupture model HAY31.

Mor

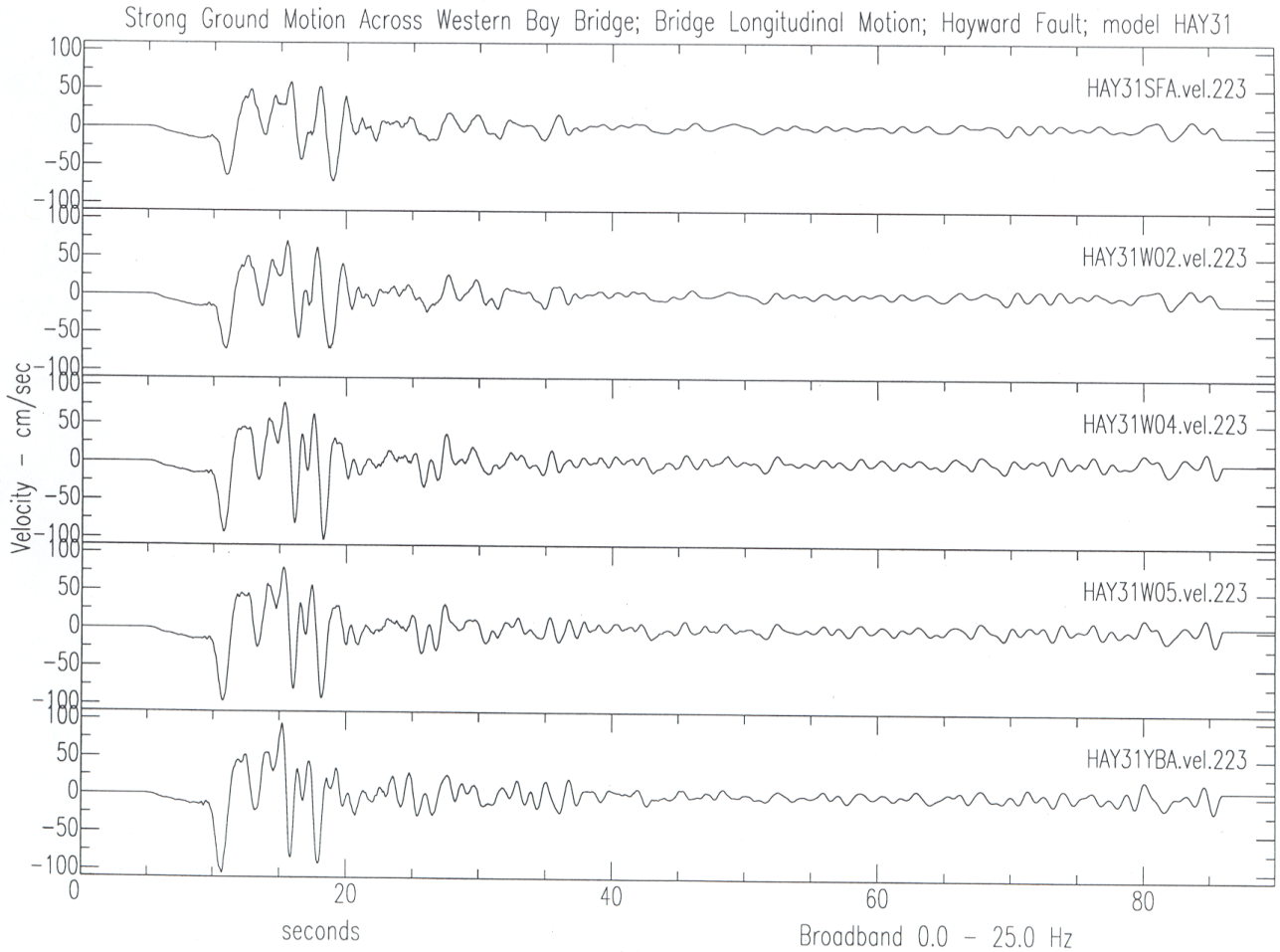

Figure 60: Bridge parallel velocities (cm/sec), western span, rupture model HAY31.

Mor

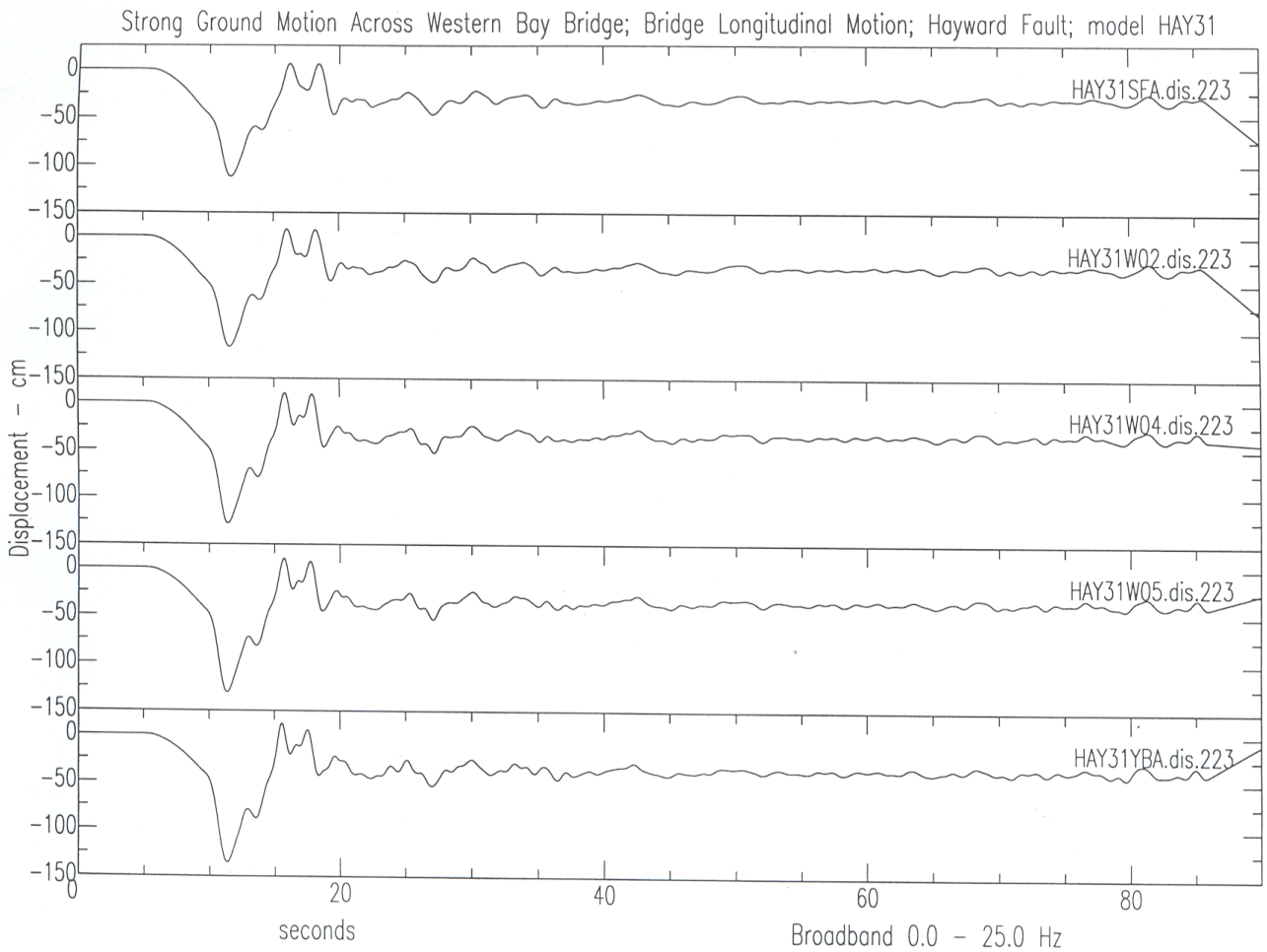

Figure 61: Bridge parallel displacements (cm), western span, rupture model HAY31.

Mor

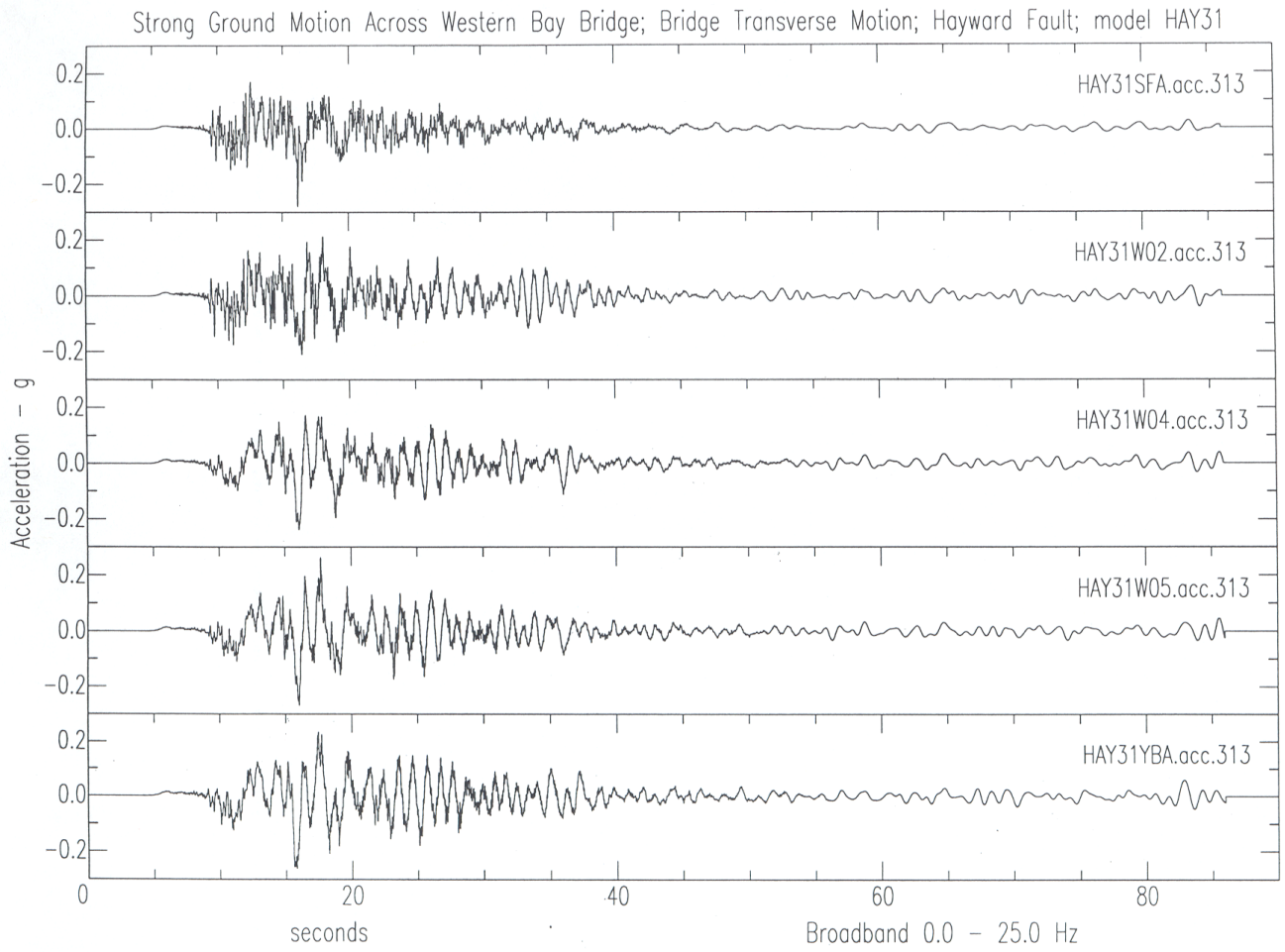

Figure 62: Bridge transverse accelerations (g), western span, rupture model HAY31.

Mor

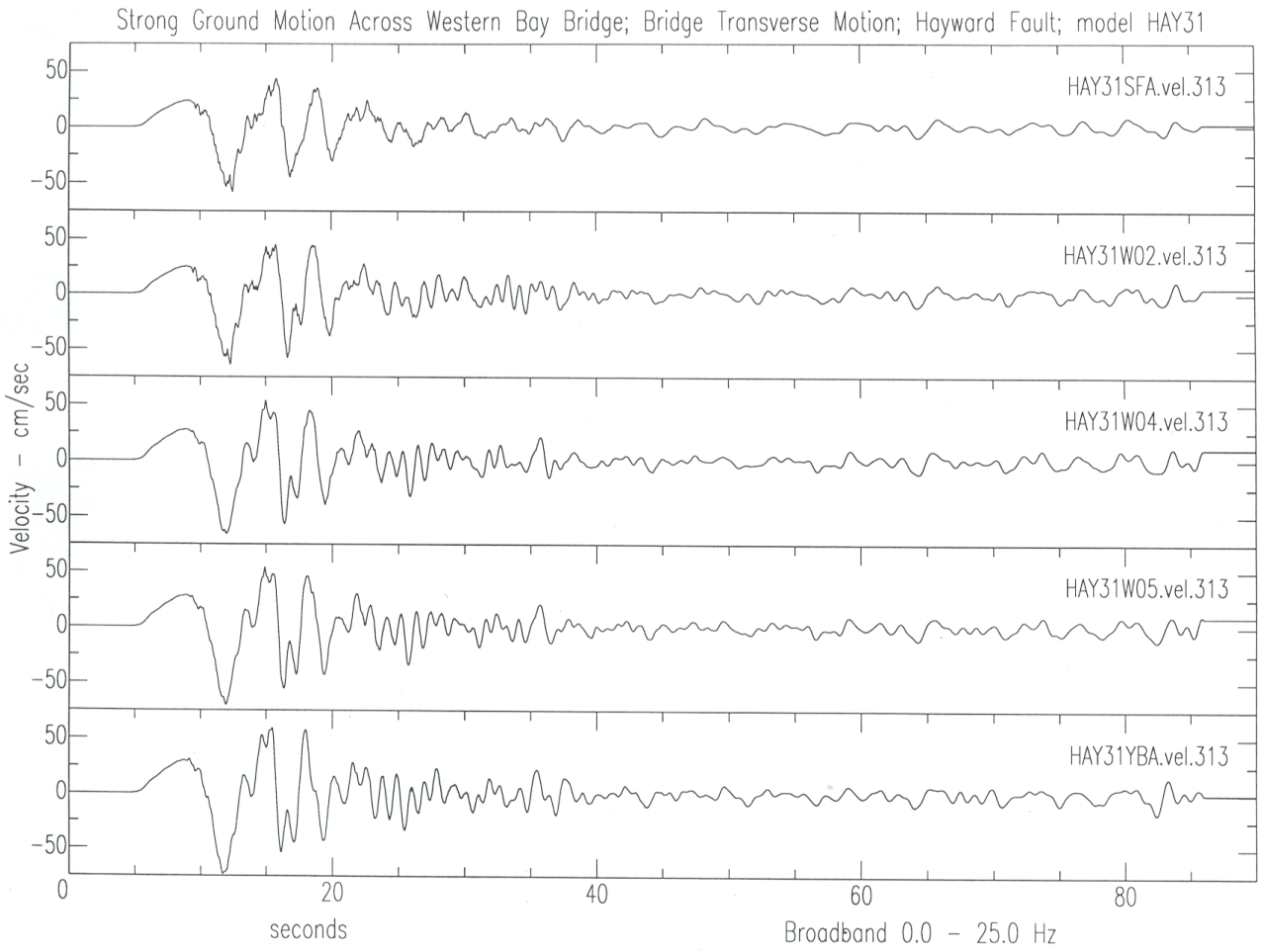

Figure 63: Bridge transverse velocities (cm/sec), western span, rupture model HAY31.

Mor

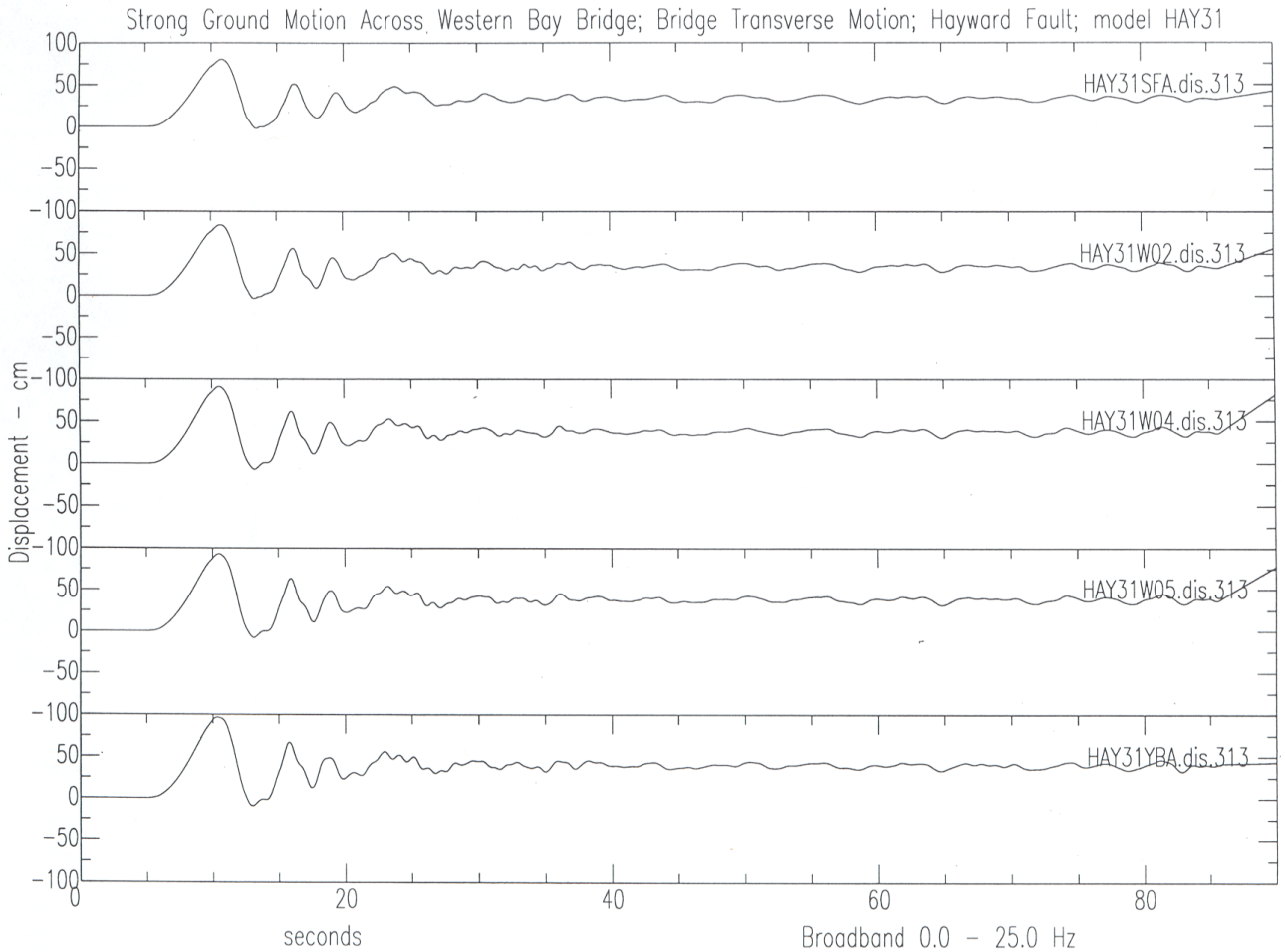

Figure 64: Bridge transverse displacements (cm), western span, rupture model HAY31.

Mor

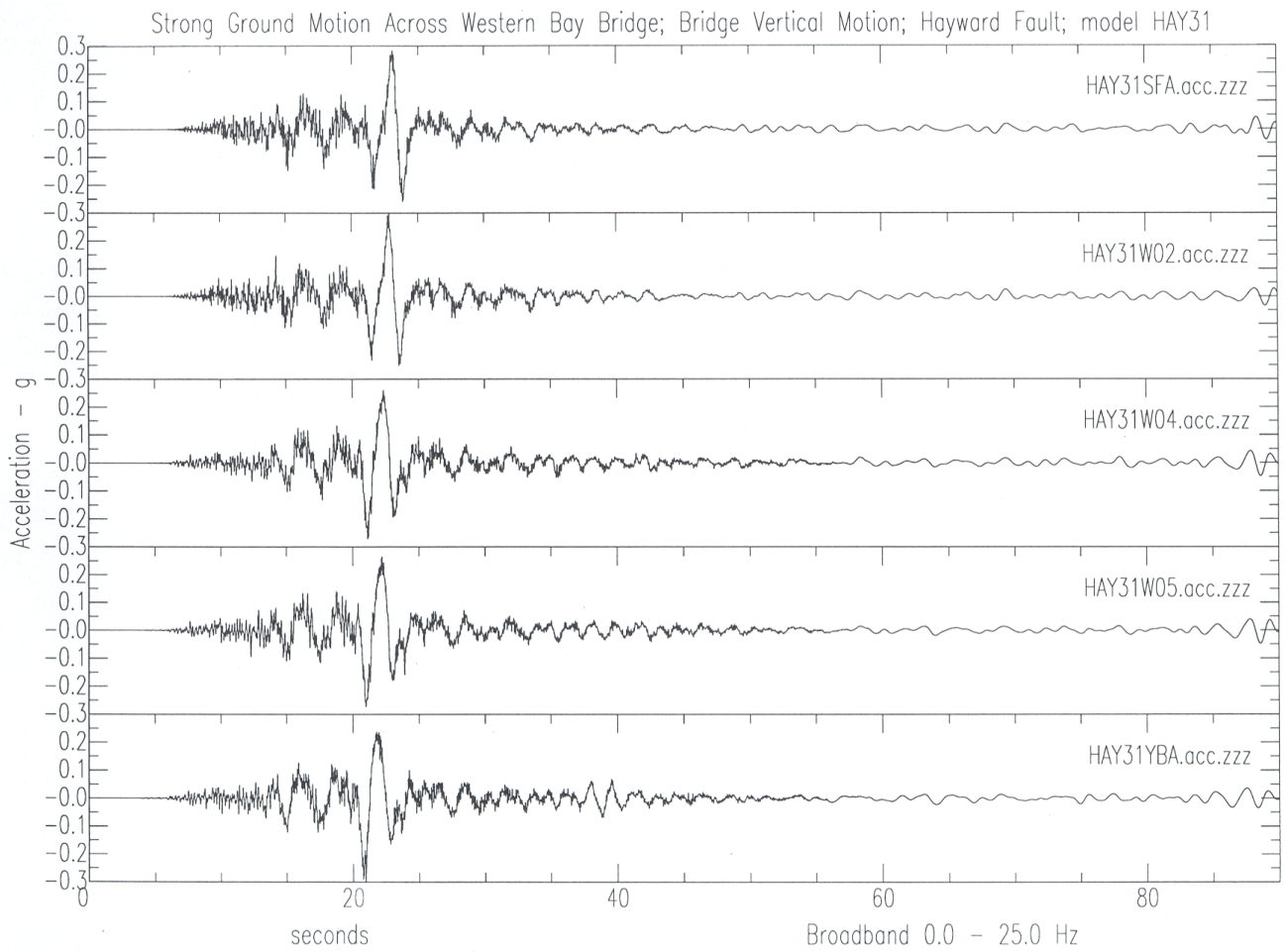

Figure 65: Bridge vertical accelerations (g), western span, rupture model HAY31.

Mor

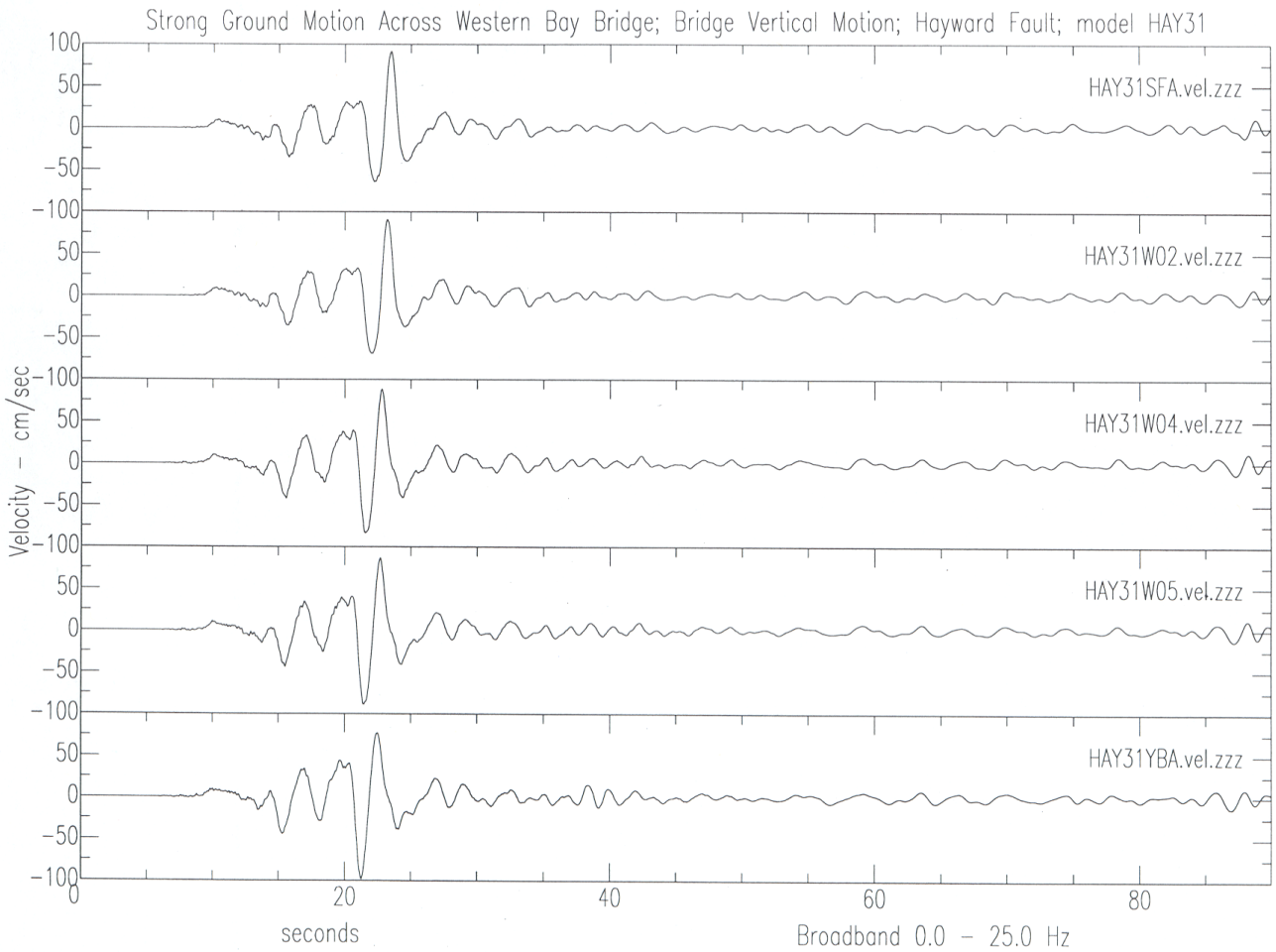

Figure 66: Bridge vertical velocities (cm/sec), western span, rupture model HAY31.

Mor

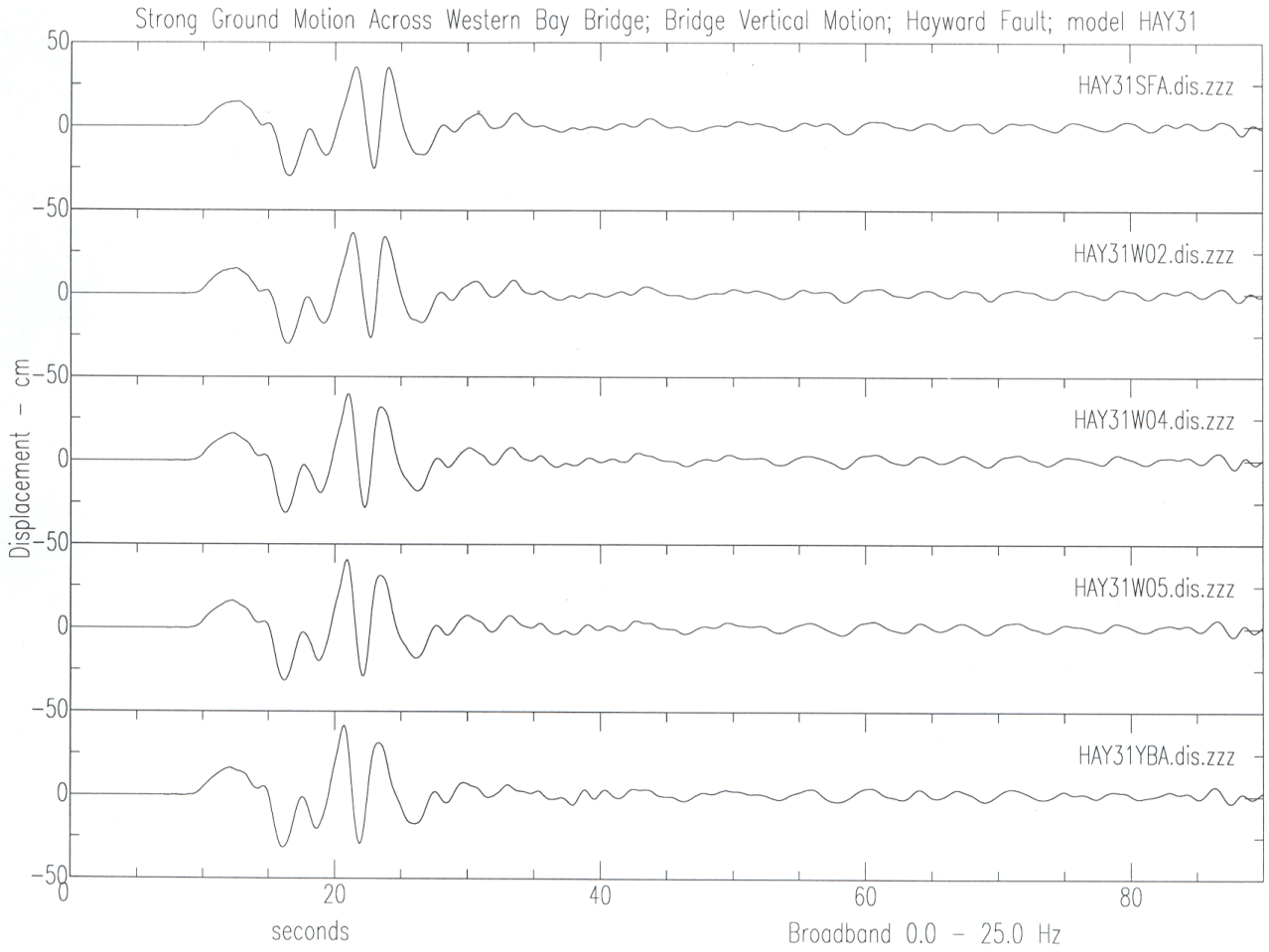

Figure 67: Bridge vertical displacements (cm), western span, rupture model HAY31.

Mor

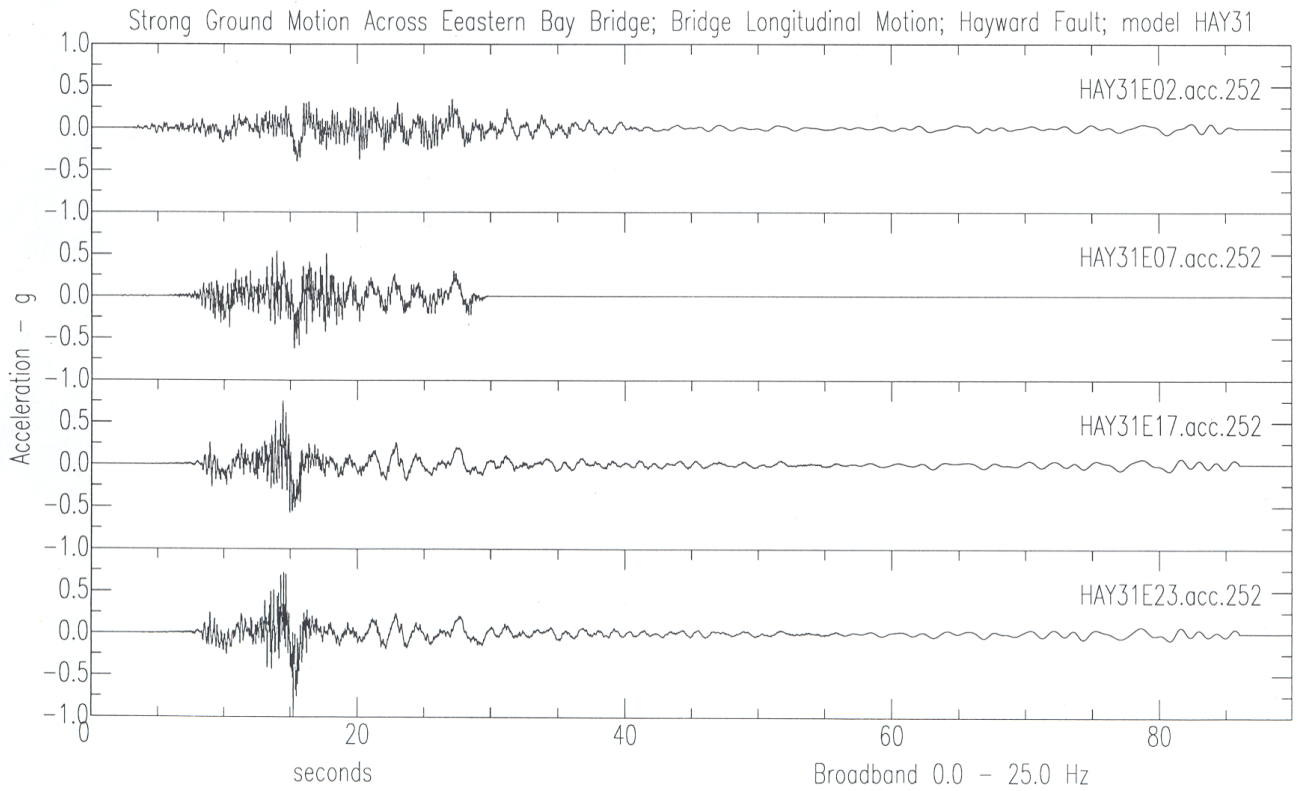

Figure 68: Bridge parallel accelerations (g), eastern span, rupture model HAY31.

Mor

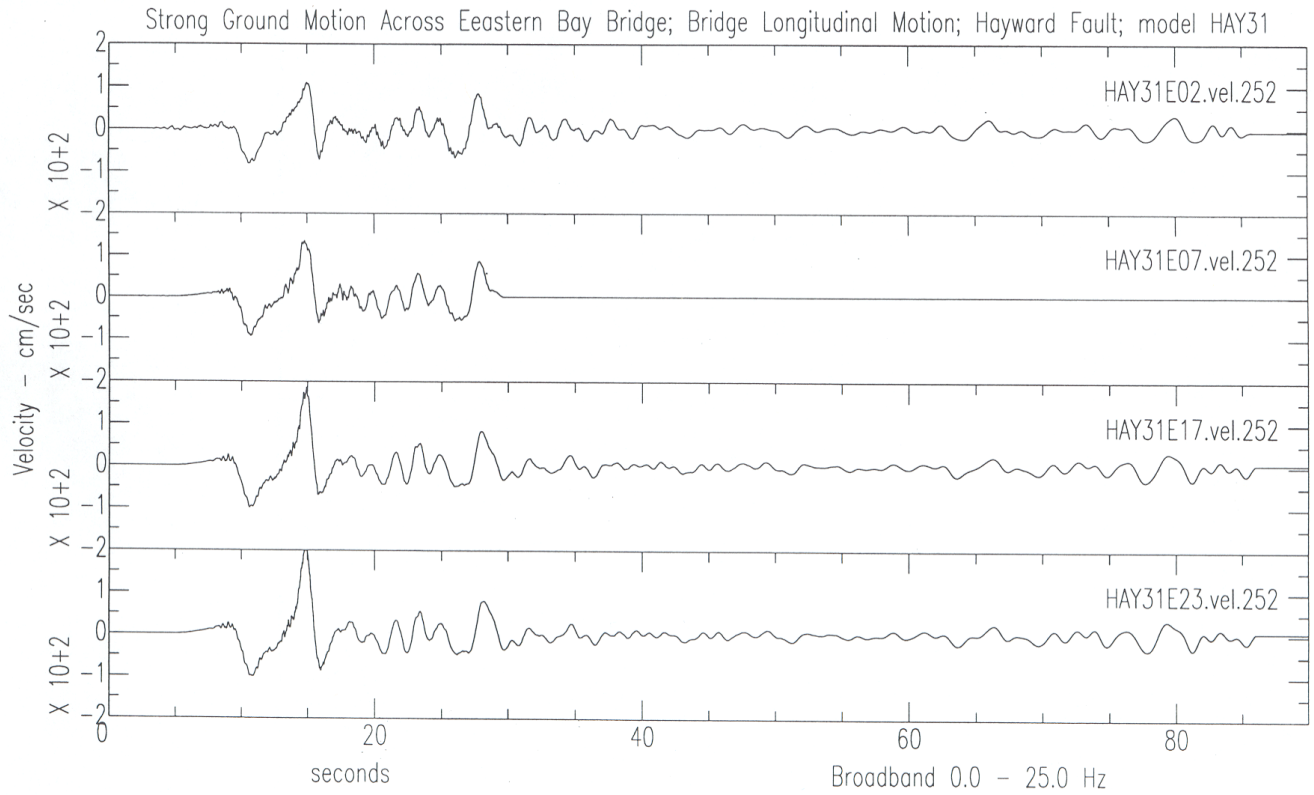

Figure 69: Bridge parallel velocities (cm/sec), eastern span, rupture model HAY31.

Mor

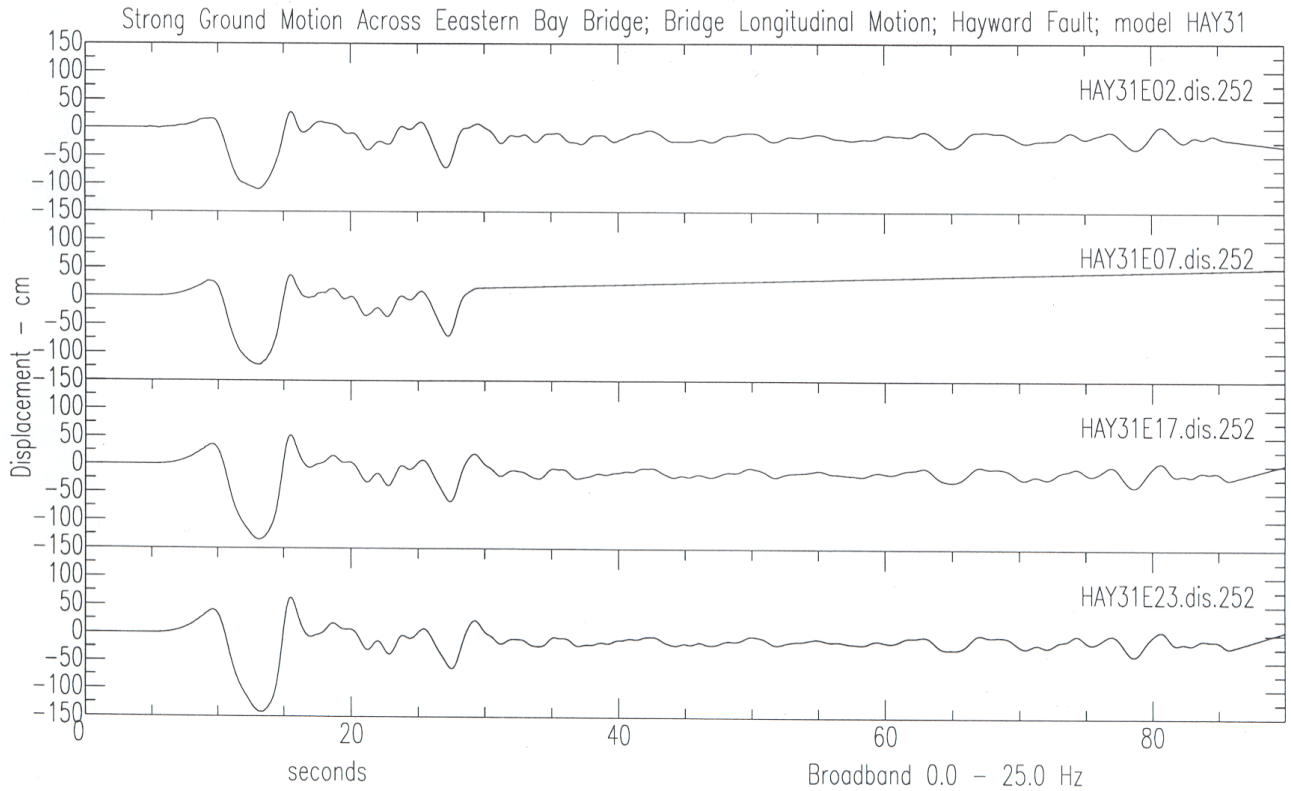

Figure 70: Bridge parallel displacements (cm), eastern span, rupture model HAY31.

Mor

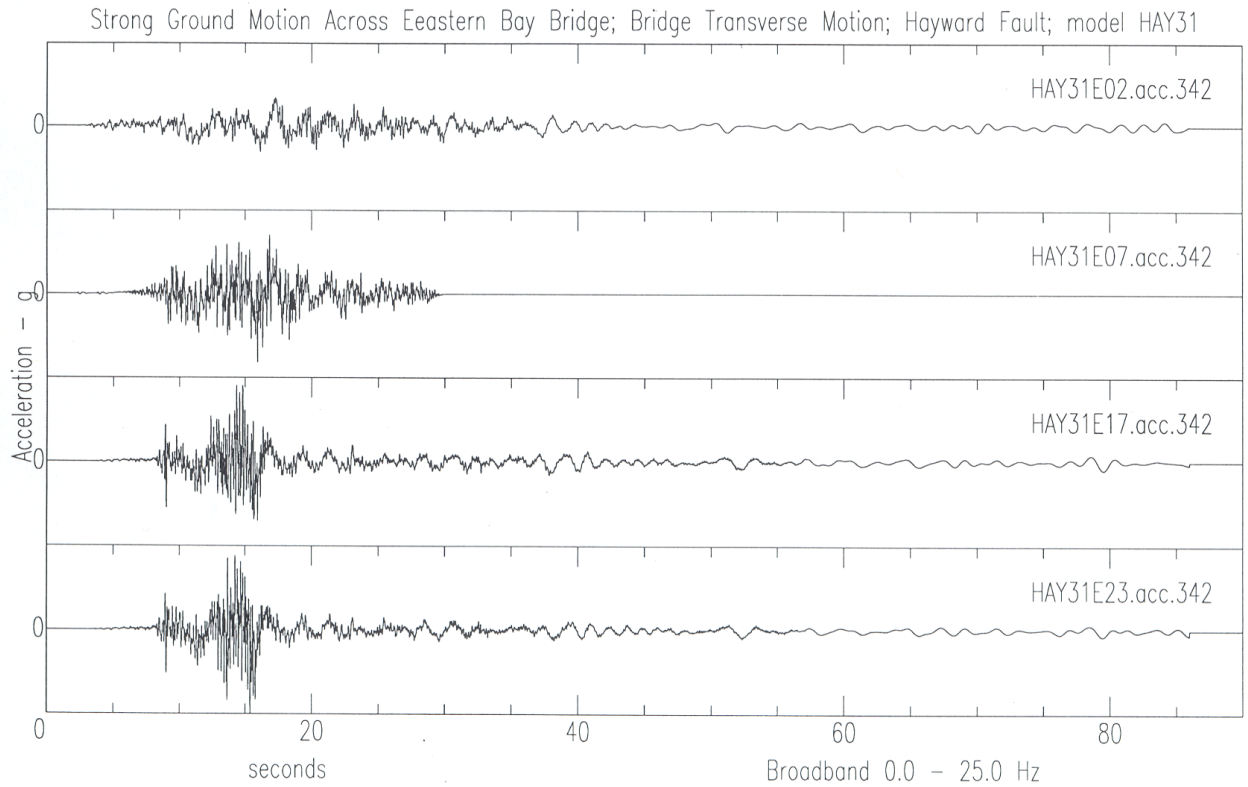

Figure 71: Bridge transverse accelerations (g), eastern span, rupture model HAY31.

Mor

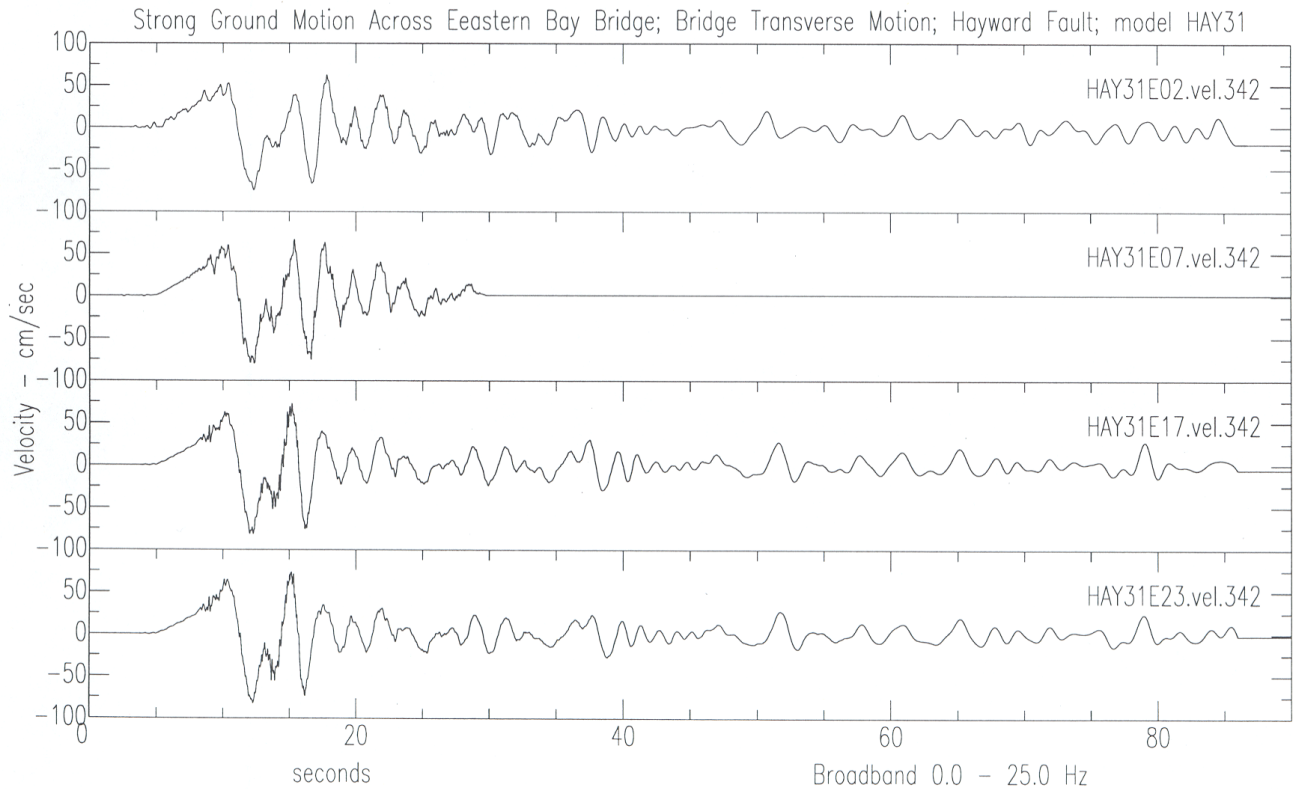

Figure 72: Bridge transverse velocities (cm/sec), eastern span, rupture model HAY31.

Mor

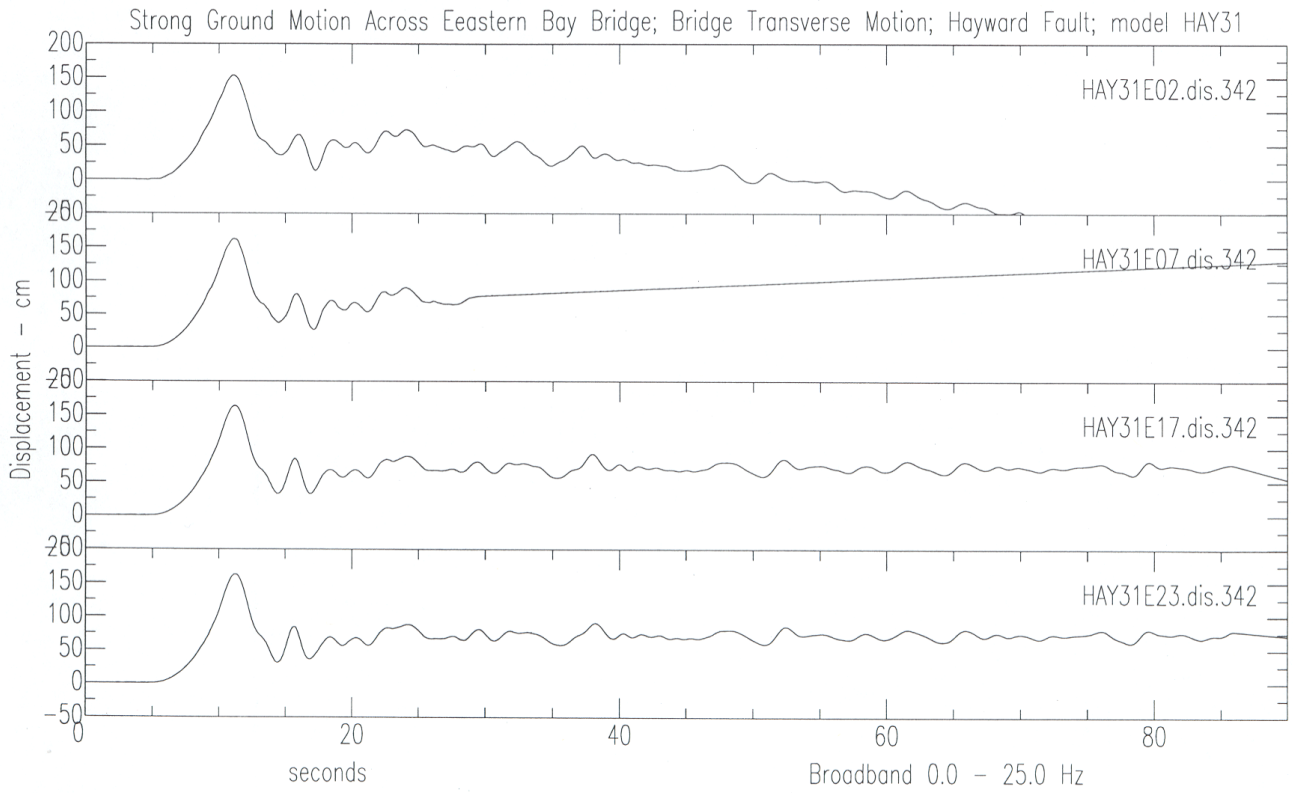

Figure 73: Bridge transverse displacements (cm), eastern span, rupture model HAY31.

Mor

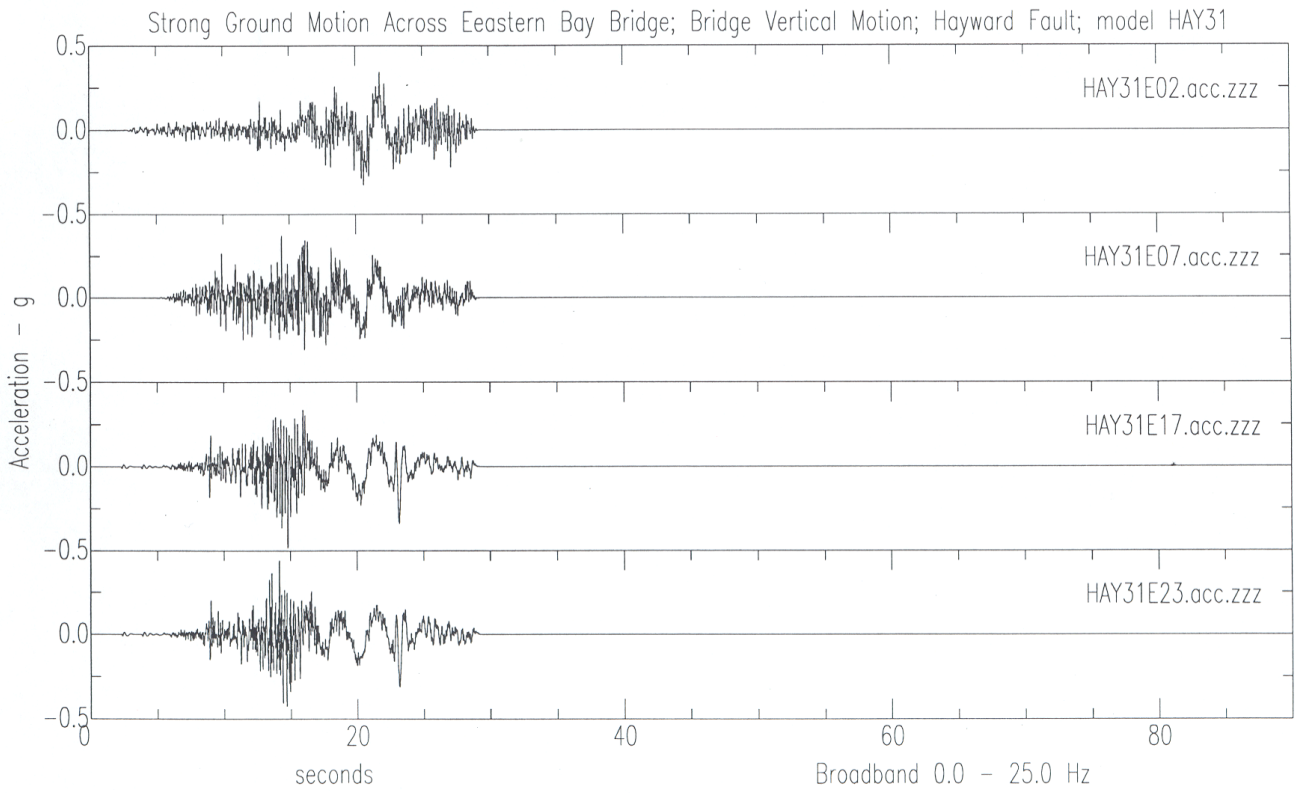

Figure 74: Bridge vertical accelerations (g), eastern span, rupture model HAY31.

Mor

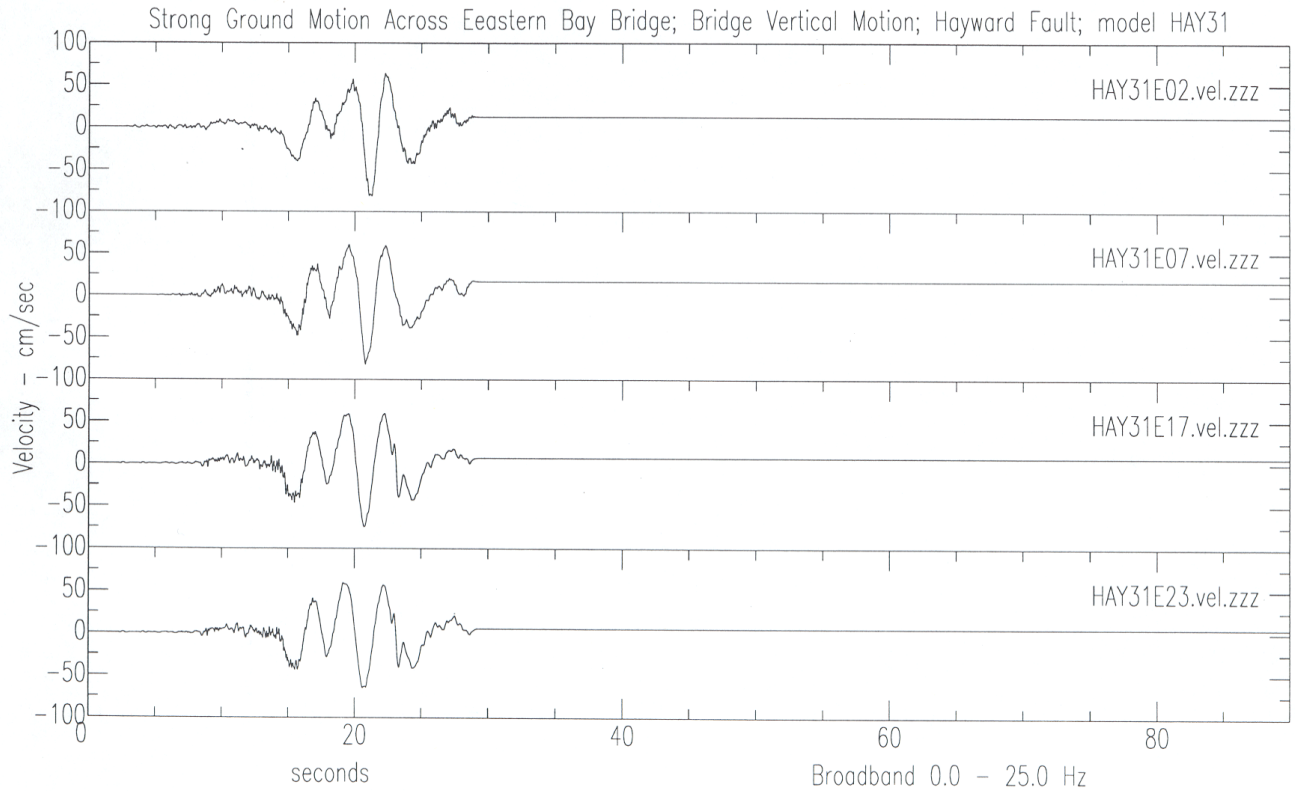

Figure 75: Bridge vertical velocities (cm/sec), eastern span, rupture model HAY31.

Mor

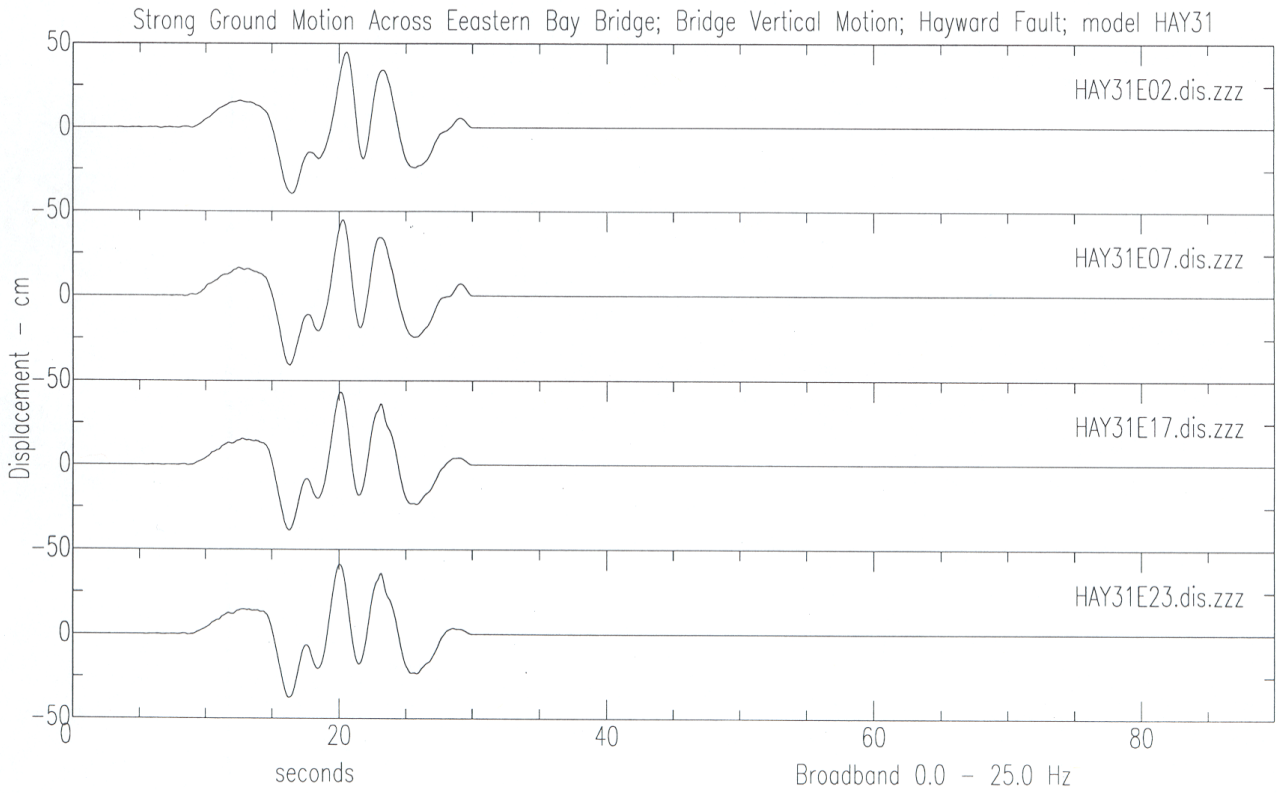

Figure 76: Bridge vertical displacements (cm), eastern span, rupture model HAY31.

Mor

HAY31 model, the western bridge moved about 45 cm north and the eastern bridge moved 75 cm north as a result of the earthquake. The bridges moved about 55 and 25 cm west, respectively.

The bridges also experienced a large transient displacement pulse. Our interpretation of ground motions is that in the near-source region, *far-field* shear-wave generation the large pulses with amplitudes up to 250 cm and *near-field* tectonic ground displacements (the ramp that results in a final offset) can result in very large long period ground displacements and velocity pulses. *Far-field* arrivals have the strongest energy in periods of about 0.2 to 0.5 s, and *near-field* arrivals have the strongest energy in periods of about 0.1 to 0.2 s. Much of these near-source ground motions would not be observed by conventional strong motion recording systems and therefore have not been included in recent standard practice structural input ground motions. These near-source pulses are arriving nearly simultaneously for and result in the very large amplitudes.

Summary and Conclusions

Downhole instrument packages placed in six boreholes along the San Francisco/Oakland Bay Bridge have recorded local seismicity since 1996. Over 200 earthquakes have been recorded. This data along with two surface sites provides the bases for ground motion analysis at eleven locations across the bridge. We have conducted wave propagation, coherency, site response, and strong ground motion studies. We found that Yerba Island provides a good rock reference site for engineering studies; as there is no apparent site response.

We apply a methodology to predict and synthesize strong ground motion along the San Francisco/Oakland Bay Bridge from a M=7.25 (Mo=8.5×10^{20} NM) earthquake along the Hayward fault, 12-15 km distant. Our methodology combines probabilistic and deterministic approaches and estimates site specific, three-component, broad-band (0.0-25.0 Hz), near-source ground motion accelerations, velocities, and displacements. We examined two different possible rupture scenarios, and "mean" and "one standard deviation" model. We combined the high frequency calculations (Hz > 0.5) based on instrument recordings with finite difference calculations for frequencies less than 0.5 Hz to generate broadband syntheses across the bridge. We found that in the near-source region, *far-field* shear-wave generation and *near-field* tectonic ground displacements can result in very large long period ground displacements and velocity pulses. *Far-field* arrivals have the strongest energy in periods of about 0.2 to 0.5 s, and *near-field* arrivals have the strongest energy in periods of about 0.1 to 0.2 s. Much of these near-source ground motions would not be observed by conventional strong motion recording systems and therefore have not been included in recent standard practice structural input ground motions. For some fault rupture scenarios, the large tectonic displacement pulse initially drives the towers with motion parallel to tectonic fault displacement before the bridge deck has "felt" the motion. Just as the far-field S-wave arrives and drives the towers in the opposite direction, the deck is beginning to respond to the tectonic displacement. So, the two main members of the bridge are being driven in opposite directions. This type of multiple long-period modal response can occur in other long period structures such as base-isolated systems and tall buildings.

We also found a high degree of variability in high frequency ground motions (periods > 0.5 sec), depending upon fault rupture scenario. The variability is higher that has been observed in the empirical data base. We hypothesize that that is because the empirical data base has too few recordings of large earthquakes in the near-source region and are not sufficient to provide a basis

for predictions. The high frequency arrivals are critical to components of large structures and to the structural response of smaller structures, in the conventional engineering sense. We conclude that the neglect of a physics-based, multi-disciplinary approach to modeling strong ground motion hazard in the past has lead to serious deficiencies in predicting the short and long period hazard to structures.

Bibliography

Aki, K. and P. G. Richards (1980). *Quantitative seismology, Theory and Methods, Volumes I and II*, W. H. Freeman and Company, San Francisco, CA.
Anderson, J.G. and S. Hough (1984) A model for the shape of the Fourier amplitude spectra of accelerograms at high frequencies. *Bull. Seis. Soc. Am.* 74, 1969-1994.

Archuleta, R., Steidl, J. H. and Bonilla, L. F. (2000). Engineering Insights from Data Recorded on Vertical Arrays. *12th World Conference in Earthquake Engineering*, Auckland, New Zealand.

Bonilla, L.F., J.H. Steidl, G.T. Lindley, A.G. Tumarkin, and R.J. Archuleta (1997) Site amplification in the San Fernando valley, CA: variability of the site effect estimation using the S-wave coda, and H/V methods. *Bull. Seis. Soc. Am.* 87, 710-730.

Brune, J.N. (1971) Tectonic stress and the spectra of seismic shear waves from earthquakes. J. Geophys. Res. **75**, 4997-5010.

Field, E.H. and K.H. Jacob (1993). The Theoretical Response of Sedimentary Layers to Ambient Seismic Noise. *Geophysical Research Letters.* **20** (24), 2925-2928.

Glaser, S.D. (1995). System Identification and Its Applications to Estimating Soil Properties, *Journal of Geotechnical Engineering*, 553-560.

Hanks, T.C. (1982) fmax. *Bull. Seis. Soc. Am.* 72, 1867-1879.

Hutchings, L. (1988). Modeling strong earthquake ground motion with an earthquake simulation program EMPSYN that utilizes empirical Green's functions, Lawrence Livermore National Laboratory, Livermore, CA, UCRL-ID-105890, p. 122.

Hutchings, L. (1991). 'Prediction' of strong ground motion for the 1989 Loma Prieta earthquake using empirical Green's functions, *Bull. Seis. Soc. Am.* 81, 88Ð121.

Hutchings, L. (1994). Kinematic Earthquake Models and Synthesized Ground Motion Using Empirical Green's Functions. *Bull. Seis. Soc. Am.* 84, pp. 1028-1050.

Hutchings, Lawrence, P.W. Kasameyer and W. Foxall (2003) LLNL, Hazard Mitigation Center Ground Motion Prediction Methodology. Lawrence Livermore National Laboratory, UCRL-ID 135697.

Hutchings, Lawrence and Rengin Gok (2004). Program NetMoment, a Simultaneous Inversion for Moment, Source Corner Frequency, and Site Specific t*. Lawrence Livermore National

Laboratory, UCRL-ID 135693.

Hutchings, L. and F. Wu (1990). Empirical Green's functions from small earthquakes: A waveform study of locally recorded aftershocks of the San Fernando earthquake, J. Geophys. Res. 95, 1187Ð1214.

Hutchings, L.J., S.P Jarpe, P.W. Kasameyer and W. Foxall (1996). Synthetic Strong Ground Motions for Engineering Design Utilizing Empirical Green's Functions. proceedings Fourth Caltrans Seismic Research Workshop, pp. 24; Eleventh World Conference of Earthquake Engineering, Acapulco, June 23-28, 1996 (CDROM Elsevvier); LLNL, UCRL-JC-123762.

Hutchings, Lawrence, Eleni Ioannidou, Steven Jarpe, and Giorgis N. Stavrakakis (1997). Strong Ground Motion synthesis for a M=7.2 Earthquake in the Gulf of Corinth, Greece using Empirical Green's Functions. UCRL-JC-129394 Lawrence Livermore National Laboratory.

Hutchings, Lawrence, Steven Jarpe, Paul Kasameyer (1998). Validation of a Ground Motion Synthesis and Prediction Methodology for the 1988,M=6.0, Saguenay Earthquake.UCRL-JC-129395 Lawrence Livermore National Laboratory.

Ioannidou, Eleni, Nicholas Voulgaris, Ioannis Kalogeras, Lawrence Hutchings, and George Stavrakakis(2001). Analysis of Site Response in the Athens Area from the 7 September 1999, Mw=5.9 Athens Earthquake and Aftershock Recordings, and Intensity Observations. Special Issue on Site Response, Bollettino Di Geofisica teorica ed applicata, December 2001.

Jarpe, S.J. and P. K. Kasameyer (1996). Validation of a Methodology for Predicting Broadband Strong Motion Time Histories using Kinematic Rupture Models and Empirical Green's Functions. *Bull. Seis. Soc. Am.* 86, pp1116-1129.

Safak, E. (1997). Models and Methods to Characterize Site Amplification from a Pair of Records. *Earthquake Spectra.* **13**(1), 97-129.
Steidl, J.H., A.G. Tumarkin, and R.J. Archuleta (1996) What is a reference site? *Bull. Seis. Soc. Am.* 86, pp. 1733-1748.

Turpin, C. (2000) *Seismic Profile of the Franciscan Formation Beneath the San Francisco-Oakland Bay Bridge, San Francisco Bay, California*, senior thesis, California State University, Sacrament, Californis.

UCB (2000). Northern California Earthquake Data Center http://quake.geo.berkeley.edu/ ncedc/ ncedc.access.html.

Scognamiligo, Laura (2004). *A test of Ground Amotion Prediction Methods that utilize Small Earthquakes.* Ph.D. dissertation, Institute of Volcanology and Geophysics, Rome, Italy.